

**Discovery and Mechanistic Studies of Novel Redox Modulators for Treatment of
Pancreatic Cancer**

by

Shuai Hu

A dissertation submitted in partial fulfillment
of the requirements for the degree of
Doctor of Philosophy
(Medicinal Chemistry)
in the University of Michigan
2020

Doctoral Committee:

Professor Nouri Neamati, Chair
Assistant Professor Amanda Lee Garner
Professor Mats Ljungman
Associate Professor Zaneta Nikolovska-Coleska
Associate Professor Maureen Sartor
Professor Duxin Sun

Shuai Hu

shuaihu@umich.edu

ORCID 0000-0001-9311-7942

© Shuai Hu 2020

DEDICATION

*To my great parents and my beloved husband,
for their forever support, trust and love*

ACKNOWLEDGEMENTS

This is an unforgettable journey that can not be finished successfully without many people's support. First of all, I want to sincerely thank my PhD advisor, Dr. Nour Neamati, for his guidance on my thesis projects and encouragement when I met obstacles. His enthusiasm in science inspires me to pursue my interest in drug discovery and development, and I appreciate his support in my dual Master's degree in bioinformatics to assist my thesis projects. His professional mentorship guides me to be both an independent researcher and an essential team player in collaborative projects. I learned science and perseverance from him and also figured out where my passion is in my future career from the past experience. I am thankful for his trust, help and advice. In addition, I am grateful for the support from all my committee members. I have a close collaboration with Dr. Mats Ljungman's lab and Dr. Duxin Sun's lab, and their strong expertise in Bru-seq and pharmacokinetics broadened my knowledge and led my projects into the right direction. Dr. Amanda Garner and Dr. Zaneta Nikolovska-Coleska were previously on my committee for the MC740 class, and they had thoughtful discussions with me on drug discovery and science in preparation for my next step in PhD. Dr. Maureen Sartor also gave me great advice in the bioinformatics classes and personal development. I am really thankful for their suggestions and support in my graduate studies.

Next, I want to thank my labmates from the Neamati Lab. It is really great to meet these people, and I am especially lucky to have Andrea Shergalis and Christine Cuthbertson as my classmates and friends. These two talented and smart girls made my life abroad more joyful. I am

grateful for their trust and support all the time. I also want to thank Dr. Yuting Kuang, a previous PhD student in the lab, who taught me experiments when I rotated in the lab and provided me a comprehensive background on reactive oxygen species, which I continued to work on as my dissertation projects. Moreover, Dr. Tiangong Lu helped me master some new experiments, and Dr. Ana Kyani taught me how to perform signaling pathway analysis. Since then I started to dive into the bioinformatics pool. I also want to thank all the co-authors in my projects to make things feasible. I would like to express my special gratitude to our collaborator Dr. Mario Sechi, who helped synthesize the QD analogs, and Dr. Yi Jin, who synthesized the QCBT7 analogs. Armand Bankhead III collaborated with me on several projects, and also kindly taught me some new bioinformatics analysis. There are also many postdocs who helped me in different projects, including Yanghan Liu, Wenmin Chen, Shuai Mao, and Yibin Xu. Additionally, Maha Hanafi is a supportive friend to discuss projects and share ideas. Sean McCann assisted me in animal studies. Brian Magnuson, Michelle Paulsen, and Karan Bedi from Ljungman lab helped me in understanding Bru-seq technique, and Bo Li and Lipeng Dai from Sun Lab provided me guidance in the pharmacokinetic studies. I really appreciate these support and assistance.

Finally, I want to greatly extend my gratitude to my family and friends outside the lab. They are definitely another important motivation for me to survive and enjoy my graduate studies. I am extremely fortunate to meet my husband here in Ann Arbor, and thanks for his unconditionally understanding, support, care and love to let me still be proud of myself and insist on my dreams. I sincerely thank my parents far away in China now, but the distance does not block their trust and love for me, and I aim to become a valuable person as my parents in their own careers. Moreover, I met many lovely friends and PKU alumni from different departments here at umich and thank them for spending time together and chatting about life, family and

career. I also want to thank my 15-classmate cohort in my PhD program, who made this group special and more fun.

Table of Contents

DEDICATION	ii
ACKNOWLEDGEMENTS	iii
LIST OF FIGURES	vii
LIST OF TABLES	x
LIST OF ABBREVIATIONS	xii
ABSTRACT	xiv
CHAPTER I. Introduction	1
CHAPTER II. ROS-Related Genes in Pancreatic Cancer	15
CHAPTER III. A Novel Redox Modulator Induces a GPX4-mediated Cell Death Dependent on Iron and Reactive Oxygen Species	40
CHAPTER IV. Identification and Characterization of Novel Mitochondrial Transcription Inhibitors	79
CHAPTER V. Mechanistic Studies of Quinolin-Chlorobenzothioate Derivatives with Proteasome Inhibitory Activity	103
CHAPTER VI. Concluding Summary and Future Directions	129
APPENDIX. Drug Synergism Prediction Using Machine Learning	137

LIST OF FIGURES

Figure I-1. General ROS production in the cell cytoplasm, mitochondria, and ER.	3
Figure I-2. The ER (pink) is an oxidizing environment, maintained by redox sensor glutathione (GSH/GSSG), with a reduction potential much larger than that of the cytoplasm.	6
Figure I-3. Structures of select redox modulators under investigation in cancer.	8
Figure II-1. Two arms of bioinformatics analysis identified ROS-signaling genes related to the progression and survival of pancreatic cancer patients.	18
Figure II-2. Select genes are significantly associated with tumor progression in both TCGA and Bailey datasets and were regulated by H ₂ O ₂ .	22
Figure II-3. Four genes are significantly related to the overall survival and progression of pancreatic cancer patients in the TCGA dataset from the Bru-seq gene list.	27
Figure II-4. Correlation analysis of <i>NFE2L3</i> , <i>PTPN14</i> , <i>ZNF547</i> and <i>KIAA1683/IQCN</i> in PDAC patients from TCGA database.	31
Figure III-1. Transcriptomic profile of QD394 is similar to that of napabucasin (napa) and H ₂ O ₂ .	43
Figure III-S1. Characterization of originally synthesized QD394 analogs.	44
Figure III-2. QD394 increases cellular ROS level and reduces GSH/GSSG ratio in MIA PaCa-2 cells.	46
Figure III-S2. QD394 did not change GSH level significantly, but napabucasin and BSO did.	47
Figure III-3. QD394 induces iron-dependent and GPX4-mediated ferroptosis in MIA PaCa-2 cells.	50
Figure III-S3. Combination studies between QD394, napabucasin, and cell death inhibitors in MIA PaCa-2 cells.	51
Figure III-S4. QD394 and QD394-Me reduced the melting temperature of GPX4 in PANC-1 cells.	52

Figure III-4. Common genes/proteins between Bru-seq and proteomics analysis reveal that QD394 interferes with mitochondrial gene expression and RNA catabolic process.	54
Figure III-5. QD394 is synergistic with select FDA-approved drugs in pancreatic cancer cells.	59
Figure III-S6. Combination of QD394 and napabucasin in PANC-1 cells.	59
Figure III-6. Pharmacokinetics optimization of QD394 leads to QD394-Me with better stability in mouse plasma, and QD394-Me has a similar cellular profile as QD394.	63
Figure III-S7. Plasma concentration of QD394 and QD394-Me administered <i>via</i> IP, PO, or IV in CD-1 mice.	63
Figure III-S8. Major metabolite of QD394-Me in mouse plasma and its abundance profiles administered <i>via</i> IV or PO in mice.	64
Figure III-S9. <i>In vivo</i> study with female Balb/c mice implanted subcutaneously with CT-26 cells.	64
Figure III-7. Summarized working mechanisms of QD394 and QD394-Me in pancreatic cancer cells.	68
Figure IV-1. The structures of SQD1, Mito-Chlor, chlorambucil and select anticancer agents with a quinone scaffold.	80
Figure IV-2. The effects of SQD1 and Mito-Chlor on mitochondrial transcription, mitochondrial proteins and ATP production.	84
Figure IV-3. SQD1 and Mito-Chlor share similar transcriptomic profiles and enriched gene sets.	86
Figure IV-4. SQD1 and Mito-Chlor inhibit cell growth and increase ROS levels in MIA PaCa-2 cells.	90
Figure IV-5. SQD1, Mito-Chlor and H ₂ O ₂ induce similar changes in protein expression in MIA PaCa-2 cells.	91
Figure IV-6. Proposed mechanisms of action of SQD1 and Mito-Chlor, and the adaptation pathways of pancreatic cancer cells in response to SQD1 and Mito-Chlor.	93
Figure V-1. Structures of select proteasome inhibitors and the lead compound QCBT7.	105
Figure V-2. QCBT7 upregulated the gene sets related to proteasome inhibition, unfolded protein response (UPR), glycolysis and hypoxic response.	111
Figure V-3. QCBT7 and MG132 have common enriched gene sets in proteasome inhibition pathway and hypoxic response.	114

Figure V-4. QCBT7 causes the accumulation of ubiquitylated proteins in MIA PaCa-2 and PANC-1 cell lines, similar to MG132 and ixazomib.	116
Figure V-5. QCBT7 increases nascent RNA and protein expression of genes related to glycolysis and ER stress in pancreatic cancer cells.	118
Figure V-6. QCBT7 increases nascent RNA and protein expression of genes related to hypoxia in pancreatic cancer cells.	120
Figure V-S1. PFKFB4 protein level decreased by PFKFB4 siRNA at 30 pmol and 60 pmol, and QCBT7 increased the protein level back.	122
Figure VI-1. Mechanistic studies of QD394 and QD394-Me in pancreatic cancer cells.	129
Figure VI-2. Characterization of mitochondrial transcription inhibitors.	130
Figure VI-3. Characterization of QCBT7 analogs.	131
Appendix-1. The workflow of TAIJI framework.	139
Appendix-2. Runtimes and prediction performance of TAIJI.	140

LIST OF TABLES

Table II-1. Summary of genes significantly associated with PDAC tumor progression in each category.	22
Table III-1. Cytotoxicity of QD compounds in MIA PaCa-2, PANC-1, and BxPC-3 cancer cell lines.	44
Table III-2. Select cell death inhibitors that were combined with QD394 in pancreatic cancer cells.	49
Table III-3. STRING analysis of 17 upregulated genes/proteins in common between Bru-seq and proteomics.	55
Table III-4. STRING analysis of 35 downregulated genes/proteins in common between Bru-seq and proteomics.	56
Table III-5. PK optimization of QD394. Microsomal stability, plasma stability, and PK studies were performed to evaluate the PK profiles of QD394 and its analog QD394-Me.	61
Table III-S1. Tissue distribution of QD394-Me in mouse.	61
Table III-S2. Cytotoxicity of QD394, QD394-Me, and napabucasin in GPX4-knockdown PANC-1 and BxPC-3 cells.	65
Table IV-1. Top 25 protein-coding genes upregulated by SQD1 in MIA PaCa-2 cells.	87
Table IV-2. Common upregulated (A) and downregulated (B) enriched gene sets among the top 20 of SQD1 and Mito-Chlor.	87
Table IV-3. Cytotoxicity of SQD1, SQD2 and Mito-Chlor in MIA PaCa-2 cells.	88
Table IV-4. Cytotoxicity of SQD1 in a panel of cancer cell lines.	89
Table V-1. Cytotoxicity of 8-thioester/ester/amide-quinoline derivatives of QCBT7 in a panel of cancer cell lines.	106
Table V-2. Stability of (a) QCBT7 and (b) 8TQ in DMSO and 1:1 DMSO/water solution with or without NAC.	109

Table V-3. Top 50 upregulated genes in QCBT7-treated MIA PaCa-2 cells.

111

LIST OF ABBREVIATIONS

ROS - reactive oxygen species

MOA - mechanism of action

Bru-seq - bromouridine-labeled RNA sequencing

GSEA - Gene Set Enrichment Analysis

STRING - Search Tool for the Retrieval of Interacting Genes/Proteins

DAVID - Database for Annotation, Visualization and Integrated Discovery

CMAP - Connectivity Map

TCGA - The Cancer Genome Atlas

PK - pharmacokinetics

FC - fold change

OXPHOS - oxidative phosphorylation

RFU - relative fluorescence unit

RLU - relative luminescence unit

RT-PCR - real-time polymerase chain reaction

CETSA - cellular thermal shift assay

TPP - triphenylphosphonium

ER - endoplasmic reticulum

GO - gene ontology

MAM - mitochondria-associated membrane

PDAC - pancreatic ductal adenocarcinoma

mtDNA - mitochondrial DNA

8TQ - 8-quinolinethiol hydrochloride

NAC - N-acetylcysteine

Nec-1 - necrostatin-1

H-strand - heavy strand

L-strand - light strand
LSP - light-strand promoter
HSP1 - heavy-strand promoter 1
HSP2 - heavy-strand promoter 2
D-loop - displacement loop
FCCP - carbonyl cyanide-4-(trifluoromethoxy)phenylhydrazone
CCCP - carbonyl cyanide 3-chlorophenylhydrazone
Vit-E - vitamin E
DHE - dihydroethidium
TBHP - tert-butyl hydroperoxide
LCMS - liquid chromatography mass spectrometry
MSigDB - molecular signatures database
UPR - unfolded protein response
NES - normalized enrichment score
FDR - false discovery rate

ABSTRACT

Pancreatic cancer remains a devastating disease and conventional chemotherapy shows modest efficacy because of drug resistance and systemic toxicity. The reprogramming of energy metabolism and oxidative stress are two hallmarks of cancer, and redox modulators have been developed as an attractive approach to treat cancer. At low or moderate levels, reactive oxygen species (ROS) serve as signaling molecules to mediate cellular functions; while at high levels, ROS induce oxidation of lipids, proteins, and DNA, ultimately leading to cell death. In this dissertation project, I aimed to identify novel redox modulators and provide a preclinical characterization of their mechanisms of action (MOAs) in pancreatic cancer cells.

Through lead optimization of a previously studied quinazolidinedione-based redox modulator, we identified QD394 with significant cytotoxicity in pancreatic cancer cells. Bru-seq technique and clustering analysis revealed remarkably similar post-treatment transcriptomic profiles between QD394 and napabucasin. Both compounds inhibited STAT3 phosphorylation, induced DNA damage, increased cellular ROS, and decreased the GSH/GSSG ratio. Moreover, QD394 caused an iron- and ROS-dependent, GPX4-mediated cell death, suggesting ferroptosis as a major mechanism. QD394 also decreased the expression of mitochondrial proteins, including LRPPRC and PNPT1 involved in mitochondrial RNA catabolic processes. A derivative QD394-Me was synthesized with improved plasma stability and reduced toxicity in mice compared to QD394. These results demonstrate that QD394 and QD394-Me represent

novel ROS-inducing drug-like compounds warranting further development for the treatment of pancreatic cancer.

Mito-Chlor, a mitochondrial-targeting triphenylphosphonium derivative of the nitrogen mustard chlorambucil, was identified to inhibit transcription of the mitochondrial genome through Bru-seq analysis, which is similar to a new ROS inducer SQD1 featuring a styrylquinoline-5, 8-dione core. Both Mito-Chlor and SQD1 decreased the mRNA levels of mitochondrial genes. However, only Mito-Chlor reduced their protein expression, and interfered with mitochondria membrane potential and oxidative phosphorylation. Both compounds increased cellular and mitochondrial ROS and stimulated similar downstream signaling related to oxidative stress and AP-1 transcription factors. These results establish SQD1 and Mito-Chlor as novel mitochondrial transcription inhibitors and redox modulators that may be applied to study cancer cell death related to mitochondrial function and redox signaling.

Finally, a medium-throughput phenotypic screen of 20,000 diverse drug-like compounds produced a quinolin-chlorobenzothioate, QCBT7, as a potent hit with submicromolar cytotoxicity in cancer cells. Its structure is similar to 8-quinolinethiol hydrochloride (8TQ), a proteasome inhibitor. Proteasome inhibitors have shown anticancer efficacy. As a more stable derivative of 8TQ, QCBT7 caused the accumulation of ubiquitylated proteins, indicating its proteasome inhibitory activity. Additionally, QCBT7 increased the expression of a set of genes (PFKFB4, CHOP, HMOX1, and SLC7A11) at both nascent RNA and protein levels, similar to the known proteasome inhibitors MG132 and ixazomib. We have also identified PFKFB4 as a potential biomarker of proteasome inhibitors that can be used to monitor treatment response. Together, this study discovers that QCBT7 induces proteasome inhibition, hypoxic response, endoplasmic reticulum stress, and glycolysis, leading to cell death.

In summary, the work as a whole provides a detailed characterization of redox modulators and their effects on cell death, mitochondria, or proteasome activity. We also identify novel ROS-related genes and pathways that could be beneficial for pancreatic cancer therapeutics. This thesis contributes to the overall understanding of ROS signaling in pancreatic cancer and the validity of ROS-modulating therapies. This collective work provides the foundation to improve the redox modulators discovered for testing *in vivo*.

CHAPTER I

Introduction

Reactive oxygen species (ROS) are partially reduced metabolites of oxygen with strong oxidizing capabilities that contribute to diseases related to cell metabolism, survival, and death. There are two main classes of ROS: free radicals and non-radicals. Free radicals include hydroxyl radical (HO^{\bullet}), nitric oxide (NO^{\bullet}), peroxynitrite (ONOO^{-}), superoxide anion ($\text{O}_2^{\bullet-}$), nitrogen dioxide (NO_2^{\bullet}), peroxy radicals (ROO^{\bullet}), and lipid peroxy (LOO^{\bullet}). Non-radicals include hydrogen peroxide (H_2O_2), singlet oxygen ($^1\text{O}_2$), and lipid peroxide (LOOH). The most well-studied ROS are hydrogen peroxide (H_2O_2), superoxide anion ($\text{O}_2^{\bullet-}$), and hydroxyl radical (HO^{\bullet})¹. At low doses, ROS maintain cellular homeostasis as secondary signaling molecules, and, at high concentrations, ROS can induce severe oxidative damage in proteins, lipids, and DNA, earning their reputation as a double-edged sword²⁻⁴.

ROS signaling in mitochondria and endoplasmic reticulum

ROS are generated *via* both non-enzymatic and enzymatic reactions. ROS generated as byproducts of oxidative phosphorylation and ATP production during electron transfer reactions in the mitochondria are the major source (Figure I-1). ATP generation depends on the mitochondrial respiratory chain in the inner mitochondrial membrane, which consists of five major protein complexes (complex I, II, III, IV, and V)⁵. ATP is synthesized by $\text{F}_0\text{F}_1\text{-ATPase}$ *via* the proton gradient across the membrane, and during this electron transfer, molecular oxygen accepts leaked electrons to form ROS⁶. Complex I (NADH dehydrogenase subunits) and

complex III (ubiquinol-cytochrome C reductase complex subunits) are the major sites of electron leak in the mitochondrial respiratory chain ^{7,8}. Furthermore, complex II (succinate dehydrogenase) also plays a role in ROS generation, and mutation or dysfunction of complex II can enhance ROS production ⁹. In addition to the mitochondria, ROS are also produced by nicotinamide adenine dinucleotide phosphate (NADPH) oxidases and xanthine oxidase in the cytoplasm, and generated in the endoplasmic reticulum (ER), peroxisome, and other organelles ². Although mitochondria hold the reputation as the primary ROS-inducing organelles of the cell, oxidative protein folding in the ER generates large quantities of ROS, and in fact, the ER lumen contains more ROS than mitochondria ^{10,11}. The ER and mitochondria interact *via* a physical contact known as the mitochondria-associated ER membrane (MAM), and the MAM allows exchange of Ca²⁺, ROS, lipids, and nutrients between the ER and the mitochondria, thus promoting cellular bioenergetics and metabolism. MAM signaling is important in biological processes including lipid biosynthesis, cell death, and macroautophagy ¹².

In eukaryotes, the ER is responsible for secreted and membrane-bound protein folding and calcium storage. ROS are generated during oxidative protein folding when molecular chaperones, such as protein disulfide isomerases (PDIs), form disulfide bonds in nascent polypeptides. Active site cysteine residues in PDIs accept electrons from free thiols in nascent polypeptides to generate a disulfide bond. PDIs then transfer the electrons to membrane-bound endoplasmic reticulum oxidoreductase 1 (ERO1) to perform another cycle of catalysis ². ERO1 further transfers the electrons to O₂ and generates H₂O₂. H₂O₂ produced by ERO1 in the ER lumen is involved in signaling and oxidative protein folding *via* peroxiredoxin 4 ^{13,14}. In response to ROS generation, antioxidant enzymes, such as superoxide dismutase, catalase, and glutathione peroxidase, maintain redox homeostasis by converting ROS into water and oxygen.

Other antioxidant molecules, including reduced glutathione (GSH), vitamin E, and NADH, can also inactivate ROS (Figure I-1) ^{15,16}. In the ER, ROS can also be produced by NADPH oxidases downstream of PDIA1 activity ¹⁷.

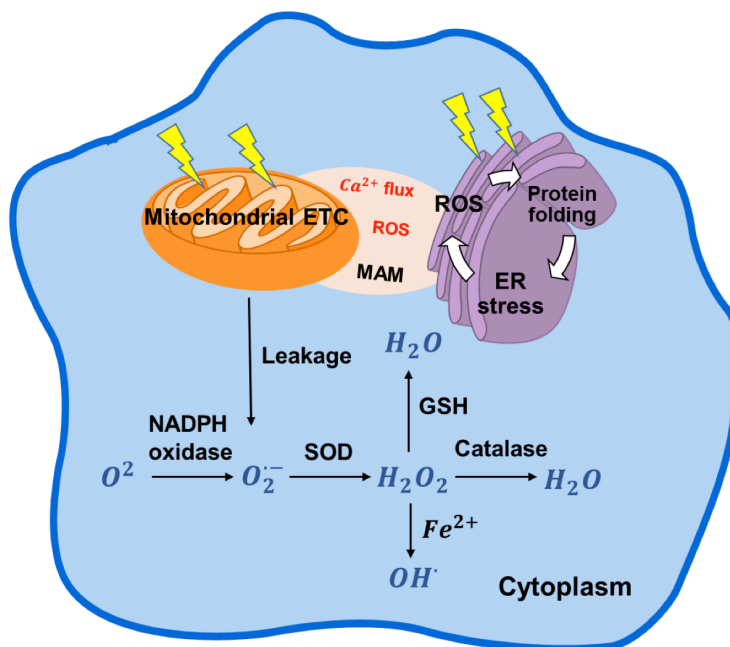


Figure I-1. General ROS production in the cell cytoplasm, mitochondria, and ER. The various types of ROS interconvert, based on cell requirements and extracellular stimuli. Mitochondria and ER are the two major organelles that control ROS signaling. ETC, electron transport chain; ROS, reactive oxygen species; MAM, mitochondria-associated ER membrane; ER, endoplasmic reticulum; SOD, superoxide dismutase; NADPH, nicotinamide adenine dinucleotide phosphate, reduced.

The MAM was first identified in 1986 as a major site of phospholipid synthesis and transportation and is now known to be essential for calcium homeostasis, energy metabolism and other signaling pathways ¹⁸⁻²⁰. High concentrations of ER Ca^{2+} are released at MAM sites and taken up into the mitochondria by the Ca^{2+} uniporter on the inner mitochondrial membrane ²¹. ROS generated by either the ER or mitochondria in H_2O_2 nanodomains generated by cristae can localize at the MAM interface and perturb calcium signaling ²² (Figure I-1). Importantly, ERO1, a key regulator of oxidative stress in the ER, is enriched at the MAM interface and regulates calcium flux ^{23,24}. ERO1 localization at the MAM interface demonstrates the role of redox

signaling on calcium flux through the mitochondria. ERO1 does not cross the MAM but may exert its effect *via* diffusible H₂O₂. Dysfunction of the ER-mitochondrial crosstalk at the MAM has been implicated in neurological diseases such as Alzheimer's and Parkinson's, thus ERO1's function at this interface may emerge as a critical driver of MAM dysfunction²⁵. The oxidizing environment of the ER is maintained by the GSH/GSSG ratio to facilitate protein folding (Figure I-2)^{2,26}. Correctly folded and processed proteins are transported out of the ER, while misfolded proteins can be either refolded or degraded *via* the ER-Associated Degradation (ERAD) pathway^{2,27}. Therefore, the ER is equipped with a regulatory mechanism to accurately differentiate between unfolded/native, misfolded, and correctly folded proteins. The rate of the reaction between PDI and GSSG or GSH is rapid, likely contributing to its role as an ER redox sensor²⁸. In a disease state, misfolded and unfolded proteins can accumulate to trigger ER swelling and the ER stress response²⁹. During ER stress, the GSH/GSSG ratio is disturbed, further increasing ROS production and distorting the ER redox environment³⁰. In eukaryotes, the ER is more susceptible to oxidative stress due to limited antioxidant enzymes, which indicates its important role in the induction of redox imbalance and cellular stress³¹. ER stress stimulates the unfolded protein response (UPR), which can promote cell survival, or upon prolonged ER stress, apoptosis ensues³². Furthermore, ER stress can induce calcium release from the ER into the cytosol. Mitochondria uptake the released Ca²⁺, causing physical and metabolic changes. For example, ROS induces the release of cytochrome c to the cytoplasm, inhibiting complex III activity and further inducing ROS in the form of a ubisemiquinone radical intermediate². Increased Ca²⁺ ions also stimulate mitochondrial Krebs cycle dehydrogenases and nitric oxide synthase, both leading to the elevation of ROS. Most importantly, in a vicious cycle, the ER-induced mitochondrial ROS may accelerate the release of Ca²⁺ from the ER to further increase

mitochondrial oxidative stress². Mitochondrial dysfunction alters ATP generation, which is required for protein folding and bond formation in the ER. Thus, mitochondrial dysfunction further aggravates ER stress².

A major role of the ER involves calcium storage, and research in recent years furthered our understanding of the role in calcium signaling. In addition to being highly oxidizing compared to other cellular compartments, the ER differs in that calcium concentrations are higher such that free calcium concentration is 100–800 μM ^{33,34}. ROS ($\text{O}_2^{\cdot-}$, H_2O_2 , and HO^{\cdot}) also communicate bidirectionally with calcium in a complex relationship. Calcium signaling is necessary for ROS production, and ROS can regulate calcium signaling³⁵. In mitochondria, calcium promotes metabolism *via* both the tricarboxylic acid cycle³⁶ and oxidative phosphorylation. In turn, ROS regulates calcium signaling by modulating plasma membrane and intracellular calcium channels and Ca^{2+} ATPases³⁵.

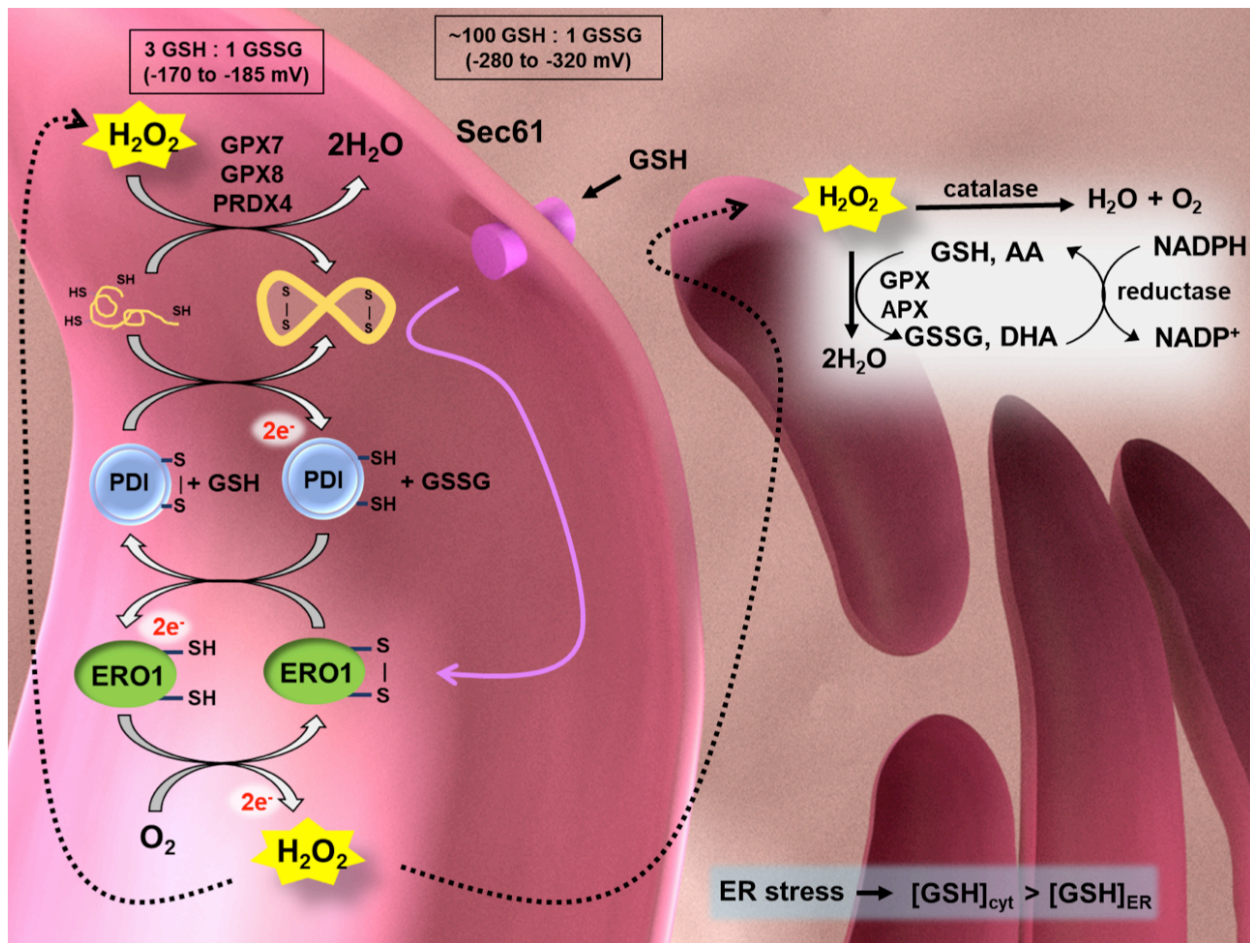
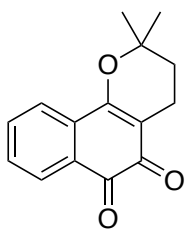


Figure I-2. The ER (pink) is an oxidizing environment, maintained by redox sensor glutathione (GSH/GSSG), with a reduction potential much larger than that of the cytoplasm (ER ϵ : -170 to -185 mV; cytoplasm ϵ : -280 to -320 mV). The oxidizing environment promotes nascent protein folding and disulfide bond formation. Ero1 is a key mediator of disulfide bond formation in the ER. Disturbed protein folding may cause ER stress and increased ER ROS production, further affecting mitochondrial and cellular metabolism. Reduced polypeptides are oxidized by PDI, which transfers its electrons to Ero1. Ero1 is reoxidized by oxygen and produces H_2O_2 . H_2O_2 is reduced through various mechanisms in the ER including catalase, glutathione peroxidases (GPX7 and GPX8), peroxiredoxin 4 (PRX4), and ascorbate peroxidase (APX). Background image created in Blender 2.79.

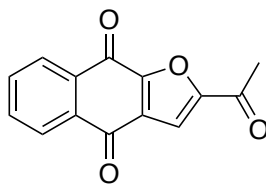
ROS-related cancer therapies

In both tumor and normal cells, low levels of ROS serve as second messengers for downstream signaling pathways and promote cell survival and cell proliferation, while increased levels of ROS cause oxidative damage to DNA, proteins, and lipids, leading to cellular malfunction and cell death³⁷. Additionally, cancer cells have higher redox requirements than

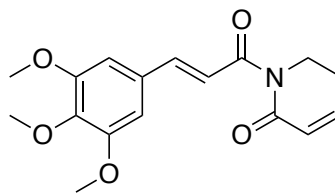
normal cells due to their increased cell metabolism, dysfunctional mitochondria, scarce nutrients, and oxygen-poor microenvironment ³⁸. Higher intracellular ROS levels force cancer cells to develop robust antioxidant systems to adapt to oxidative stress. Cancer cells are more vulnerable to redox modulators than normal cells due to their strong dependence on intrinsically high levels of ROS and limited antioxidant threshold. Reprogramming energy metabolism and oxidative stress are also two hallmarks of cancer ³⁹⁻⁴². Therefore, treating cancer with small molecule redox modulators may overwhelm cancer cells selectively. Several redox modulators are under review in clinical trials to evaluate efficacy and safety profiles in cancer ¹⁰⁻¹⁴. ARQ761, a beta-lapachone prodrug that reacts with NAD(P)H quinone dehydrogenase 1 (NQO1) to generate ROS, showed modest efficacy in an open-label, dose-escalation Phase I study ⁴³. ARQ761 is currently in a Phase II clinical trial with gemcitabine/nab-paclitaxel in patients with advanced pancreatic cancer who have not been treated with gemcitabine ⁴⁴. Napabucasin is an orally-administered cancer stemness inhibitor with a quinone scaffold and has been tested in Phase III clinical trials in multiple cancers ⁴⁵⁻⁴⁷. Napabucasin inhibits Signal Transducer and Activator of Transcription 3 (STAT3) signaling and increases ROS levels predominately by NQO1 bioactivation. There are also other ROS-modulating agents under investigation in cancer treatment (Figure I-3) ⁴⁸⁻⁵¹. Therefore, regulating cellular ROS is a promising method to treat cancer. In the following chapters, I hypothesize that redox modulators are effective in treating pancreatic cancer, and I aim to understand the working mechanisms of the newly discovered ROS modulators.



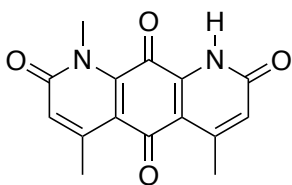
β -lapachone



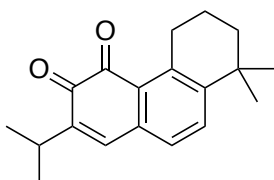
Napabucasin



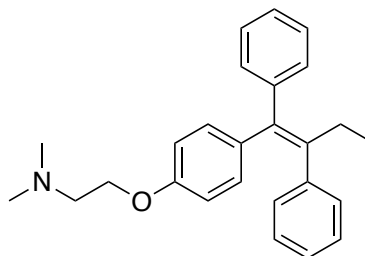
Piperlongumine



Deoxyxyboquinone



Miltirone



Tamoxifen

Figure I-3. Structures of select redox modulators under investigation in cancer.

Pancreatic cancer is the fourth leading cause of cancer death in the United States, and its incidence and mortality rates are continuing to increase worldwide ^{52,53}. It is predicted to be the second leading cause of cancer death in the USA by 2030 ^{53,54}. Pancreatic cancer is primarily diagnosed at a late stage because early-stage symptoms are non-specific. The 5-year survival rate at the advanced stage is only around 3% ⁵². Conventional chemotherapies show only modest efficacy in pancreatic cancer because of drug resistance and systemic toxicity, including the current standard-of-care, FOLFIRINOX (folinic acid, 5-fluorouracil (5-FU), irinotecan, and oxaliplatin), and gemcitabine together with nab-paclitaxel ^{53,55}. Therefore, it is imperative to find new improved therapies to treat pancreatic cancer, and I aim to use redox modulators to treat this disease.

Next-generation sequencing to assist mechanistic studies

ROS-modulating compounds display cancer-specific cytotoxicity and anti-tumor efficacy; however, the involved signaling pathways, working mechanisms, and affected targets of ROS are complex. It remains considerably challenging to identify the specific targets and illustrate the mechanisms of action (MOAs) of each anti-cancer therapeutic agent, even for the FDA-approved drugs. The advancement of next-generation sequencing and bioinformatics techniques opens a new avenue for investigating the drug targets and MOAs. These methods provide insights into the changes of transcriptomic profiles and downstream signaling, and facilitate studies of cancer genomics, diagnosis, and treatment^{56,57}. In my studies, I used the bromouridine-labeled RNA sequencing (Bru-seq) technique to determine the induced and repressed genes in response to our redox modulators, and ultimately identify the affected signaling pathways and potential targets. Bru-seq was developed by Dr. Mats Ljungman's lab to assess the newly synthesized RNA in cells⁵⁸. Bromouridine was added to cells at the last 30 min of drug treatments to label the newly synthesized RNAs. The bromouridine-containing RNAs were captured using anti-BrdU antibodies conjugated to magnetic beads and converted to cDNA libraries (Illumina TrueSeq) that were sent for deep sequencing at the University of Michigan Sequencing Core. This technique could provide information on the direct changes of transcriptome caused by the compounds instead of the steady states of mature RNAs.

With the Bru-seq data, I further used bioinformatics tools, such as Gene Set Enrichment Analysis (GSEA) and Search Tool for the Retrieval of Interacting Genes/proteins (STRING) to determine the enriched gene sets after compound treatments. Publicly available databases, including The Cancer Genome Atlas (TCGA), Connectivity Map (CMAP), and Human Protein Atlas (HPA) assist the discovery of new genes as potential pharmacodynamics biomarkers

involved in the therapeutic pathways. These analyses help generate hypotheses of MOAs or targets of redox modulators, which could be further tested using corresponding assays, such as immunoblot, siRNA knockdown, and Cellular Thermal Shift Assay (CETSA).

References

1. Li, Y. R., Robert Li, Y. & Trush, M. Defining ROS in Biology and Medicine. *Reactive Oxygen Species* vol. 1 (2016).
2. Cao, S. S. & Kaufman, R. J. Endoplasmic reticulum stress and oxidative stress in cell fate decision and human disease. *Antioxid. Redox Signal.* 21, 396–413 (2014).
3. Puspita, L., Chung, S. Y. & Shim, J.-W. Oxidative stress and cellular pathologies in Parkinson's disease. *Molecular Brain* vol. 10 (2017).
4. Sifuentes-Franco, S., Pacheco-Moisés, F. P., Rodríguez-Carrizalez, A. D. & Miranda-Díaz, A. G. The Role of Oxidative Stress, Mitochondrial Function, and Autophagy in Diabetic Polyneuropathy. *J Diabetes Res* 2017, 1673081 (2017).
5. Bolisetty, S. & Jaimes, E. A. Mitochondria and reactive oxygen species: physiology and pathophysiology. *Int. J. Mol. Sci.* 14, 6306–6344 (2013).
6. Dromparis, P. & Michelakis, E. D. Mitochondria in vascular health and disease. *Annu. Rev. Physiol.* 75, 95–126 (2013).
7. Borek, A., Sarewicz, M. & Osyczka, A. Movement of the Iron–Sulfur Head Domain of Cytochromebc1 Transiently Opens the Catalytic QoSite for Reaction with Oxygen†. *Biochemistry* vol. 47 12365–12370 (2008).
8. Warnau, J. *et al.* Redox-coupled quinone dynamics in the respiratory complex I. *Proc. Natl. Acad. Sci. U. S. A.* 115, E8413–E8420 (2018).
9. Kausar, S., Wang, F. & Cui, H. The Role of Mitochondria in Reactive Oxygen Species Generation and Its Implications for Neurodegenerative Diseases. *Cells* vol. 7 274 (2018).
10. Bulleid, N. J. & Ellgaard, L. Multiple ways to make disulfides. *Trends in Biochemical Sciences* vol. 36 485–492 (2011).
11. Malinouski, M., Zhou, Y., Belousov, V. V., Hatfield, D. L. & Gladyshev, V. N. Hydrogen peroxide probes directed to different cellular compartments. *PLoS One* 6, e14564 (2011).
12. Phillips, M. J. & Voeltz, G. K. Structure and function of ER membrane contact sites with other organelles. *Nat. Rev. Mol. Cell Biol.* 17, 69–82 (2016).

13. Tavender, T. J. & Bulleid, N. J. Peroxiredoxin IV protects cells from oxidative stress by removing H₂O₂ produced during disulphide formation. *Journal of Cell Science* vol. 123 2672–2679 (2010).
14. Zito, E. *et al.* Oxidative Protein Folding by an Endoplasmic Reticulum-Localized Peroxiredoxin. *Molecular Cell* vol. 40 787–797 (2010).
15. Gomes, E. C., Silva, A. N. & de Oliveira, M. R. Oxidants, antioxidants, and the beneficial roles of exercise-induced production of reactive species. *Oxid. Med. Cell. Longev.* 2012, 756132 (2012).
16. Tse, G., Yan, B. P., Chan, Y. W. F., Tian, X. Y. & Huang, Y. Reactive Oxygen Species, Endoplasmic Reticulum Stress and Mitochondrial Dysfunction: The Link with Cardiac Arrhythmogenesis. *Frontiers in Physiology* vol. 7 (2016).
17. Laurindo, F. R. M., Araujo, T. L. S. & Abrahão, T. B. Nox NADPH Oxidases and the Endoplasmic Reticulum. *Antioxidants & Redox Signaling* vol. 20 2755–2775 (2014).
18. Rieusset, J. The role of endoplasmic reticulum-mitochondria contact sites in the control of glucose homeostasis: an update. *Cell Death Dis.* 9, 388 (2018).
19. Thoudam, T., Jeon, J.-H., Ha, C.-M. & Lee, I.-K. Role of Mitochondria-Associated Endoplasmic Reticulum Membrane in Inflammation-Mediated Metabolic Diseases. *Mediators Inflamm.* 2016, 1851420 (2016).
20. Csordás, G., Weaver, D. & Hajnóczky, G. Endoplasmic Reticulum-Mitochondrial Contactology: Structure and Signaling Functions. *Trends Cell Biol.* 28, 523–540 (2018).
21. Csordás, G., Várnai, P., Golenár, T., Sheu, S.-S. & Hajnóczky, G. Calcium transport across the inner mitochondrial membrane: Molecular mechanisms and pharmacology. *Molecular and Cellular Endocrinology* vol. 353 109–113 (2012).
22. Booth, D. M., Enyedi, B., Geiszt, M., Várnai, P. & Hajnóczky, G. Redox Nanodomains Are Induced by and Control Calcium Signaling at the ER-Mitochondrial Interface. *Mol. Cell* 63, 240–248 (2016).
23. Anelli, T. *et al.* Ero1 α Regulates Ca²⁺ Fluxes at the Endoplasmic Reticulum–Mitochondria Interface (MAM). *Antioxidants & Redox Signaling* vol. 16 1077–1087 (2012).
24. Gilady, S. Y. *et al.* Ero1 α requires oxidizing and normoxic conditions to localize to the mitochondria-associated membrane (MAM). *Cell Stress and Chaperones* vol. 15 619–629 (2010).
25. Hetz, C. & Mollereau, B. Disturbance of endoplasmic reticulum proteostasis in neurodegenerative diseases. *Nature Reviews Neuroscience* vol. 15 233–249 (2014).
26. Chakravarthi, S., Jessop, C. E. & Bulleid, N. J. The role of glutathione in disulphide bond

- formation and endoplasmic-reticulum-generated oxidative stress. *EMBO reports* vol. 7 271–275 (2006).
27. Hwang, J. & Qi, L. Quality Control in the Endoplasmic Reticulum: Crosstalk between ERAD and UPR pathways. *Trends Biochem. Sci.* 43, 593–605 (2018).
 28. Lappi, A.-K. & Ruddock, L. W. Reexamination of the Role of Interplay between Glutathione and Protein Disulfide Isomerase. *Journal of Molecular Biology* vol. 409 238–249 (2011).
 29. Oakes, S. A. & Papa, F. R. The Role of Endoplasmic Reticulum Stress in Human Pathology. *Annual Review of Pathology: Mechanisms of Disease* vol. 10 173–194 (2015).
 30. Tu, B. P. & Weissman, J. S. Oxidative protein folding in eukaryotes. *Journal of Cell Biology* vol. 164 341–346 (2004).
 31. Santos, C. X. C. *et al.* Protein disulfide isomerase (PDI) associates with NADPH oxidase and is required for phagocytosis of *Leishmania chagasi* promastigotes by macrophages. *Journal of Leukocyte Biology* vol. 86 989–998 (2009).
 32. Zeeshan, H. M. A., Lee, G. H., Kim, H.-R. & Chae, H.-J. Endoplasmic Reticulum Stress and Associated ROS. *Int. J. Mol. Sci.* 17, 327 (2016).
 33. Bhandary, B., Marahatta, A., Kim, H.-R. & Chae, H.-J. An Involvement of Oxidative Stress in Endoplasmic Reticulum Stress and Its Associated Diseases. *International Journal of Molecular Sciences* vol. 14 434–456 (2012).
 34. Carreras-Sureda, A., Pihán, P. & Hetz, C. Calcium signaling at the endoplasmic reticulum: fine-tuning stress responses. *Cell Calcium* 70, 24–31 (2018).
 35. Görlach, A., Bertram, K., Hudecova, S. & Krizanova, O. Calcium and ROS: A mutual interplay. *Redox Biology* vol. 6 260–271 (2015).
 36. McCormack, J. G. & Denton, R. M. Mitochondrial Ca²⁺ Transport and the Role of Intramitochondrial Ca²⁺ in the Regulation of Energy Metabolism. *Developmental Neuroscience* vol. 15 165–173 (1993).
 37. Kumari, S., Badana, A. K., G, M. M., G, S. & Malla, R. Reactive Oxygen Species: A Key Constituent in Cancer Survival. *Biomark. Insights* 13, 1177271918755391 (2018).
 38. DeBerardinis, R. J. & Chandel, N. S. Fundamentals of cancer metabolism. *Science Advances* vol. 2 e1600200 (2016).
 39. Hanahan, D. & Weinberg, R. A. Hallmarks of Cancer: The Next Generation. *Cell* vol. 144 646–674 (2011).
 40. Fouad, Y. A. & Aanei, C. Revisiting the hallmarks of cancer. *Am. J. Cancer Res.* 7, 1016–

1036 (2017).

41. Hornsveld, M. & Dansen, T. B. The Hallmarks of Cancer from a Redox Perspective. *Antioxid. Redox Signal.* 25, 300–325 (2016).
42. Pavlova, N. N. & Thompson, C. B. The Emerging Hallmarks of Cancer Metabolism. *Cell Metabolism* vol. 23 27–47 (2016).
43. Gerber, D. E. *et al.* Phase 1 study of ARQ 761, a β -lapachone analogue that promotes NQO1-mediated programmed cancer cell necrosis. *Br. J. Cancer* 119, 928–936 (2018).
44. ARQ-761 Treatment With Gemcitabine/Nab-Paclitaxel Chemotherapy In Pancreatic Cancer - Full Text View - ClinicalTrials.gov. <https://clinicaltrials.gov/ct2/show/NCT02514031>.
45. Sonbol, M. B. *et al.* CanStem111P trial: a Phase III study of napabucasin plus nab-paclitaxel with gemcitabine. *Future Oncology* vol. 15 1295–1302 (2019).
46. A Study of Napabucasin (BBI-608) in Combination With FOLFIRI in Adult Patients With Previously Treated Metastatic Colorectal Cancer - Full Text View - ClinicalTrials.gov. <https://clinicaltrials.gov/ct2/show/NCT02753127>.
47. A Study of BBI608 Plus Weekly Paclitaxel to Treat Gastric and Gastro-Esophageal Junction Cancer - Full Text View - ClinicalTrials.gov. <https://clinicaltrials.gov/ct2/show/NCT02178956>.
48. Karki, K., Hedrick, E., Kasiappan, R., Jin, U.-H. & Safe, S. Piperlongumine Induces Reactive Oxygen Species (ROS)-Dependent Downregulation of Specificity Protein Transcription Factors. *Cancer Prev. Res.* 10, 467–477 (2017).
49. Lee, H. Y. *et al.* Reactive Oxygen Species Synergize To Potently and Selectively Induce Cancer Cell Death. *ACS Chem. Biol.* 12, 1416–1424 (2017).
50. Wang, L. *et al.* Miltirone induced mitochondrial dysfunction and ROS-dependent apoptosis in colon cancer cells. *Life Sci.* 151, 224–234 (2016).
51. Liu, L. *et al.* Tamoxifen reduces fat mass by boosting reactive oxygen species. *Cell Death Dis.* 6, e1586 (2015).
52. Siegel, R. L., Miller, K. D. & Jemal, A. Cancer statistics, 2019. *CA: A Cancer Journal for Clinicians* vol. 69 7–34 (2019).
53. Kamisawa, T., Wood, L. D., Itoi, T. & Takaori, K. Pancreatic cancer. *The Lancet* vol. 388 73–85 (2016).
54. Rahib, L. *et al.* Projecting cancer incidence and deaths to 2030: the unexpected burden of thyroid, liver, and pancreas cancers in the United States. *Cancer Res.* 74, 2913–2921 (2014).

55. Mohammad, A. A. Advanced pancreatic cancer: the standard of care and new opportunities. *Oncology Reviews* (2018) doi:10.4081/oncol.2018.370.
56. Serrati, S. *et al.* Next-generation sequencing: advances and applications in cancer diagnosis. *OncoTargets and Therapy* vol. 9 7355–7365 (2016).
57. Gagan, J. & Van Allen, E. M. Next-generation sequencing to guide cancer therapy. *Genome Medicine* vol. 7 (2015).
58. Paulsen, M. T. *et al.* Use of Bru-Seq and BruChase-Seq for genome-wide assessment of the synthesis and stability of RNA. *Methods* 67, 45–54 (2014).

CHAPTER II

ROS-Related Genes in Pancreatic Cancer

Pancreatic cancer, of which pancreatic ductal adenocarcinoma (PDAC) is the major subtype, remains a devastating disease lacking early diagnosis and effective treatment. Therefore, it is essential to discover novel biomarkers to facilitate disease-monitoring and new targets for drug discovery. A few studies have been conducted to identify and illustrate the complex ROS signaling pathways and to discover new biomarkers using various tools, including mass spectrometry-based proteomics, transcriptome sequencing, and computational modeling¹⁻⁵. A survival analysis of 73 known oxidative stress genes in a panel of cancer cells using the TCGA data portal revealed that FoxM1, thioredoxin, and superoxide dismutase genes may affect the overall survival of cancer patients¹. ROS-modulating compounds have shown potential applications in treating pancreatic cancer, and we aim to evaluate how ROS-related genes are involved in disease progression and survival^{6,7}. In this chapter, I used a combination of Bru-seq nascent RNA profiling and literature review to identify ROS-related genes and then qualify these genes as potential drug targets and biomarkers in pancreatic cancer patients using TCGA RNA-seq metadata.

Discovery of novel ROS-related genes in pancreatic cancer cells

I started with two lists of ROS-related genes. The first list (referred to as the Bru-seq gene list) was experimentally derived by exposing pancreatic cells to H₂O₂ and measuring the transcriptional response. MIA PaCa-2 cells were exposed to H₂O₂ at three concentrations (50 μM,

150 μ M, and 300 μ M) and then nascent RNA was profiled using Bru-seq. Upregulated (fold change > 2) and downregulated (fold change < 0.5) genes were combined to create a collection of experimentally derived ROS-related differentially expressed genes. The second list (referred to as the literature gene list) was derived from the reported ROS annotated gene sets. We collected 1,250 ROS-related genes by combining Molecular Signatures Database (MSigDB) ROS gene sets and references (Figure II-1).

Both the Bru-seq and literature genes were evaluated for association with patient disease progression and survival using the pancreatic adenocarcinoma (PAAD) cohort from TCGA. For disease progression, RNA-seq gene expression and patient tumor stage and grade were sourced from the GDAC Firehose. Patients were stratified into high and low categories by pathologic_stage, pathologic_t, and grade. Patient stages and grades were classified into high and low categories by combining patients with lower stage/grade (e.g. I/G1, G2) into a single group and comparing to patients with a higher stage/grade (e.g. II, III and IV/G3) into a single group. A Wilcoxon test was used to identify significant differences in log₂ RSEM gene expression values between categories and *p*-values were adjusted for multiple testing per disease. From the H₂O₂ Bru-seq gene list, we identified 189 genes with lower expression and 108 genes with higher expression in later stages of PDAC tumors. From the literature gene list, 41 were found to have lower expression in later stages of PDAC tumors while 56 had higher expression in later stage PDAC tumors (Figure II-1). We use “low genes” and “high genes” to indicate the association directionality between gene expression and worse patient progression or survival (respectively) in Figure II-1. Notably, there were nine common “low genes” and 12 common “high genes” between the two lists and Figure II-1B and 1C show the expression of the top three genes (ranked by fold change) in each category as stratified by pathological stage. Among the

nine common “low genes”, six of them are involved in response to oxidative stress (*XPA*, *ERCC8*, *FXN*, *SLC23A2*, *MAPK9*, and *PSIP1*), three are related to oxidative phosphorylation (*NDUFA11*, *ATP6V1H*, and *COX11*), and two regulate nucleotide excision repair (*XPA* and *ERCC8*), based on STRING analysis ⁸. For the 12 common “high genes”, six are linked to cellular response to oxygen-containing compounds (*EIF4EBP1*, *AGTRAP*, *ZC3H12A*, *NQO1*, *PSENI*, and *SLC9A1*), and eight are involved in the cellular response to chemical stimulus (*SQSTM1*, *EIF4EBP1*, *NQO1*, *SLC9A1*, *ZC3H12A*, *CAT*, *SDC4*, *PSENI*, and *MYBL2*). Below, we discuss the roles of these genes in ROS signaling and pancreatic cancer.

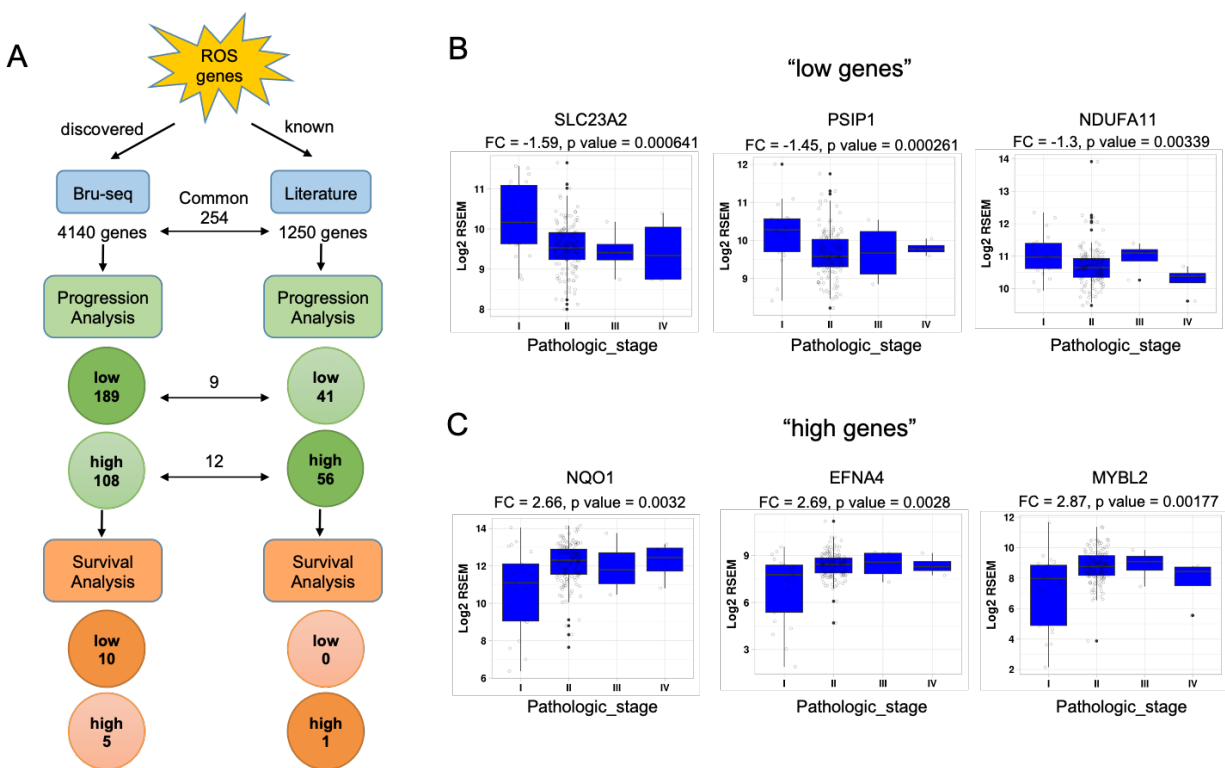


Figure II-1. Two arms of bioinformatics analysis identified ROS-signaling genes related to the progression and survival of pancreatic cancer patients. (A) Bru-seq, the left arm, was performed using 50 μ M, 150 μ M, and 300 μ M H₂O₂-treated MIA PaCa-2 cells for 4 h. Literature, the right arm, includes genes from known ROS gene sets and bioinformatics literature. The TCGA dataset was used for the progression and survival analysis. Low, the gene is significantly decreased in PDAC patients at later stages or with reduced survival rate. High, the gene is significantly overexpressed in PDAC patients at later stages or with reduced survival rate. Wilcoxon two sample test (p-adjusted < 0.05) was applied for progression analysis, and multi-threshold log rank test (q value < 0.05) and quartile-threshold cox proportional hazards test (q value < 0.05) were applied for the survival analysis. (B, C) The expression of top three genes in different pathological stages of TCGA_PAAD tumors. Low pathological stage: I; high pathological stage: II, III, IV. FC, fold change, calculated as mean log₂ RSEM of high stage over mean log₂ RSEM of low stage.

Progression analysis of ROS-related genes identified from two arms

SLC23A2 (FC = -1.59), *PSIP1* (FC = -1.45), and *NDUFA11* (FC = -1.3) are the top three genes with lowest gene expression in late-stage PDAC patients. *SLC23A2* (Solute Carrier Family 23 Member 2) is a vitamin C transporter regulating vitamin C absorption and uptake that affects the antioxidant system in response to ROS. *SLC23A2* is an important target for drug delivery across epithelial membranes, and its expression modulates drug uptake into the cells and may affect cancer treatment^{9,10}. Therefore, *SLC23A2* inhibition could enhance the permeability and bioavailability of anti-cancer drugs¹⁰. Moreover, polymorphisms of *SLC23A2* SNPs are related to chronic lymphocytic leukemia biology, clinical outcomes of chemo-drugs in esophageal squamous cell carcinoma patients, and gastric cancer risk^{11–13}. Our study demonstrates that *SLC23A2* expression is significantly correlated to pancreatic cancer progression, supporting its involvement in pancreatic cancer.

PSIP1 (PC4 and SFRS1 Interacting Protein 1) is a transcription coactivator that facilitates binding between RNA polymerase II and DNA to promote gene transcription. It shows elevated levels in metastatic invasive ductal carcinoma and is negatively correlated with the survival of triple-negative breast cancer (TNBC) patients¹⁴. Additionally, overexpression of *PSIP1* in prostate cancer cells reduced their sensitivity to lysosomal membrane permeabilization-inducing chemotherapies¹⁵. Moreover, it has been studied as a stress oncoprotein to protect

cancer cells from different environmental stressors, including oxidative stress¹⁶⁻¹⁸. Our analysis reveals that *PSIP1* has significantly lower expression in later stage TCGA PDAC tumors and H₂O₂ decreases its nascent transcripts.

NDUFA11 (NADH: Ubiquinone Oxidoreductase Subunit A11) encodes a subunit of the membrane-bound mitochondrial complex I, working as an NADH-ubiquinone reductase on the mitochondrial ETC^{19,20}. Mutation of *NDUFA11* may cause multiple diseases, such as neonatal lactic acidosis and cardiac disorders, due to defects in the respiratory chain²¹. Furthermore, *NDUFA11* SNPs are associated with heart rate variability that is related to cardiac morbidity and mortality²². *NDUFA11* expression was increased by long non-coding RNA *TERC* in lung squamous cell carcinoma^{22,23}. Our analysis shows that it is also related to pancreatic cancer progression and may represent a promising therapeutic target.

MYBL2 (FC = 2.87), *EFNA4* (FC = 2.69), and *NQO1* (FC = 2.66) are the top three genes with the highest fold change when comparing late stage to early stage PDAC tumors. *MYBL2* (MYB Proto-Oncogene Like 2) encodes a nuclear protein in the MYB family of transcription factors linked to cell cycle regulation. *MYBL2* is an essential upstream transcription factor of several genes related to cell proliferation in NSCLC, and its overexpression is associated with poor patient survival²⁴⁻²⁶. Its potential role as a drug target or biomarker has also been demonstrated in breast cancer²⁷, esophageal squamous cell carcinoma²⁸, and hepatocellular cancer^{28,29}. In pancreatic cancer patients, microRNA-29a (miR-29a) can downregulate *MYBL2* gene expression to regulate tumorigenesis³⁰. *MYBL2* is also a key downstream gene of Akt/FOXM1 signaling, and its overexpression promotes tumor progression in glioma³¹. Besides cancer, overexpression of MYBL2 protein improves cell viability and inhibits apoptosis in H9c2

cardiomyocytes³². In our analysis, we found higher *MYBL2* expression in later stage PDAC patients.

EFNA4 (Ephrin A4) is involved in the cell fate decisions of mammary epithelial cells³³. It also regulates the adhesion and cell death of the chronic lymphocytic leukemia cells³⁴. Overexpression of *EFNA4* in triple-negative breast cancer (TNBC), ovarian cancer, and pancreatic cancer is significantly associated with poor patient outcome^{35,36}. The knockdown of *EFNA4* inhibits the motility and invasion of pancreatic cancer cells by affecting the expression of epithelial (E)-cadherin and Snail proteins³⁷. Based on these findings, inhibitors of *EFNA4* have been developed to treat cancers. 2,5-dimethylpyrrolyl benzoic acid suppressed the EFNA4-Akt pathway and induced apoptosis in PDAC cells, demonstrating anti-tumor efficacy in an orthotopic PDAC mouse model³⁶. PF-06647263, a novel anti-EFNA4 antibody linked to a calicheamicin payload, showed limited anti-tumor activity in TNBC and ovarian cancer patients in a first-in-human, Phase I study³⁸. In our study, we show that *EFNA4* has increased expression in later stage PDAC. This finding suggests value in identifying more effective *EFNA4* inhibitors for clinical trials in pancreatic cancer.

NQO1 (NAD(P)H Quinone Dehydrogenase 1) is the most-well studied gene among all three genes associated with PDAC disease progression. It encodes a cytoplasmic two-electron reductase to detoxify and bioactivate quinone compounds³⁹. Elevated expression of *NQO1* in tumor tissues is closely related to tumor progression, aggressiveness, and poor patient prognosis in breast, lung, prostate and pancreatic cancer⁴⁰⁻⁴³. Agents inhibiting NQO1 activity have been developed and show anti-tumor effects *in vitro* and *in vivo*³⁹. One NQO1 inhibitor, β -lapachone (ARQ 501) and its analog are in Phase I and II clinical trials for cancer therapy, highlighting the potential role of NQO1 as a therapeutic target. Moreover, the combination of an NQO1 inhibitor

and anticancer drugs resulted in improved antitumor activity in multiple cancers ⁴⁴⁻⁴⁶. In our analysis, *NQO1* expression was significantly associated with stage progression in pancreatic cancer patients that is consistent with the literature. In Chapter III, we characterized a redox modulator similar to napabucasin in the transcriptomic profile and it may regulate mitochondrial proteins *via* NQO1.

PDAC disease progression analysis of ROS-signaling genes unique to the Bru-seq arm

Apart from understanding the roles of common genes between the Bru-seq arm and the literature arm, we also investigated differentially expressed genes that were unique to the Bru-seq arm, which may provide new information about ROS signaling essential for pancreatic cancer. Out of the 297 genes related to PDAC tumor progression, we focused on genes with clear Bru-seq trace diagrams and dose-dependent changes in response to H₂O₂. A total of 35 differentially expressed genes were selected based on manual inspection of Bru-seq trace diagrams for further analysis. In order to validate our discoveries from this sequencing arm, we also evaluated these genes on their association with disease progression in a separate pancreatic cancer study by Bailey *et al.* ⁴⁷. Nine out of 24 “high genes” and two out of 11 “low genes” displayed significant differential expression in later stage PDAC tumors in both datasets (Table II-1, Figure II-2).

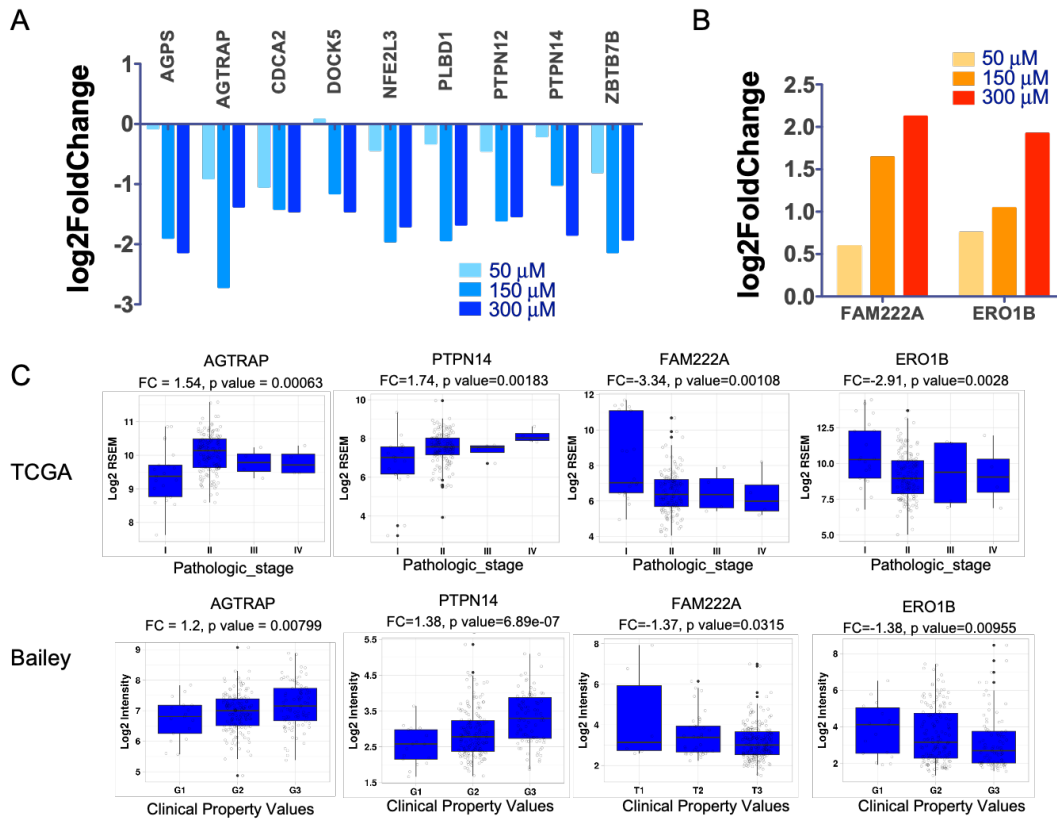


Figure II-2. Select genes are significantly associated with tumor progression in both TCGA and Bailey datasets and were regulated by H₂O₂. (A) Nine genes overexpressed in later stages of PDAC tumors were downregulated by H₂O₂. (B) Two genes downregulated in later stages of PDAC tumors were upregulated by H₂O₂. (C) Expression of select genes in different pathologic stages of TCGA_PAAD tumors.

Table II-1. Summary of genes significantly associated with PDAC tumor progression in each category. Datasets contain the TCGA and Bailey datasets. Low, lower expression in later stage tumors. High, higher expression in later stage tumors.

Category	Genes
Common between two arms	Low (9) <i>SLC23A2, PSIP1, NDUFA11, COX11, FXN, ATP6VIH, XPA, ERCC8, MAPK9</i>
	High (12) <i>MYBL2, EFNA4, NQO1, ZC3H12A, SDC4, SLC9A1, AGTRAP, EIF4EBP1, PSEN1, CAT, OXSRI, SQSTM1</i>
Unique in Bru-seq arm and validated in both datasets	Low (2) <i>FAM222A, ERO1B</i>
	High (9) <i>AGPS, AGTRAP, CDCA2, DOCK5, NFE2L3, PLBD1, PTPN12, PTPN14, ZBTB7B</i>

Among the nine overexpressed genes downregulated by H₂O₂ treatment, *AGPS* (Alkylglycerone Phosphate Synthase) encodes a FAD-binding protein from the oxidoreductase/transferase type 4 family. *AGPS* is a rate-limiting enzyme in plasmalogen synthesis, and its expression is affected by amyloid precursor protein levels and ROS production in Alzheimer's disease⁴⁸. *AGPS* protein is critical for ether lipid synthesis and is upregulated in multiple cancers, such as glioma and hepatic carcinoma^{49,50}. Knockdown of *AGPS* reduced expression of multi-drug resistance and anti-apoptosis proteins, leading to drug uptake and cancer cell death⁴⁹. Inhibition of *AGPS* also suppressed the migration of glioma U-87 MG cells⁵¹. Several inhibitors of *AGPS* have impaired cell proliferation, epithelial to mesenchymal transition (EMT), and migration, especially in cancers overexpressing *AGPS* protein^{52,53}. Our study is the first to show the upregulation of *AGPS* in later stage PDAC tumors and we suggest *AGPS* inhibitors may also be repurposed for pancreatic cancer treatment.

AGTRAP (Angiotensin II Receptor Associated Protein) is involved in the negative regulation of angiotensin II signaling *via* interaction with the angiotensin II type I receptor. Activation of aortic vascular *AGTRAP* can inhibit the ROS-p38 MAPK/JNK pathway and suppress pathological aortic hypertrophy⁵⁴. Additionally, knockout mice displayed age-related pathological changes in the kidney⁵⁵. *AGTRAP* is overexpressed in squamous cell carcinomas and melanoma tumors, but it has conflicting associations with disease prognosis^{56,57}. We observed upregulation of *AGTRAP* in later stage pancreatic cancer patients, suggesting its potential as a prognostic biomarker in pancreatic cancer.

CDCA2 (Cell Division Cycle Associated 2) is a cell cycle regulator related to cell proliferation and tumor progression. The relationship between *CDCA* proteins and ROS is not clear. *CDCA2* can promote cancer cell growth, and is upregulated in multiple cancers (colorectal

carcinoma, lung adenocarcinoma, and PDAC) and associated with tumor progression and prognosis⁵⁸⁻⁶⁰. More studies are needed to understand its cellular involvement in the ROS signaling pathways.

DOCK5 (Dedicator of Cytokinesis 5) is a guanine nucleotide exchange factor for small Rho family G proteins. Its spliced variant promoted proliferation, migration, and invasion of HPV-negative head and neck squamous cell carcinoma (HNSCC)⁶³. It works together with *DOCK2* to regulate chemotaxis, ROS production, and formation of extracellular traps in neutrophils⁶⁴. We observed a positive association of *DOCK2* expression with later stage tumors, implying possible biomarker relevance or therapeutic target potential.

The relationships between *PLBD1* (Phospholipase B Domain Containing 1), *ZBTB7B* (Zinc Finger and BTB Domain Containing 7B), and ROS are not clear. *PLBD1* was associated with the initiation and progression of carotid paragangliomas with a high mutation rate⁶⁵. *ZBTB7B* is a critical protein in mature CD4+ T cells that suppresses CD8-lineage gene expression, and it modulates thymic development and lymphomagenesis⁶⁶⁻⁶⁸. We identified a novel association of the expression of these genes and disease progression in two pancreatic cancer datasets to robustly support their relevance to pancreatic cancer disease.

PTPN12 (Protein Tyrosine Phosphatase Non-Receptor Type 12) and *PTPN14* (Protein Tyrosine Phosphatase Non-Receptor Type 14) encode protein tyrosine phosphatases that are drug targets for multiple cancers⁶⁹⁻⁷¹. The link between *PTPN14* and ROS signaling is not well understood, but some studies on its functions in cancers have been performed. Knockdown of *PTPN14* led to an increase in neuroblastoma cell migration and invasion; however, the opposite effect was observed in gastric cancer cells where the suppression of *PTPN14* inhibited EMT^{69,72}. In gastric cancer cells, *PTPN1* accelerated proliferation and migration by increasing the

phosphorylation of the oncoprotein Yes-associated protein (YAP) in the Hippo signaling pathway ⁷². Furthermore, PTPN14 overexpression correlated with low survival in colorectal cancer patients ⁷⁰. Conversely, a separate study determined that *PNPT14* was a tumor suppressor in the p53-PTPN14-YAP axis in pancreatic cancer ⁷¹. We believe further studies are needed to elucidate the connection between *PTPN14* and ROS signaling in pancreatic cancer.

FAM222A and *ERO1B* were validated in both TCGA and Bailey datasets, and their lower expression correlated with later stages of pancreatic cancer (Figure II-2). H₂O₂ was found to increase the transcription of these genes in MIA PaCa-2 cells, indicating a connection with ROS signaling. The function of *FAM222A* (Family with Sequence Similarity 222 Member A) is not fully understood in cancer and ROS signaling. *ERO1B* (Endoplasmic Reticulum Oxidoreductase 1 Beta) encodes an oxidoreductase involved in disulfide bond formation in the endoplasmic reticulum. *ERO1A* and *ERO1B* are two paralogs from the ERO1 family in higher eukaryotes ⁸⁰. *ERO1A* is ubiquitously expressed in multiple human tissues, while *ERO1B* is more exclusively in secretory tissues, such as the pancreas ⁸¹. ERO1 β is induced by unfolded protein stress and is approximately twice as active as ERO1 α as an oxidase ⁸². Knockdown of *ERO1B*, a downstream target of ATF6a, significantly increased the sensitivity of U2OS osteosarcoma cells to cisplatin treatment ⁸³. Low expression of *ERO1B* is associated with poor patient overall survival in pancreatic cancer, and it is increased in pancreatic neuroendocrine tumors ^{84,85}. In our study, we showed that *ERO1B* expression was upregulated in earlier stages/grades of PDAC tumors in the both datasets.

Survival analysis of ROS signaling genes in both arms

We identified that 16 genes were significantly associated with pancreatic cancer progression and patient survival. In the Bru-seq arm, the overexpression of *PTPN14* and

NFE2L3 (Nuclear Factor, Erythroid 2 Like 3) genes and lower expression of *ZNF547* and *KIAA1683* genes are significantly associated with a reduced survival rate in PDAC patients in the TCGA dataset (Figure II-3). *NFE2L3* (Nrf3) is in the same nuclear transcription factor family as Nrf2, which has been extensively investigated for its known roles in oxidative stress and cancer [88,89]. Nrf2 expression has been shown to increase promoter activity of peroxiredoxin 6, an antioxidant enzyme, while Nrf3 displayed opposite effects ⁷². Nrf3 is upregulated in multiple tumor samples compared to normal tissues, and promotes 20S proteasome assembly via increasing POMP expression, thus degrading the tumor suppressors p53 and Rb ^{73,74}. Silencing of *Nrf3* decreased cell proliferation and tumor growth in colorectal cancer by increasing DUK expression and inhibiting CDK1 activity ⁷⁵. Its downregulation also induced cell cycle arrest at the G0/G1 Phase in colorectal cancer ⁷⁶. In pancreatic cancer, we found increased expression of *Nrf3* was associated with reduced overall survival. Meanwhile, other studies have shown that *NFE2L3* was relevant to poor prognosis of pancreatic cancer patients when considering cumulative survival rate and disease-free survival ^{73,74}. Therefore, our analysis is consistent with current studies, supporting the potential role of *NFE2L3* as a therapeutic target or prognostic biomarker in PDAC. The biological functions of *ZNF547* (Zinc Finger Protein 547) and *KIAA1683* (IQCN, IQ Motif Containing N) are relatively unknown in cancer and ROS signaling. We believe these novel findings represent opportunities to further understand the connection between ROS signaling and poor pancreatic patient outcome.

KPNA4 (Karyopherin Subunit Alpha 4) is the only gene showing association with reduced patient survival and tumor progression from the literature arm. *KPNA4* is a downstream target of several microRNAs that are tumor suppressors and associated with poor prognosis and reduced survival of glioblastoma and hepatocellular carcinoma ^{86,87}. *KPNA4* protein is

overexpressed in cutaneous squamous cell carcinoma, and it increases cell proliferation and resistance to cisplatin⁸⁸. Additionally, inhibition of KPNA4 slowed the metastasis of prostate cancer⁸⁹. Therefore, *KPNA4* may be a worthy therapeutic target in cancers, including PDAC.

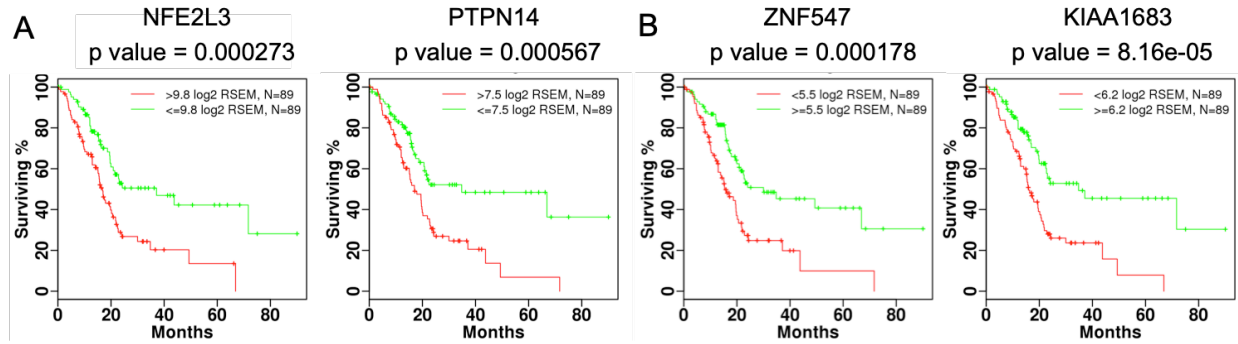


Figure II-3. Four genes are significantly related to the overall survival and progression of pancreatic cancer patients in the TCGA dataset from the Bru-seq gene list. (A) Higher expression of *NFE2L3* and *PTPN14* significantly correlates with reduced overall survival. (B) Lower expression of *ZNF547* and *KIAA1683* significantly correlates with decreased overall survival.

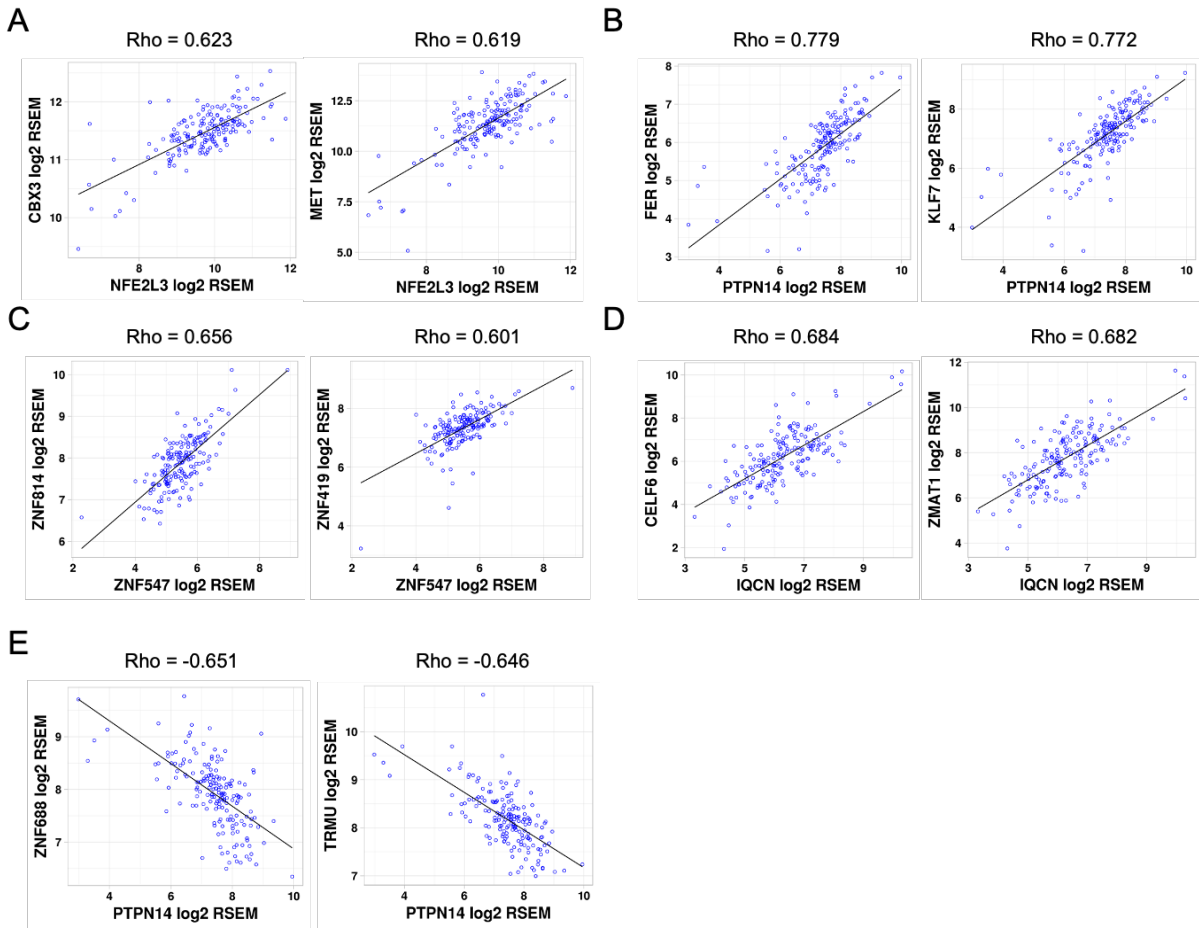
Correlation analysis of genes associated with PDAC progression and survival

In an effort to identify genes that are correlated with the four survival genes (*NFE2L3*, *PTPN14*, *ZNF547*, and *KIAA1683*) from the Bru-seq arm in the TCGA dataset, a correlation analysis was performed to further understand their roles in pancreatic cancer. Gene co-expression analysis can provide insight to transcriptional programs for which these genes participate and generate hypotheses for future experimental validation to reveal pathway interactions. Using log2 RSEM values from the TCGA PAAD cohort (N = 178), we calculated Spearman correlation to quantify the co-expression between these four genes and all other genes measured. Three genes (*CBX3*, *MET*, and *ECT2*) were positively correlated with *NFE2L3* with a *rho* value over 0.6 (Figure II-4A, 4F). Few studies delve into the biological relationship between these three genes and *NFE2L3*. *MET* is a candidate upstream oncogene of *ECT2*, and overexpression of *ECT2* in lung adenocarcinoma and glioblastoma is associated with poor patient survival^{5,90}. In the TCGA PAAD dataset, 128 genes were positively, and 22 genes were

negatively co-expressed with *PTPN14* (Figure II-4B, 4E, 4F). Protein-protein interaction analysis was conducted using STRING. The 128 genes positively correlated with *PTPN14* were enriched for KEGG pathways related to the regulation of actin cytoskeleton, focal adhesion, PI3K-Akt signaling, and RAS signaling, suggesting *PTPN14* may be involved in these pathways (Figure II-4G). This suggests that *PTPN14* may be involved in these pathways. Connections between *PTPN14* and focal adhesion, modulation of cell proliferation, migration, and invasion in cancers have been studied ^{69,72,91}. *YAPI* is the sixth most positively correlated gene, and its relationship with *PTPN14* has been described previously ⁷². The biological relationships between the top five positively co-expressed genes (*FER*, *KLF7*, *AHNAK*, *RSF1*, and *MINDY2*) and *PTPN14* remain unclear, and these relationships are worthy of future investigation. No KEGG pathways were significantly enriched for the negatively correlated genes.

ZNF547 and *KIAA1683/IQCN* are two genes associated with reduced survival and later stage of disease progression. We also determined that two genes (*ZNF814* and *ZNF419*) positively correlated with *ZNF547*, and 33 with *KIAA1683/IQCN* (Figure II-4C, 4D, 4F). The biological functions of *ZNF814* and *ZNF419* are poorly understood. One study identified *ZNF814* had significant mutations (c.1010C>T and a synonymous mutation) in familial hemangioblastomas ⁹². In HeLa cells, alternative splicing of *ZNF419* may remove a DNA-binding domain from the protein, thus affecting downstream cellular targets and functions ⁹³. Moreover, a polymorphism in the splice donor site of *ZNF419* resulted in the minor histocompatibility antigen ZAPHIR, which is involved in the specific CD8⁺ T cell responses in selective graft-versus-tumor immunity, thus *ZNF419* could be important in immunotherapy ⁹⁴. These findings provide candidate biological functions and cellular pathways that *ZNF547* may be involved in.

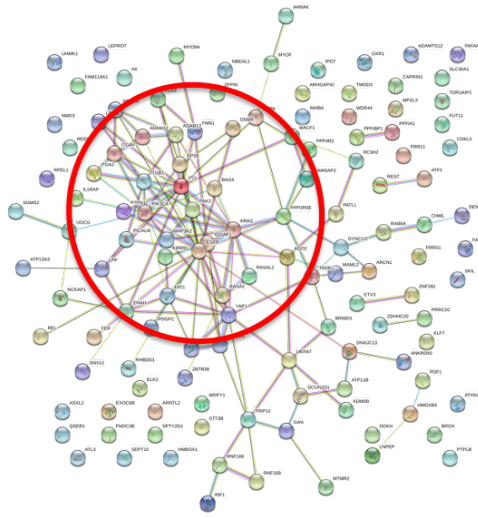
Of the 33 genes positively co-expressed with *KIAA1683/IQCN*, four contain an RNA-binding domain (*CELF6*, *CIRBP*, *RBM5*, and *SAFB2*). There are no significant KEGG pathways enriched from this gene list. The top two genes are *CELF6* and *ZMAT1*. *CELF6* is an RNA-binding protein that regulates cell proliferation and cell cycle in a p53- and/or p21-dependent manner, and it modulates p21 stability by binding to the 3'-UTR of p21 transcripts⁹⁵. In another study of the Xinjiang Uygur population, the minor allele “C” of rs4777498 in *CELF6* correlated with the increased risk of cervical cancer⁹⁶. *ZMAT1* has six transcripts, and three of them are protein-coding. *ZMAT1* transcript variant 2, a long non-coding RNA, is downregulated in gastric cancer tissue compared with adjacent normal tissue, and its expression is lower in advanced-stage disease and patients with shorter disease-free intervals⁹⁷. *KIAA1683/IQCN* may be related to these functional relationships and transcriptional regulation, but its detailed association with pancreatic cancer pathways remains to be determined.



F

Gene	Entrez ID	# of Positive Correlations	# of Negative Correlations
<i>NFE2L3</i>	9603	3	0
<i>PTPN14</i>	5784	128	22
<i>ZNF547</i>	284306	2	0
<i>KIAA1683/IQCN</i>	80726	33	0

G



KEGG pathway (FDR < 0.01)	Genes
actin cytoskeleton	<i>EGFR, ENAH, IQGAP1, ITGA2, ITGAV, ITGB1, KRAS, NCKAP1, PAK2, PDGFC, PIK3CA, VCL</i>
focal adhesion	<i>EGFR, ITGA2, ITGAV, ITGB1, PAK2, PDGFC, PIK3CA, VCL</i>
PI3K-Akt signaling	<i>ATF2, EGFR, ITGA2, ITGAV, ITGB1, KRAS, OSMR, PDGFC, PIK3CA, PPP2R5E</i>
RAS signaling	<i>EGFR, KRAS, PAK2, PDGFC, PIK3CA, RASA2, RASAL2, REL</i>

Figure II-4. Correlation analysis of *NFE2L3*, *PTPN14*, *ZNF547* and *KIAA1683/IQCN* in PDAC patients from TCGA database. (A-D) Top two genes with positive correlations with *NFE2L3*, *PTPN14*, *ZNF547* or *KIAA1683/IQCN*. (A) *NFE2L3*: *CBX3* and *MET*. (B) *PTPN14*: *FER* and *KLF7*. (C) *ZNF547*: *ZNF814* and *ZNF419*. (D) *KIAA1683/IQCN*: *CELF6* and *ZMAT1*. (E) Top two genes with negative correlations with *PTPN14*: *ZNF688* and *TRMU*. (F) Summary of all co-expressed genes. Genes with abstract correlation score ($|\rho|$) over 0.6 were counted as significant. Correlations were calculated using Spearman statistics on TCGA dataset, and the log₂ UQ normalized RSEM data were downloaded from GDAC Firehose. Gene expression is required in at least 50% of patients. (G) STRING analysis of 128 positively co-expressed genes with *PTPN14*. Red circle highlights the major enriched KEGG pathways as listed in the table.

Conclusions

Reactive oxygen species are essential signaling messengers in cancer cells and redox modulators continue to be investigated as promising anticancer agents. It is critical to understand the genes, pathways, and mechanisms involved in ROS signaling to effectively target and

harness the therapeutic potential of this important process. In this study, we used Bru-seq to profile the nascent RNA of H₂O₂-treated pancreatic cancer cells to discover novel ROS-related genes. We confirmed the clinical significance of genes involved in ROS signaling using several previously published pancreatic patient cohorts by quantifying association with pancreatic cancer disease progression and survival. Collectively, we identified nine genes with lower expression and 12 genes with higher expression in more advanced PDAC tumors from both arms, confirming their association with pancreatic cancer progression. More importantly, for the first time, we identified nine ROS-related genes with positive and two with negative associations with disease progression in both TCGA and Bailey pancreatic cancer datasets. In addition, three genes (*NFE2L3*, *PTPN14*, and *KPNA4*) had higher expression and two genes (*ZNF547* and *KIAA1683/IQCN*) had lower expression in TCGA patients with a reduced survival time. However, the survival analysis results were not supported by the Bailey dataset. These discrepancies may be due to different cohorts of pancreatic cancer patients, different subtypes of pancreatic cancer patients, and different measurement methods ^{47,98}. Overall, our findings combined with previous studies in various cancers suggest these genes represent prognostic biomarkers or therapeutic targets in pancreatic cancer, and further investigation into their biological function and signaling pathways is warranted.

Author contributions

Shuai Hu is the primary author, Armand Bankhead III made the progression boxplots and survival curves. Mats Ljungman's lab performed the Bru-seq experiments. Nouri Neamati is the corresponding author.

References

1. Leone, A., Roca, M. S., Ciardiello, C., Costantini, S. & Budillon, A. Oxidative Stress Gene Expression Profile Correlates with Cancer Patient Poor Prognosis: Identification of Crucial

- Pathways Might Select Novel Therapeutic Approaches. *Oxid. Med. Cell. Longev.* 2017, 2597581 (2017).
2. Pereira, E. J., Smolko, C. M. & Janes, K. A. Computational Models of Reactive Oxygen Species as Metabolic Byproducts and Signal-Transduction Modulators. *Front. Pharmacol.* 7, 457 (2016).
 3. Wang, R.-S., Oldham, W. M., Maron, B. A. & Loscalzo, J. Systems Biology Approaches to Redox Metabolism in Stress and Disease States. *Antioxid. Redox Signal.* 29, 953–972 (2018).
 4. Yuan, K. *et al.* Thiol-based redox proteomics in cancer research. *PROTEOMICS* vol. 15 287–299 (2015).
 5. Murata, Y. *et al.* ECT2 amplification and overexpression as a new prognostic biomarker for early-stage lung adenocarcinoma. *Cancer Sci.* 105, 490–497 (2014).
 6. Cohen, S. J. *et al.* A Phase 2 Randomized, Double-Blind, Multicenter Trial of Imexon Plus Gemcitabine Versus Gemcitabine Plus Placebo in Patients With Metastatic Chemotherapy-naïve Pancreatic Adenocarcinoma. *Am. J. Clin. Oncol.* 41, 230–235 (2018).
 7. Mohammad, J. *et al.* Piperlongumine potentiates the effects of gemcitabine in and human pancreatic cancer models. *Oncotarget* 9, 10457–10469 (2018).
 8. Szklarczyk, D. *et al.* STRING v11: protein-protein association networks with increased coverage, supporting functional discovery in genome-wide experimental datasets. *Nucleic Acids Res.* 47, D607–D613 (2019).
 9. Wang, C. *et al.* SVCT-2 determines the sensitivity to ascorbate-induced cell death in cholangiocarcinoma cell lines and patient derived xenografts. *Cancer Lett.* 398, 1–11 (2017).
 10. Khurana, V., Kwatra, D., Pal, D. & Mitra, A. K. Molecular expression and functional activity of vitamin C specific transport system (SVCT2) in human breast cancer cells. *Int. J. Pharm.* 474, 14–24 (2014).
 11. Casabonne, D. *et al.* Fruit and vegetable intake and vitamin C transporter gene (SLC23A2) polymorphisms in chronic lymphocytic leukaemia. *Eur. J. Nutr.* 56, 1123–1133 (2017).
 12. Minegaki, T. *et al.* Genetic polymorphisms in SLC23A2 as predictive biomarkers of severe acute toxicities after treatment with a definitive 5-fluorouracil/cisplatin-based chemoradiotherapy in Japanese patients with esophageal squamous cell carcinoma. *Int. J. Med. Sci.* 11, 321–326 (2014).
 13. Duell, E. J. *et al.* Vitamin C transporter gene (SLC23A1 and SLC23A2) polymorphisms, plasma vitamin C levels, and gastric cancer risk in the EPIC cohort. *Genes Nutr.* 8, 549–560 (2013).
 14. Singh, D. K. *et al.* PSIP1/p75 promotes tumorigenicity in breast cancer cells by promoting the transcription of cell cycle genes. *Carcinogenesis* 38, 966–975 (2017).
 15. Ríos-Colón, L. *et al.* Targeting the stress oncoprotein LEDGF/p75 to sensitize chemoresistant prostate cancer cells to taxanes. *Oncotarget* 8, 24915–24931 (2017).

16. Matsui, H., Lin, L. R., Singh, D. P., Shinohara, T. & Reddy, V. N. Lens epithelium-derived growth factor: increased survival and decreased DNA breakage of human RPE cells induced by oxidative stress. *Invest. Ophthalmol. Vis. Sci.* 42, 2935–2941 (2001).
17. Singh, D. P., Fatma, N., Kimura, A., Chylack, L. T., Jr & Shinohara, T. LEDGF binds to heat shock and stress-related element to activate the expression of stress-related genes. *Biochem. Biophys. Res. Commun.* 283, 943–955 (2001).
18. Basu, A. *et al.* LEDGF/p75 Overexpression Attenuates Oxidative Stress-Induced Necrosis and Upregulates the Oxidoreductase ERP57/PDIA3/GRP58 in Prostate Cancer. *PLoS One* 11, e0146549 (2016).
19. Žárský, V. & Doležal, P. Evolution of the Tim17 protein family. *Biol. Direct* 11, 54 (2016).
20. Andrews, B., Carroll, J., Ding, S., Fearnley, I. M. & Walker, J. E. Assembly factors for the membrane arm of human complex I. *Proc. Natl. Acad. Sci. U. S. A.* 110, 18934–18939 (2013).
21. Berger, I. *et al.* Mitochondrial complex I deficiency caused by a deleterious NDUFA11 mutation. *Ann. Neurol.* 63, 405–408 (2008).
22. Nolte, I. M. *et al.* Genetic loci associated with heart rate variability and their effects on cardiac disease risk. *Nat. Commun.* 8, 15805 (2017).
23. Wu, X., Ruan, L., Yang, Y. & Mei, Q. Identification of crucial regulatory relationships between long non-coding RNAs and protein-coding genes in lung squamous cell carcinoma. *Mol. Cell. Probes* 30, 146–152 (2016).
24. Ahmed, F. Integrated Network Analysis Reveals FOXM1 and MYBL2 as Key Regulators of Cell Proliferation in Non-small Cell Lung Cancer. *Front. Oncol.* 9, 1011 (2019).
25. Musa, J., Aynaud, M.-M., Mirabeau, O., Delattre, O. & Grünewald, T. G. P. MYBL2 (B-Myb): a central regulator of cell proliferation, cell survival and differentiation involved in tumorigenesis. *Cell Death & Disease* vol. 8 e2895–e2895 (2017).
26. Fan, X. *et al.* B-Myb Mediates Proliferation and Migration of Non-Small-Cell Lung Cancer via Suppressing IGFBP3. *International Journal of Molecular Sciences* vol. 19 1479 (2018).
27. Zhou, Q. *et al.* Co-expression network analysis identified candidate biomarkers in association with progression and prognosis of breast cancer. *J. Cancer Res. Clin. Oncol.* 145, 2383–2396 (2019).
28. Qin, H. *et al.* Prognostic implications and oncogenic roles of MYBL2 protein expression in esophageal squamous-cell carcinoma. *Onco. Targets. Ther.* 12, 1917–1927 (2019).
29. Guan, Z., Cheng, W., Huang, D. & Wei, A. High MYBL2 expression and transcription regulatory activity is associated with poor overall survival in patients with hepatocellular carcinoma. *Curr Res Transl Med* 66, 27–32 (2018).
30. Dey, S. *et al.* miR-29a is repressed by MYC in pancreatic cancer and its restoration drives tumor suppressive effects via downregulation of LOXL2. *Mol. Cancer Res.* (2019) doi:10.1158/1541-7786.MCR-19-0594.
31. Zhang, X., Lv, Q.-L., Huang, Y.-T., Zhang, L.-H. & Zhou, H.-H. Akt/FoxM1 signaling

- pathway-mediated upregulation of MYBL2 promotes progression of human glioma. *J. Exp. Clin. Cancer Res.* 36, 105 (2017).
32. Shao, M., Ren, Z. & Zhang, R. MYBL2 protects against H9c2 injury induced by hypoxia via AKT and NF- κ B pathways. *Mol. Med. Rep.* 17, 4832–4838 (2018).
 33. Burleigh, A. *et al.* A co-culture genome-wide RNAi screen with mammary epithelial cells reveals transmembrane signals required for growth and differentiation. *Breast Cancer Res.* 17, 4 (2015).
 34. Flores, M. A. *et al.* EphrinA4 plays a critical role in α 4 and α L mediated survival of human CLL cells during extravasation. *Oncotarget* vol. 7 (2016).
 35. Damelin, M. *et al.* Anti-EFNA4 Calicheamicin Conjugates Effectively Target Triple-Negative Breast and Ovarian Tumor-Initiating Cells to Result in Sustained Tumor Regressions. *Clin. Cancer Res.* 21, 4165–4173 (2015).
 36. Takano, H. *et al.* Inhibition of Eph receptor A4 by 2,5-dimethylpyrrolyl benzoic acid suppresses human pancreatic cancer growing orthotopically in nude mice. *Oncotarget* 6, 41063–41076 (2015).
 37. Liu, C., Huang, H., Wang, C., Kong, Y. & Zhang, H. Involvement of ephrin receptor A4 in pancreatic cancer cell motility and invasion. *Oncol. Lett.* 7, 2165–2169 (2014).
 38. Garrido-Laguna, I. *et al.* First-in-human, phase I study of PF-06647263, an anti-EFNA4 calicheamicin antibody-drug conjugate, in patients with advanced solid tumors. *Int. J. Cancer* 145, 1798–1808 (2019).
 39. Zhang, K. *et al.* NAD(P)H:Quinone Oxidoreductase 1 (NQO1) as a Therapeutic and Diagnostic Target in Cancer. *J. Med. Chem.* 61, 6983–7003 (2018).
 40. Yang, Y. *et al.* Clinical implications of high NQO1 expression in breast cancers. *J. Exp. Clin. Cancer Res.* 33, 14 (2014).
 41. Li, Z. *et al.* NQO1 protein expression predicts poor prognosis of non-small cell lung cancers. *BMC Cancer* 15, 207 (2015).
 42. Sun, Z., Cui, Y., Pei, J. & Fan, Z. Association between NQO1 C609T polymorphism and prostate cancer risk. *Tumour Biol.* 35, 7993–7998 (2014).
 43. Awadallah, N. S. *et al.* NQO1 expression in pancreatic cancer and its potential use as a biomarker. *Appl. Immunohistochem. Mol. Morphol.* 16, 24–31 (2008).
 44. Mizumoto, A. *et al.* Combination treatment with highly bioavailable curcumin and NQO1 inhibitor exhibits potent antitumor effects on esophageal squamous cell carcinoma. *J. Gastroenterol.* 54, 687–698 (2019).
 45. Chen, J. *et al.* Mesoporous Silica Nanoparticle-Based Combination of NQO1 Inhibitor and 5-Fluorouracil for Potent Antitumor Effect Against Head and Neck Squamous Cell Carcinoma (HNSCC). *Nanoscale Res. Lett.* 14, 387 (2019).
 46. Zhang, L. *et al.* β -Lapachone and Paclitaxel Combination Micelles with Improved Drug Encapsulation and Therapeutic Synergy as Novel Nanotherapeutics for NQO1-Targeted Cancer Therapy. *Mol. Pharm.* 12, 3999–4010 (2015).

47. Bailey, P. *et al.* Genomic analyses identify molecular subtypes of pancreatic cancer. *Nature* 531, 47–52 (2016).
48. Grimm, M. O. W. *et al.* Plasmalogen synthesis is regulated via alkyl-dihydroxyacetonephosphate-synthase by amyloid precursor protein processing and is affected in Alzheimer's disease. *J. Neurochem.* 116, 916–925 (2011).
49. Zhu, Y. *et al.* Alkylglyceronephosphate synthase (AGPS) alters lipid signaling pathways and supports chemotherapy resistance of glioma and hepatic carcinoma cell lines. *Asian Pac. J. Cancer Prev.* 15, 3219–3226 (2014).
50. Zhu, Y. *et al.* Role and mechanism of the alkylglycerone phosphate synthase in suppressing the invasion potential of human glioma and hepatic carcinoma cells in vitro. *Oncol. Rep.* 32, 431–436 (2014).
51. Zhang, Y. *et al.* Tudor-staphylococcal nuclease regulates the expression and biological function of alkylglycerone phosphate synthase via nuclear factor- κ B and microRNA-127 in human glioma U87MG cells. *Oncol. Lett.* 15, 9553–9558 (2018).
52. Piano, V. *et al.* Discovery of Inhibitors for the Ether Lipid-Generating Enzyme AGPS as Anti-Cancer Agents. *ACS Chem. Biol.* 10, 2589–2597 (2015).
53. Stazi, G. *et al.* Development of alkyl glycerone phosphate synthase inhibitors: Structure-activity relationship and effects on ether lipids and epithelial-mesenchymal transition in cancer cells. *Eur. J. Med. Chem.* 163, 722–735 (2019).
54. Wakui, H. *et al.* Activation of angiotensin II type 1 receptor-associated protein exerts an inhibitory effect on vascular hypertrophy and oxidative stress in angiotensin II-mediated hypertension. *Cardiovasc. Res.* 100, 511–519 (2013).
55. Uneda, K. *et al.* Angiotensin II Type 1 Receptor-Associated Protein Regulates Kidney Aging and Lifespan Independent of Angiotensin. *J. Am. Heart Assoc.* 6, (2017).
56. Zeng, H., Li, H., Zhao, Y., Chen, L. & Ma, X. Transcripto-based network analysis reveals a model of gene activation in tongue squamous cell carcinomas. *Head & Neck* vol. 41 4098–4110 (2019).
57. Loftus, S. K. *et al.* Hypoxia-induced HIF1 α targets in melanocytes reveal a molecular profile associated with poor melanoma prognosis. *Pigment Cell Melanoma Res.* 30, 339–352 (2017).
58. Shi, R. *et al.* CDCA2 promotes lung adenocarcinoma cell proliferation and predicts poor survival in lung adenocarcinoma patients. *Oncotarget* 8, 19768–19779 (2017).
59. Feng, Y. *et al.* CDCA2 promotes the proliferation of colorectal cancer cells by activating the AKT/CCND1 pathway in vitro and in vivo. *BMC Cancer* 19, 576 (2019).
60. Wang, M.-Y. *et al.* Prognostic Impact of Cell Division Cycle Associated 2 Expression on Pancreatic Ductal Adenocarcinoma. *Chin. Med. Sci. J.* 31, 149–154 (2016).
61. Wang, H. *et al.* CDCA7 promotes lung adenocarcinoma proliferation via regulating the cell cycle. *Pathol. Res. Pract.* 215, 152559 (2019).
62. Jiménez-P, R. *et al.* CDCA7 is a critical mediator of lymphomagenesis that selectively

- regulates anchorage-independent growth. *Haematologica* 103, 1669–1678 (2018).
63. Liu, C. *et al.* Characterization of Alternative Splicing Events in HPV-Negative Head and Neck Squamous Cell Carcinoma Identifies an Oncogenic DOCK5 Variant. *Clin. Cancer Res.* 24, 5123–5132 (2018).
 64. Watanabe, M. *et al.* DOCK2 and DOCK5 act additively in neutrophils to regulate chemotaxis, superoxide production, and extracellular trap formation. *J. Immunol.* 193, 5660–5667 (2014).
 65. Snezhkina, A. V. *et al.* Novel Genes Associated with the Development of Carotid Paragangliomas. *Molecular Biology* vol. 53 547–559 (2019).
 66. Wang, L. *et al.* The zinc finger transcription factor Zbtb7b represses CD8-lineage gene expression in peripheral CD4+ T cells. *Immunity* 29, 876–887 (2008).
 67. Lee, H.-O. *et al.* Disregulated expression of the transcription factor ThPOK during T-cell development leads to high incidence of T-cell lymphomas. *Proc. Natl. Acad. Sci. U. S. A.* 112, 7773–7778 (2015).
 68. Tokunaga, T. *et al.* Regulation of Th-POK and Runx3 in T cell development in human thymoma. *Autoimmunity* vol. 42 653–660 (2009).
 69. Chen, G., Yang, Z., Feng, M. & Wang, Z. microRNA-217 suppressed epithelial-to-mesenchymal transition through targeting PTPN14 in gastric cancer. *Biosci. Rep.* 40, (2020).
 70. Martinez-Romero, J., Bueno-Fortes, S., Martín-Merino, M., Ramirez de Molina, A. & De Las Rivas, J. Survival marker genes of colorectal cancer derived from consistent transcriptomic profiling. *BMC Genomics* 19, 857 (2018).
 71. Mello, S. S. *et al.* A p53 Super-tumor Suppressor Reveals a Tumor Suppressive p53-Ptpn14-Yap Axis in Pancreatic Cancer. *Cancer Cell* 32, 460–473.e6 (2017).
 72. Han, X. *et al.* Nonreceptor tyrosine phosphatase 14 promotes proliferation and migration through regulating phosphorylation of YAP of Hippo signaling pathway in gastric cancer cells. *J. Cell. Biochem.* 120, 17723–17730 (2019).
 73. Ma, Q. Role of Nrf2 in Oxidative Stress and Toxicity. *Annual Review of Pharmacology and Toxicology* vol. 53 401–426 (2013).
 74. Cloer, E. W., Goldfarb, D., Schrank, T. P., Weissman, B. E. & Major, M. B. NRF2 Activation in Cancer: From DNA to Protein. *Cancer Res.* 79, 889–898 (2019).
 75. Chowdhury, I. *et al.* Oxidant stress stimulates expression of the human peroxiredoxin 6 gene by a transcriptional mechanism involving an antioxidant response element. *Free Radic. Biol. Med.* 46, 146–153 (2009).
 76. Kobayashi, A. & Waku, T. New addiction to the NRF2-related factor NRF3 in cancer cells: Ubiquitin-independent proteolysis through the 20S proteasome. *Cancer Science* vol. 111 6–14 (2020).
 77. Wang, H. *et al.* Elevated expression of NFE2L3 predicts the poor prognosis of pancreatic cancer patients. *Cell Cycle* 17, 2164–2174 (2018).

78. Bury, M. *et al.* NFE2L3 Controls Colon Cancer Cell Growth through Regulation of DUX4, a CDK1 Inhibitor. *Cell Rep.* 29, 1469–1481.e9 (2019).
79. Zhang, L. *et al.* NFE2L3 Inhibition Induces Cell Cycle Arrest at the G0/G1 Phase in Colorectal Cancer Cells through Downregulating CCND1 and pRb1-ser807/811. *Dis. Markers* 2019, 2829798 (2019).
80. Shergalis, A. G., Hu, S., Bankhead, A., 3rd & Neamati, N. Role of the ERO1-PDI interaction in oxidative protein folding and disease. *Pharmacol. Ther.* 107525 (2020).
81. Araki, K. & Inaba, K. Structure, mechanism, and evolution of Ero1 family enzymes. *Antioxid. Redox Signal.* 16, 790–799 (2012).
82. Wang, L., Zhu, L. & Wang, C.-C. The endoplasmic reticulum sulfhydryl oxidase Ero1 β drives efficient oxidative protein folding with loose regulation. *Biochem. J* 434, 113–121 (2011).
83. Yarapureddy, S. *et al.* ATF6 α Activation Enhances Survival against Chemotherapy and Serves as a Prognostic Indicator in Osteosarcoma. *Neoplasia* 21, 516–532 (2019).
84. Zhu, T. *et al.* Genome-scale analysis identifies GJB2 and ERO1LB as prognosis markers in patients with pancreatic cancer. *Oncotarget* 8, 21281–21289 (2017).
85. Xie, J. *et al.* The Immunohistochemical Evaluation of Solid Pseudopapillary Tumors of the Pancreas and Pancreatic Neuroendocrine Tumors Reveals ERO1L β as a New Biomarker. *Medicine* 95, e2509 (2016).
86. Wang, H. *et al.* Upregulation of miR-181s reverses mesenchymal transition by targeting KPNA4 in glioblastoma. *Sci. Rep.* 5, 13072 (2015).
87. Wang, Z. *et al.* Reanalysis of microRNA expression profiles identifies novel biomarkers for hepatocellular carcinoma prognosis. *Tumour Biol.* 37, 14779–14787 (2016).
88. Zhang, M., Luo, H. & Hui, L. MiR-3619-5p hampers proliferation and cisplatin resistance in cutaneous squamous-cell carcinoma via KPNA4. *Biochem. Biophys. Res. Commun.* 513, 419–425 (2019).
89. Yang, J. *et al.* Inhibition of KPNA4 attenuates prostate cancer metastasis. *Oncogene* 36, 2868–2878 (2017).
90. Sahlia, B. *et al.* The guanine nucleotide exchange factors trio, Ect2, and Vav3 mediate the invasive behavior of glioblastoma. *Am. J. Pathol.* 173, 1828–1838 (2008).
91. Po’uha, S. T. *et al.* Stathmin levels alter PTPN14 expression and impact neuroblastoma cell migration. *Br. J. Cancer* (2019) doi:10.1038/s41416-019-0669-1.
92. Ma, D. *et al.* Whole exome sequencing identified genetic variations in Chinese hemangioblastoma patients. *Am. J. Med. Genet. A* 173, 2605–2613 (2017).
93. Martin, G. *et al.* Allele-specific splicing effects on DKKL1 and ZNF419 transcripts in HeLa cells. *Gene* 598, 107–112 (2017).
94. Broen, K. *et al.* A polymorphism in the splice donor site of ZNF419 results in the novel renal cell carcinoma-associated minor histocompatibility antigen ZAPHIR. *PLoS One* 6,

e21699 (2011).

95. Liu, G. *et al.* RNA-binding protein CELF6 is cell cycle regulated and controls cancer cell proliferation by stabilizing p21. *Cell Death Dis.* 10, 688 (2019).
96. Fang, J. *et al.* Correlation between polymorphisms in microRNA-regulated genes and cervical cancer susceptibility in a Xinjiang Uygur population. *Oncotarget* vol. 8 (2017).
97. Lai, Y. *et al.* Downregulation of long noncoding RNA ZMAT1 transcript variant 2 predicts a poor prognosis in patients with gastric cancer. *Int. J. Clin. Exp. Pathol.* 8, 5556–5562 (2015).
98. Cancer Genome Atlas Research Network. Electronic address: andrew_aguirre@dfci.harvard.edu & Cancer Genome Atlas Research Network. Integrated Genomic Characterization of Pancreatic Ductal Adenocarcinoma. *Cancer Cell* 32, 185–203.e13 (2017).

CHAPTER III

A Novel Redox Modulator Induces a GPX4-mediated Cell Death Dependent on Iron and Reactive Oxygen Species

Previously, we developed a series of quinazolinedione-based ROS inducers that were tested for utility in pre-clinical models of pancreatic cancer (Chart 1). In this study, we show for the first time that QD394 displayed highly similar transcriptomic profiles with napabucasin, suggesting similar downstream signaling effects. Combinations with cell death signaling inhibitors revealed that QD394 induced ferroptosis but not caspase-dependent apoptosis, necroptosis, or autophagy. We further demonstrate that QD394 induces lipid peroxidation, iron-, ROS-, and glutathione peroxidase 4 (GPX4)-mediated cell death, all of which are closely related to ferroptosis. Ferroptosis was first identified in 2012 to represent an iron-dependent regulated cell death with increased lipid peroxidation ¹. Intrinsic mechanisms of ferroptosis depend on the activity of phospholipid peroxidase GPX4 and lipid peroxidation ^{2,3}. At least four classes of ferroptosis inducers have been developed, including (1) SLC7A11 inhibitor (erastin), (2) GPX4 inhibitor (RSL3), (3) FIN56 (depleting GPX4 protein), and (4) FINO₂ (indirectly inhibiting GPX4) ². Ferroptosis inducers show synergistic anti-tumor effects with select chemotherapies ⁴ and sensitize cancer cells to radiation ⁵. We also observed synergy between QD394 and select FDA-approved drugs, suggesting that combination studies with redox modulators as ferroptosis inducers could be a viable approach to treat pancreatic cancer.

Additionally, we performed proteomics analysis and observed a significant decrease in LRPPRC and PNPT1 expression, two proteins involved in mitochondrial RNA catabolic processes. The expression of these two genes is negatively correlated with the survival of pancreatic cancer patients. Furthermore, a pharmacokinetics (PK)-guided lead optimization campaign was conducted to develop a QD394 analog, QD394-Me, with improved PK properties.

Results

QD394 shows remarkable similarity to napabucasin and H₂O₂ in transcriptomic profiles

Among 11 originally synthesized analogs, QD394 had the highest cytotoxicity in MIA PaCa-2 cells and similar cytotoxicity in PANC-1 and BxPC-3 cells (Table III-1). I have also tested QD394 in HPNE and HFF-1 cell lines, and its IC₅₀ values are 2-fold higher than that in MiaPaca-2. QD394 induced the highest level of intracellular ROS after 1 h compound treatment (Figure III-S1). To better elucidate its mechanism of action, we performed Bru-seq, which is a nascent RNA-seq technique that uses bromouridine to label newly synthesized RNAs⁶. This method detects immediate changes in the transcriptome caused by drugs to aid in the understanding of the potential mechanisms of action. We discovered that the transcriptomic profile of QD394 was highly similar to that of napabucasin and H₂O₂. The shrunkenLFC (shrunken log₂FoldChange) of genes in QD394 Bru-seq samples significantly correlated with that of the napabucasin ($r = 0.92$) and H₂O₂ ($r = 0.88$) samples, indicating similar transcription regulation (Figure III-1A). ShrunkenLFC reduces the effect of low-expressing genes resulting in over-inflated Log₂FoldChange values. Gene Set Enrichment Analysis (GSEA) revealed 82 upregulated and 51 downregulated enriched gene sets in common between QD394 and napabucasin Bru-seq samples using the C2 curated gene sets from Molecular Signatures

(MSigDB) Database v7.0 with FDR below 0.001 (Figure III-1B, C). For the Hallmark and KEGG pathway gene sets shared between QD394 and napabucasin, TNFA signaling, UV response, and hypoxia hallmark gene sets were upregulated, and RNA degradation KEGG gene set was downregulated (Figure III-1D, E). TNF signaling and ROS are interconnected in the regulation of cell homeostasis, survival, and death in inflammatory diseases and cancers. ROS is closely related to TNF-related downstream signaling, such as NF- κ B and JNK activation, and TNF can induce antioxidant NRF2 pathway to protect cells from elevated ROS ⁷. UV radiation can cause DNA damage and corresponding cell death *via* oxidative stress ^{8,9}. Moreover, cellular and mitochondrial ROS activate a series of transcription factors (TFs), which trigger the expression of a number of genes involved in the hypoxic response ^{10,11}. It is interesting to note that QD394 affects RNA degradation in the KEGG pathway gene set, and this is consistent with our proteomics study (see below).

Since napabucasin is a STAT3 signaling inhibitor and exhibited a similar transcriptomic profile as QD394, we sought to determine whether QD394 affected STAT3 signaling. Indeed, QD394 inhibited the phosphorylation of STAT3 in MIA PaCa-2 and PANC-1 cells, and it increased the phosphorylation of H2AX, a DNA damage biomarker (Figure III-1F).

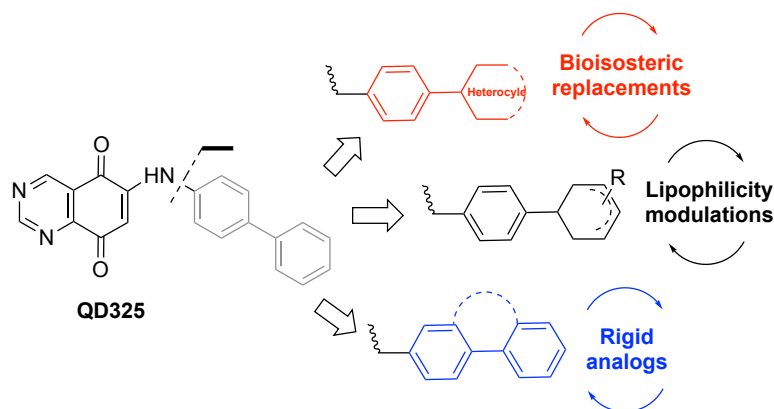


Chart 1. Design of novel quinazolinone-based ROS modulators.

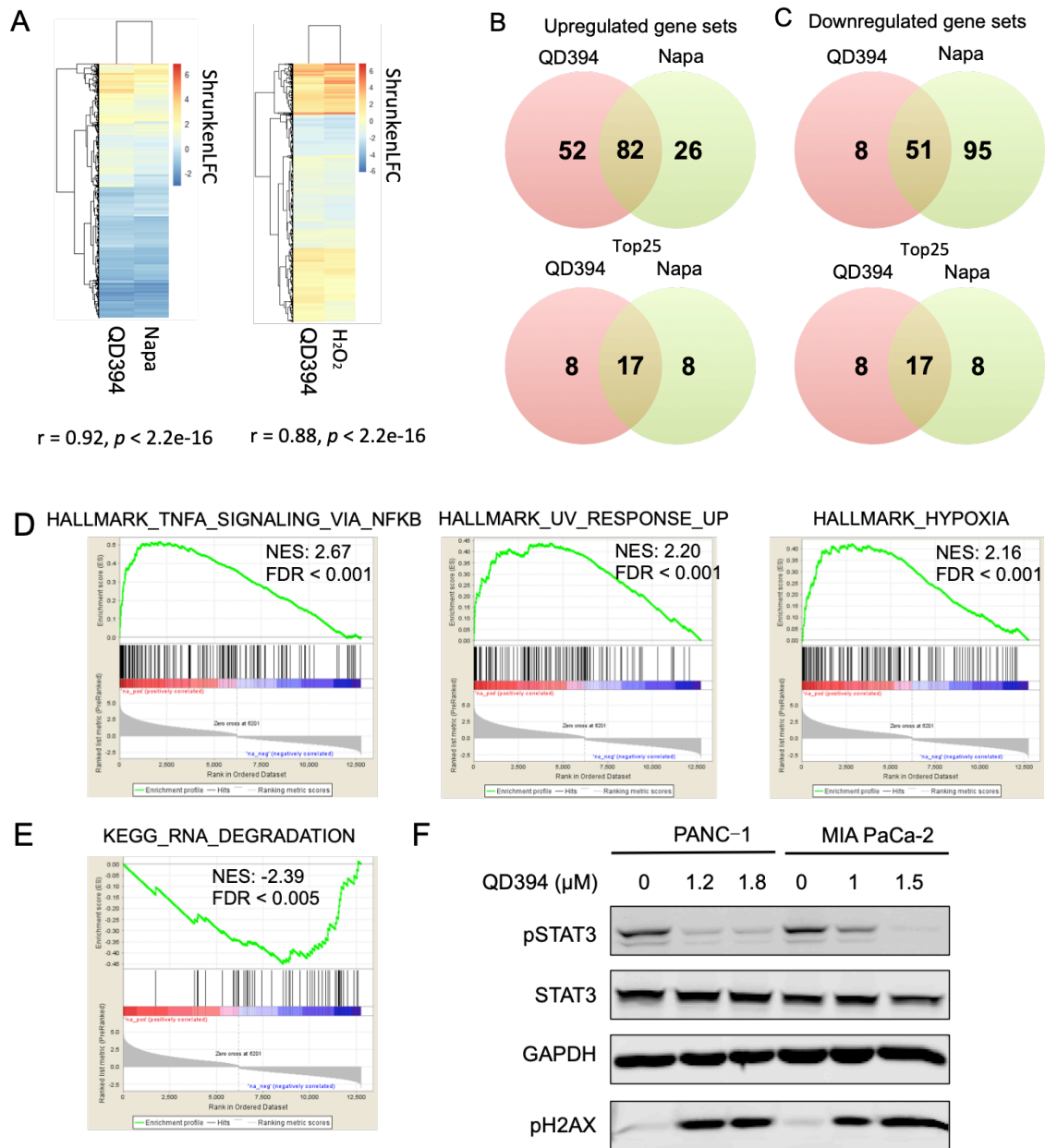


Figure III-1. Transcriptomic profile of QD394 is similar to that of napabucasin (napa) and H_2O_2 . (A) Pearson correlation between QD394, napabucasin, and H_2O_2 samples calculated in R. ShrunkenLFC was used to build heatmaps. (B, C) Upregulated and downregulated gene sets in GSEA from QD394 and napabucasin Bru-seq samples. GSEA plots of upregulated (D) and downregulated (E) enriched gene sets from the QD394 samples that are shared with napabucasin are depicted. FDR < 0.001. NES, normalized enrichment score. (F) Cells were treated with QD394 for 4 h at indicated concentrations and analyzed by immunoblot with STAT3, pSTAT3, GAPDH, and pH2AX antibodies.

Table III-1. Cytotoxicity of QD compounds in MIA PaCa-2, PANC-1, and BxPC-3 cancer cell lines. The IC₅₀ (μM) is shown as mean ± sd. Mean and standard deviation were calculated from three independent experiments.

ID	IC ₅₀ (μM)		
	MIA PaCa-2	PANC-1	BxPC-3
QD385	2.4 ± 0.1	2.3 ± 0.3	5.1 ± 1.4
QD386	9.7 ± 4.0	4.4 ± 1.9	10.1 ± 2.8
QD387	3.1 ± 0.2	1.9 ± 0.2	3.3 ± 1.4
QD388	2.4 ± 0.6	1.4 ± 0.5	2.5 ± 0.9
QD389	1.5 ± 0.3	0.8 ± 0.3	2.3 ± 0.4
QD390	3.1 ± 1.5	4.7 ± 1.5	4.5 ± 0.6
QD391	2.2 ± 0.7	1.6 ± 0.8	2.6 ± 0.3
QD392	1.5 ± 0.7	2.3 ± 0.3	1.6 ± 0.6
QD393	1.2 ± 0.2	0.9 ± 0.4	0.5 ± 0.1
QD394	0.64 ± 0.04	0.34 ± 0.03	0.9 ± 0.2
QD395	2.0 ± 0.7	0.8 ± 0.2	2.7 ± 0.4
QD394-Me	3.63 ± 0.37	0.38 ± 0.01	0.87 ± 0.15

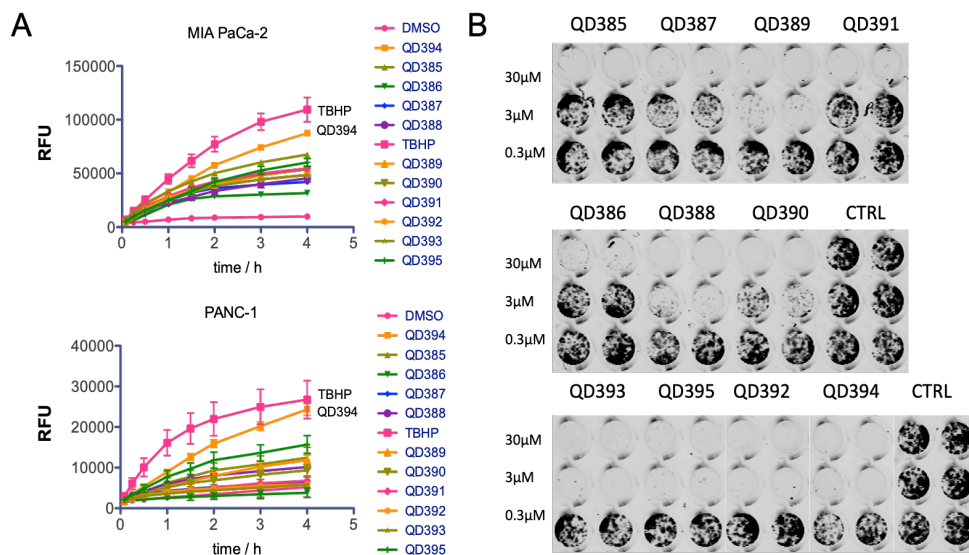


Figure III-S1. Characterization of originally synthesized QD394 analogs. (A) ROS-inducing capability of 11 QD394 analogs measured by CM-H2DCFDA dye in MIA PaCa-2 and PANC-1 cells. RFU, relative fluorescence unit. All analogs were tested at 10 μM, and tert-butyl hydroperoxide (TBHP) was tested at 200 μM. (B) QD394 is one of the most potent compounds in the colony formation assay in MIA PaCa-2 cells.

QD394 induces ROS-mediated cell death and decreases the GSH/GSSG ratio

As a redox modulator, QD394 caused time-dependent cellular ROS accumulation within the first 4-hour treatment in MIA PaCa-2 cells (Figure III-2A). The significant increase of ROS level could be reduced in 30 minutes by the antioxidant N-acetylcysteine (NAC) (Figure III-2B). Additionally, NAC significantly increased the IC₅₀ of QD394 from 0.53 μM to 1.11 μM (Figure III-2C) and rescued colony formation inhibition by QD394 (Figure III-2D). Thus, the cytotoxicity of QD394 is partially dependent on ROS induction.

Glutathione is a well-known cellular ROS scavenger. In the GSH/GSSG-Glo assay, QD394 significantly decreased the GSH/GSSG ratio at both 2 h and 4 h treatment, similar to napabucasin (Figure III-2E). The decrease of ratio is due to reduced GSH level or increased GSSG level or both. The reduction from QD394 treatment was caused by oxidation of GSH to GSSG, rather than the direct decrease of GSH level (Figure III-S2). BSO is an inhibitor of GSH synthesis, and both napabucasin and buthionine sulfoximine (BSO) significantly lowered GSH level (Figure III-2E, S2).

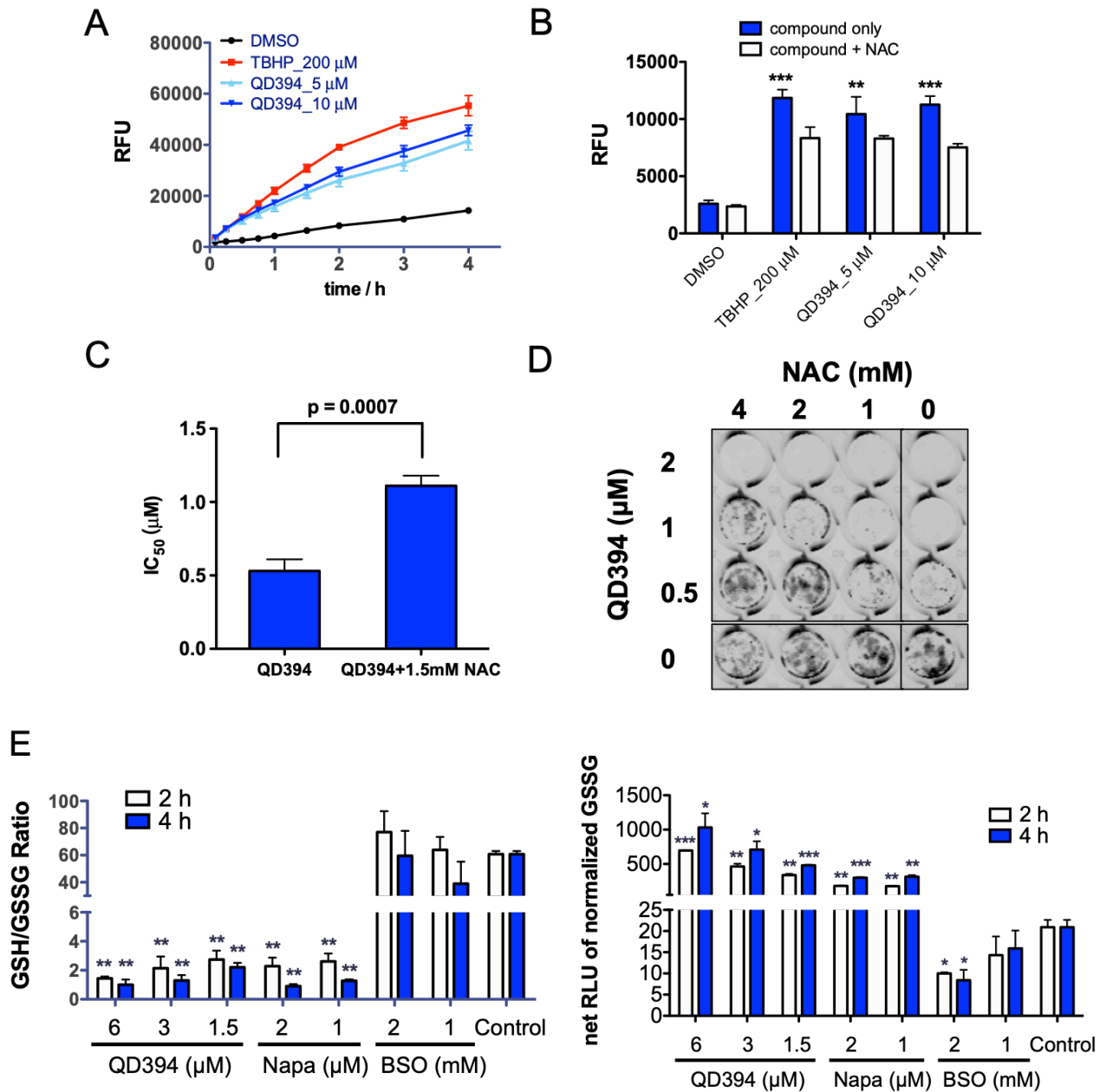


Figure III-2. QD394 increases cellular ROS level and reduces GSH/GSSG ratio in MIA PaCa-2 cells. (A) QD394 increased fluorescence (RFU) indicating cellular ROS generation across treatment time (0 - 4 h). TBHP was used as a positive control. (B) At 30 min, significant increase of ROS was determined in QD394- and TBHP-treated cells, and NAC (3 mM) reduced the elevated ROS levels. ** denotes $p < 0.005$, *** denotes $p < 0.0005$. (C) NAC significantly decreased the cytotoxicity of QD394 in the MTT assay. (D) NAC protected the inhibition of colony formation caused by QD394. (E) QD394 reduced cellular GSH/GSSG ratio mainly resulting from GSSG formation. RLU, relative luminescence unit. * denotes $p < 0.05$, ** denotes $p < 0.005$, *** denotes $p < 0.0005$.

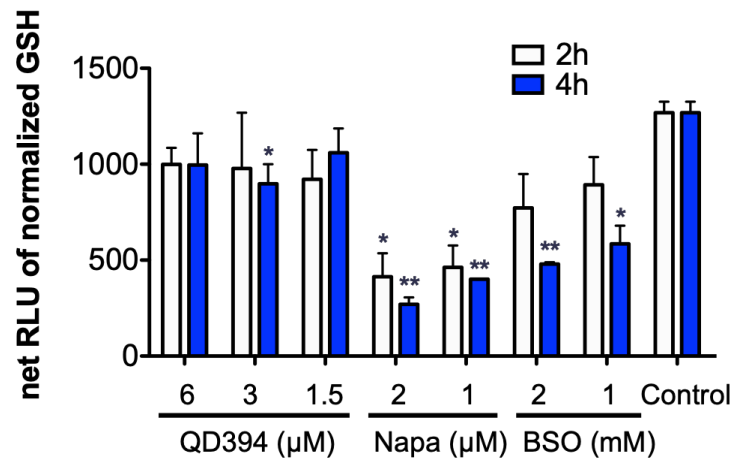


Figure III-S2. QD394 did not change GSH level significantly, but napabucasin and BSO did. RLU, relative luminescence unit. * denotes $p < 0.05$, ** denotes $p < 0.005$, *** denotes $p < 0.0005$.

QD394 causes iron-dependent and GPX4-mediated cell death

Since we observed that QD394 modulated the GSH/GSSG ratio and its cytotoxicity was dependent on ROS, we hypothesized that QD394 could induce ferroptosis. To determine the cell death mechanism, we combined QD394 with a panel of signaling inhibitors (Table III-2). We identified that deferoxamine (DFO) and deferasirox, two iron chelators, prevented cell death caused by QD394, indicating iron is a contributing factor for its cytotoxicity (Figure III-3A, S3). Two known ferroptosis inhibitors had different effects on cell death rescue. Liproxstatin-1 modestly rescued cell death caused by QD394, while ferrostatin-1 did not. Z-VAD (a caspase-dependent apoptosis inhibitor) and necrostatin-1 (a necroptosis inhibitor) did not rescue cell death, and chloroquine (an autophagy inhibitor) slightly rescued cell death in the colony formation assay (Figure III-S3). Interestingly, necrostatin-1 blocked the inhibition of colony formation caused by napabucasin, indicating that cell death by napabucasin may proceed *via* necroptosis. The link between napabucasin and necroptosis has not been reported previously.

Moreover, these results demonstrate that QD394 and napabucasin have different cell death mechanisms.

The final step in ferroptosis is an increase in lipid peroxidation¹⁻⁵. We measured the lipid ROS level in QD394-treated cells using the BODIPY C11 dye to validate QD394-induced ferroptosis cell death. QD394 significantly increased lipid ROS in a dose-dependent manner (Figure III-3B). TBHP (an ROS inducer), RSL3 (a GPX4 inhibitor), and erastin (an SLC7A11 inhibitor) all increased lipid ROS. Besides iron and lipid peroxidation, GPX4 is another central mediator of ferroptosis. GPX4 catalyzes the reduction of hydrogen peroxide, organic hydroperoxides, and lipid hydroperoxides, and thereby protects cells against oxidative damage¹². Therefore, we investigated whether there is a connection between QD394 and GPX4. In the cellular thermal shift assay (CETSA), QD394 destabilized GPX4 protein, indicated by the reduction in its melting temperature (from 60.34 °C to 57.62 °C) in MIA PaCa-2 cells (Figure III-3C). The destabilization of GPX4 by QD394 was also observed in PANC-1 cells (Figure III-S4). Binding to a protein generally stabilizes it, however, QD394 destabilizes GPX4 and it may be caused by an alternative binding mode or indirect interaction between them. Furthermore, the cytotoxicity of QD394 was significantly decreased in MIA PaCa-2 cells with GPX4 knocked down using siRNA, further suggesting that QD394 regulates GPX4-mediated cell death (Figure III-3D). Additionally, QD394 rescued the cytotoxicity of RSL3 in pancreatic cancer cells, suggesting that QD394 targets GPX4 (Figure III-3E). In summary, QD394 induces an iron-dependent and GPX4-mediated cell death, which is closely related to ROS induction.

Table III-2. Select cell death inhibitors that were combined with QD394 in pancreatic cancer cells.

Cell death	Target	Inhibitor
Apoptosis	All caspases	Z-VAD-FMK
Necroptosis	RIP1 kinase	Necrostatin-1
	Selective inhibitor of RIP1	Necrostatin-1s
Ferroptosis	Iron; iron-dependent prolyl hydroxylases; lysosomal ROS inhibitor by chelating lysosomal redox-active iron	Deferoxamine (DFO), deferasirox
	Inhibit autooxidation of lipids by trapping peroxy radicals; not rescue H ₂ O ₂ -induced cell death	Ferrostatin-1
	Inhibit ferroptosis induced by L-buthionine sulphoximine (BSO), erastin and (1S,3R)-RSL3; inhibit autooxidation of lipids by trapping peroxy radicals	Liproxstatin-1
Autophagy	Impair autophagosome fusion with lysosomes	Chloroquine
	Inhibit PI3K activity and the initial phase of the autophagic process	3-Methyladenine
Parthanatos	PARP inhibitors	Olaparib
	AIF release inhibitors	N-phenylmaleimide

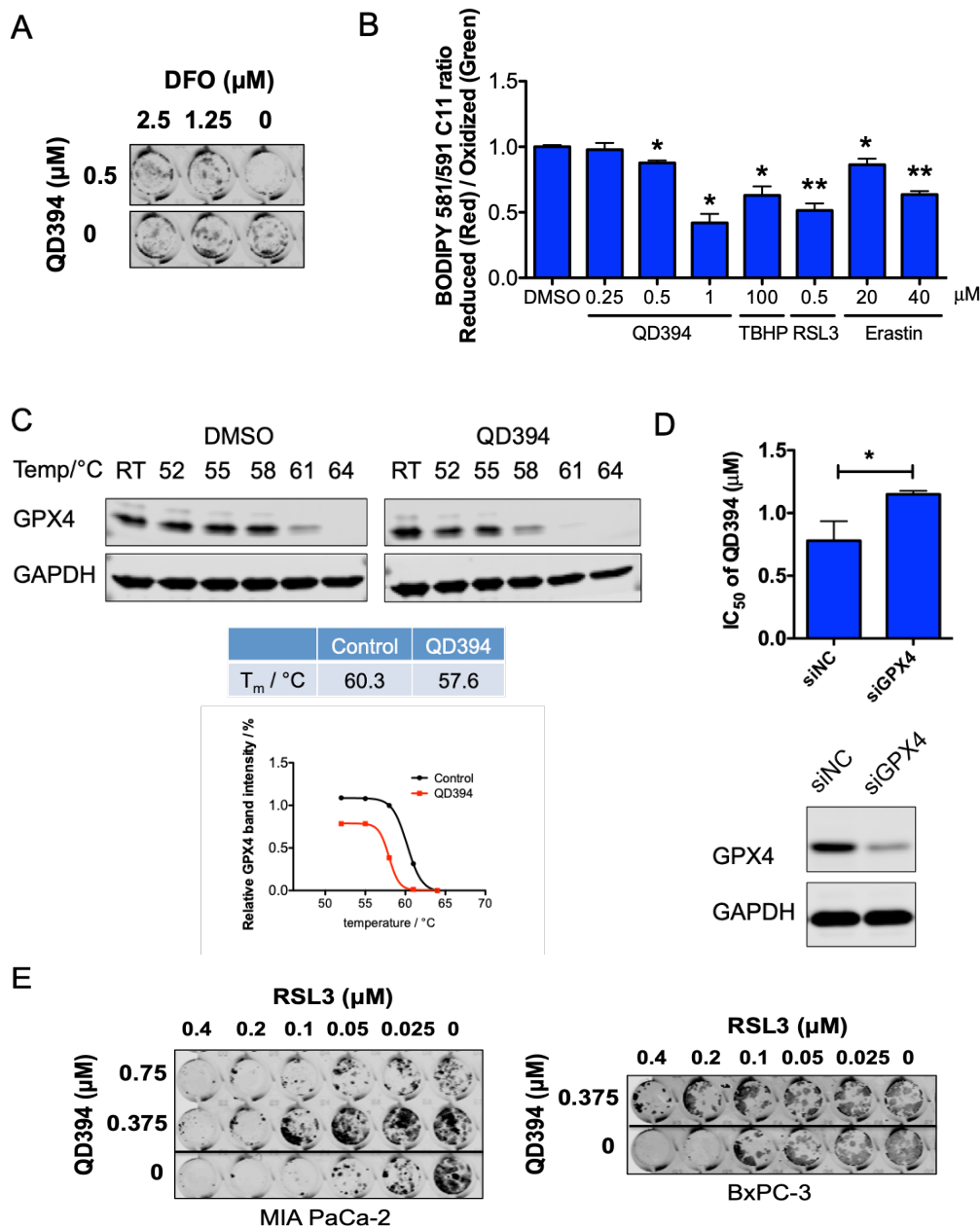


Figure III-3. QD394 induces iron-dependent and GPX4-mediated ferroptosis in MIA PaCa-2 cells. (A) DFO decreased the inhibition of colony formation caused by QD394. (B) QD394 significantly induced lipid peroxidation after 24 h treatment, similar to TBHP, RSL3, and erastin. * denotes $p < 0.05$, ** denotes $p < 0.005$. (C) The potential interaction between QD394 and GPX4 was determined by cellular thermal shift assay. Detailed procedures are described in the methods section. QD394 decreased the melting temperature of GPX4 protein by quantification using Image J and GraphPad Prism. QD394 was tested at 100 μM for 1 h. RT: room temperature, around 21 $^{\circ}\text{C}$. (D) Knockdown of GPX4 significantly reduced cytotoxicity of QD394. siNC: samples treated with scramble siRNA; siGPX4: samples treated with GPX4 siRNA. * denotes $p < 0.05$. Cells were immunoblotted with GPX4 antibody to validate GPX4 knockdown. (E) RSL3 inhibited colony formation in pancreatic cancer cells, and QD394 rescued its effect.

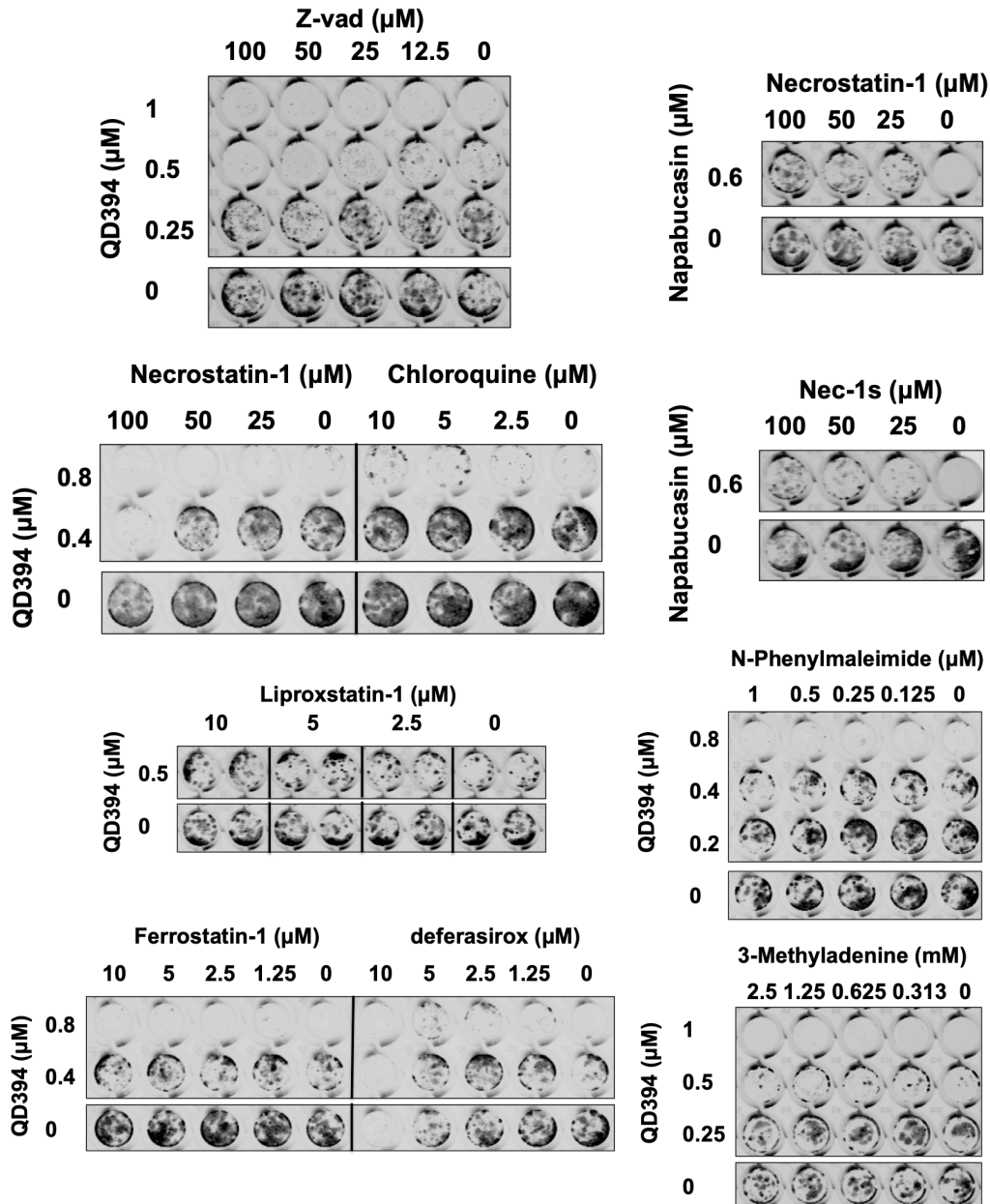


Figure III-S3. Combination studies between QD394, napabucasin, and cell death inhibitors in MIA PaCa-2 cells.

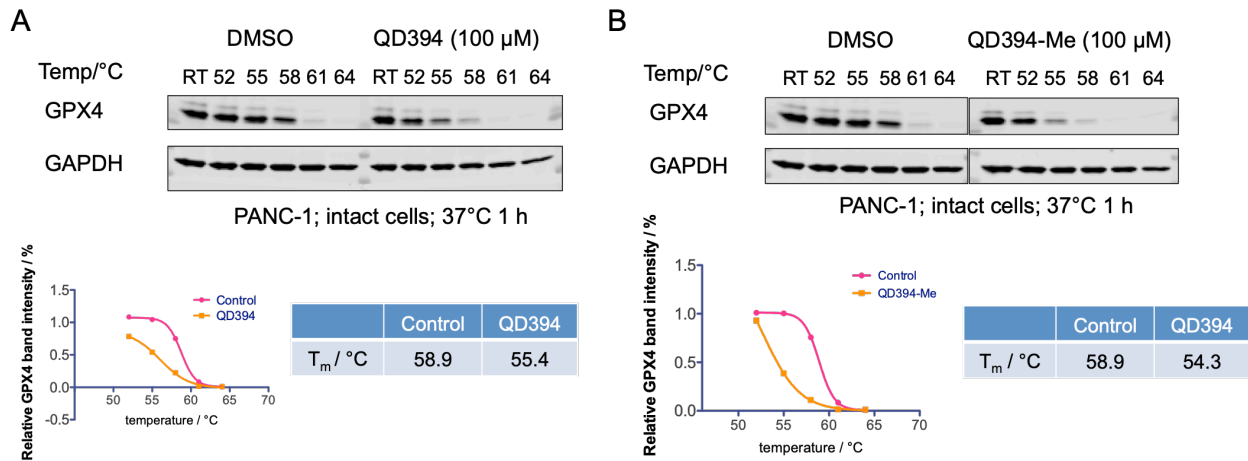


Figure III-S4. QD394 and QD394-Me reduced the melting temperature of GPX4 in PANC-1 cells. (A) QD394. (B) QD394-Me. RT: around 21 °C.

QD394 interferes with mitochondrial gene expression and RNA catabolic process

To further investigate the Bru-seq results at the protein level, we performed proteomics and measured the changes caused by QD394. QD394 increased the expression of 84 proteins and decreased the expression of 146 proteins by at least 1.5-fold (FDR < 0.05) after 24 h treatment in MIA PaCa-2 cells with duplicates. There are 17 upregulated and 35 downregulated genes/proteins in common between the proteomics and Bru-seq analysis (Figure III-4A). In the STRING analysis¹³, the 17 proteins with increased expression were involved in the response to endoplasmic reticulum (ER) stress, the unfolded protein response, and the transcription from RNA polymerase II promoter related to oxidative stress (Table III-3). Furthermore, the 35 proteins with decreased protein expression had a close connection with mitochondrial genes, mitochondrial translation regulation, and cellular metabolic processes (Table III-4, Figure III-4B). QD394 reduced expression of proteins involved in mitochondrial RNA catabolic processes, which is consistent with the Bru-seq GSEA analysis showing that QD394 downregulated the KEGG RNA degradation gene set. We observed that LRPPRC and PNPT1 are involved in many

of the biological processes downregulated by QD394 (Table III-4). *LRPPRC* (Leucine Rich Pentatricopeptide Repeat Containing) encodes a protein localized primarily to mitochondria, and it may regulate RNA metabolism and transcription in both nuclei and mitochondria. *PNPT1* (Polyribonucleotide Nucleotidyltransferase 1) encodes a mitochondrial intermembrane protein in the polynucleotide phosphorylase family comprised of phosphate-dependent 3'-to-5' exoribonucleases implicated in RNA processing and degradation. More importantly, we discovered that high expression of both genes significantly correlated with reduced overall survival of pancreatic cancer patients in the TCGA PAAD dataset (Figure III-4C). In the 24 h proteomics experiment, QD394 reduced the expression of these two proteins (FDR < 0.05); additionally, QD394 significantly decreased their expression at 4 h (Figure III-4D). Napabucasin also decreased the protein expression of these two genes at 4 h, while H₂O₂ did not. We combined NAC and dicoumarol (an NQO1 inhibitor) with QD394 and napabucasin to assess the effects on the expression of LRPPRC and PNPT1 (Figure III-S5). NAC did not affect the downregulation of these two proteins caused by QD394 and napabucasin; however, dicoumarol blocked the reduction, indicating that NQO1 is a potential regulator in this process. Therefore, in PANC-1 cells, which have little intrinsic NQO1 expression, we did not observe the downregulation of LRPPRC and PNPT1 proteins by QD394 and napabucasin (Figure III-S5).

Besides these two mitochondrial proteins related to RNA processing, QD394 also reduced the expression of other mitochondrial proteins in the proteomics study, substantiating its possible role in affecting mitochondrial function (Figure III-4E). Overall, QD394 downregulated mitochondrial proteins, including LRPPRC and PNPT1 in both Bru-seq and proteomics experiments.

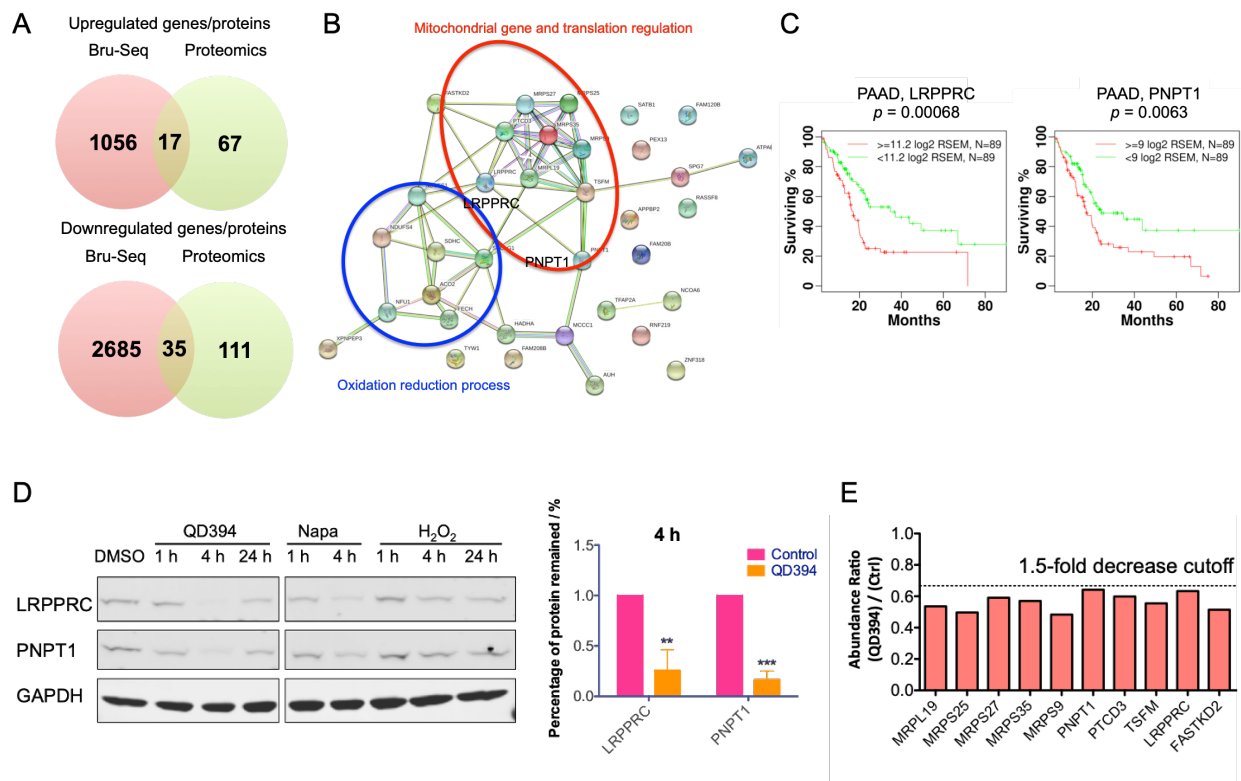


Figure III-4. Common genes/proteins between Bru-seq and proteomics analysis reveal that QD394 interferes with mitochondrial gene expression and RNA catabolic process. (A) Venn diagrams of upregulated and downregulated genes/proteins between Bru-seq (fold change over 2) and proteomics (fold change over 1.5) analysis. (B) STRING analysis of 35 downregulated genes/proteins in common between Bru-seq and proteomics studies. Red circle highlights the genes involved in mitochondrial gene and translation regulation. Blue circle indicates the genes associated with the oxidation reduction process. (C) LRPPRC and PNPT1 are significantly related to the overall survival of pancreatic adenocarcinoma patients in TCGA dataset. (D) QD394 decreased the protein expression of LRPPRC and PNPT1 in MIA PaCa-2 cells. QD394 and napabucasin were tested at $3 \times IC_{50}$ for 1 h and 4 h. QD394 was tested at $2 \times IC_{50}$ for 24 h. H₂O₂ was used at 150 μ M. * denotes $p < 0.05$, ** denotes $p < 0.005$, *** denotes $p < 0.0005$. (E) The expression of mitochondrial proteins decreased in the QD394-treated MIA PaCa-2 cells.

Table III-3. STRING analysis of 17 upregulated genes/proteins in common between Bru-seq and proteomics. Biological process GO terms are ranked by FDR.

Biological Process (GO)	Count	FDR	Matching proteins
response to endoplasmic reticulum stress	5	0.0018	ASNS,CTH,HSPA5,PPP1R15A, SESN2
cellular response to glucose starvation	3	0.003	ASNS,HSPA5,SESN2
negative regulation of response to stimulus	8	0.0055	CD55,CTH,HMOX1,HSPA5, PPP1R15A,RIOK3,SERPINE1, SESN2
negative regulation of immune effector process	3	0.0078	CD55,HMOX1,RIOK3
response to stress	10	0.0078	ASNS,CD55,CTH,HMOX1, HSPA5,IFRD1,PPP1R15A, RIOK3, SERPINE1,SESN2
negative regulation of signal transduction	7	0.0078	CTH,HMOX1,HSPA5, PPP1R15A,RIOK3,SERPINE1, SESN2
endoplasmic reticulum unfolded protein response	3	0.0078	ASNS,CTH,HSPA5
cellular response to nutrient levels	4	0.0078	ASNS,HMOX1,HSPA5,SESN2
PERK-mediated unfolded protein response	2	0.0078	ASNS,HSPA5
negative regulation of apoptotic process	6	0.0078	ASNS,CBX4,CTH,HMOX1, HSPA5,SERPINE1
regulation of translation in response to stress	2	0.0078	PPP1R15A,SESN2
regulation of transcription from RNA polymerase II promoter in response to stress	3	0.0078	HMOX1,HSPA5,SESN2
regulation of transcription from RNA polymerase II promoter in response to oxidative stress	2	0.0078	HMOX1,SESN2
negative regulation of cellular process	12	0.0078	ASNS,CBX4,CD55,CTH, HMOX1,HSPA5,IFRD1,JUND, PPP1R15A,RIOK3,SERPINE1, SESN2
cellular response to chemical stimulus	9	0.0078	ASNS,CTH,HMOX1,HSPA5, JUND,RIOK3,SERPINE1, SESN2,ZFAND2A
cellular response to arsenic-containing substance	2	0.0078	HMOX1,ZFAND2A
negative regulation of endoplasmic reticulum unfolded protein response	2	0.0078	HSPA5,PPP1R15A
regulation of PERK-mediated unfolded protein response	2	0.0078	HSPA5,PPP1R15A

aspartate family amino acid biosynthetic process	2	0.0079	ASNS,CTH
response to organic substance	9	0.0082	ASNS,CTH,HMOX1,HSPA5,JUND,PLIN2,RIOK3,SERPINE1,SESN2

Table III-4. STRING analysis of 35 downregulated genes/proteins in common between Bru-seq and proteomics. Biological process GO terms are ranked by FDR. PNPT1 and LRPPRC are labeled in red.

Biological Process (GO)	Count	FDR	Matching proteins
mitochondrial gene expression	8	1.04E-07	MRPL19,MRPS25,MRPS27,MRPS35,MRPS9,PNPT1,PTCD3,TSFM
mitochondrial translational elongation	7	1.16E-07	MRPL19,MRPS25,MRPS27,MRPS35,MRPS9,PTCD3,TSFM
mitochondrial translational termination	6	2.58E-06	MRPL19,MRPS25,MRPS27,MRPS35,MRPS9,PTCD3
regulation of mitochondrial translation	4	1.74E-05	FASTKD2,LRPPRC,MRPS27,TSFM
cellular respiration	6	2.73E-05	ACO2,FASTKD2,NDUFS1,NDUFS4,SDHC,SUCLG1
oxidation-reduction process	10	0.0002	ACO2,AUH,FASTKD2,HADHA,NDUFS1,NDUFS4,PEX13,SDHC,SUCLG1,TYW1
generation of precursor metabolites and energy	7	0.00026	ACO2,FASTKD2,FECH,NDUFS1,NDUFS4,SDHC,SUCLG1
metabolic process	30	0.00029	ACO2,AUH,FAM120B,FAM20B,FASTKD2,FECH,HADHA,LRPPRC,MCCC1,MRPL19,MRPS25,MRPS27,MRPS35,MRPS9,NCOA6,NDUFS1,NDUFS4,NFU1,PEX13,PNPT1,PTCD3,SATB1,SDHC,SPG7,SUCLG1,TFAP2A,TSFM,TYW1,XPNPEP3,ZNF318
peptide metabolic process	7	0.001	MRPL19,MRPS25,MRPS27,MRPS35,MRPS9,PTCD3,TSFM
cellular metabolic process	28	0.001	ACO2,AUH,FAM120B,FAM20B,FASTKD2,FECH,HADHA,LRPPRC,MCCC1,MRPL19,MRPS25,MRPS27,MRPS35,MRPS9,NCOA6,NDUFS1,NDUFS4,NFU1,PEX13,PNPT1,PTCD3,SATB1,SDHC,SUCLG1,TFAP2A,TSFM,TYW1,ZNF318
tricarboxylic acid cycle	3	0.0012	ACO2,SDHC,SUCLG1
cellular amide metabolic process	8	0.0012	MCCC1,MRPL19,MRPS25,MRPS27,MRPS35,MRPS9,PTCD3,TSFM
protein-containing complex subunit organization	12	0.0012	ATPAF1,FASTKD2,MCCC1,MRPL19,MRPS25,MRPS27,MRPS35,MRPS9,NDUFS1,NDUFS4,PNPT1,PTCD3

regulation of mitochondrial RNA catabolic process	2	0.0014	LRPPRC,PNPT1
citrate metabolic process	3	0.0014	ACO2,SDHC,SUCLG1
leucine catabolic process	2	0.0016	AUH,MCCC1
organic substance metabolic process	28	0.0016	ACO2,AUH,FAM120B,FASTKD2,FECH,HADHA,LRPPRC,MCCC1,MRPL19,MRPS25,MRPS27,MRPS35,MRPS9,NCOA6,NDUFS1,NDUFS4,PEX13,PNPT1,PTCD3,SATB1,SDHC,SPG7,SUCLG1,TFAP2A,TSFM,TYW1,XPNPEP3,ZNF318
leucine metabolic process	2	0.0026	AUH,MCCC1
cellular nitrogen compound metabolic process	20	0.0026	FAM120B,FECH,LRPPRC,MCCC1,MRPL19,MRPS25,MRPS27,MRPS35,MRPS9,NCOA6,NDUFS1,NDUFS4,PNPT1,PTCD3,SATB1,SDHC,TFAP2A,TSFM,TYW1,ZNF318

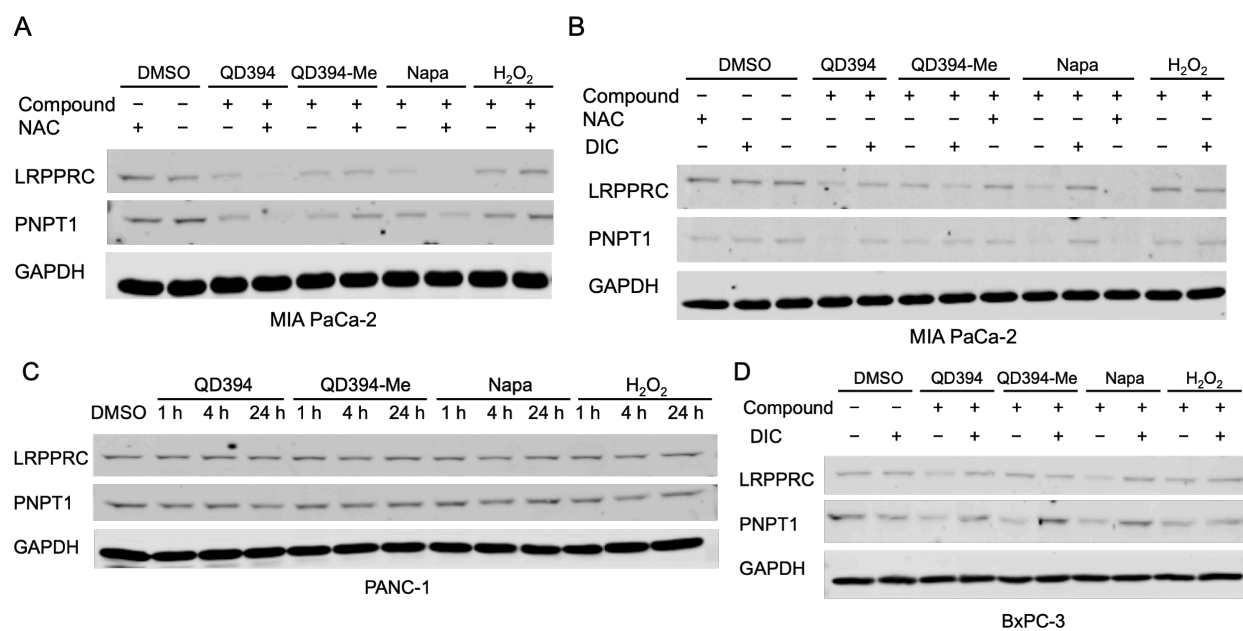


Figure III-S5. Combination of NAC, dicoumarol (DIC) with QD394, QD394-Me, napabucasin (napa) and H₂O₂ in probing LRPPRC and PNPT1 in pancreatic cancer cells. QD394, QD394-Me and napabucasin were tested at 3 × IC₅₀ for 4 h. H₂O₂ was tested at 200 μM. NAC (3 mM) and DIC (20 μM) were added 1 h before compound treatments. (A, B) MIA PaCa-2. (C) PANC-1. (D) BxPC-3.

QD394 is synergistic with napabucasin and select FDA-approved drugs

ROS inducers sensitize cancer cells to standard-of-care chemotherapy and radiation ¹⁴. QD394 and napabucasin showed synergism in the colony formation assay in both MIA PaCa-2 and PANC-1 cells (Figure III-5A, S6), suggesting the potential development of combination studies between redox modulator QD394 and cancer stemness inhibitors such as napabucasin. We next tested whether QD394 would act in synergy with the ROS inducer arsenic trioxide (As_2O_3), which is approved to treat acute promyelocytic leukemia (APL). As_2O_3 have been shown to reduce protein expression of Bcl-2, increase cellular ROS, induce permeability transition pore complex (PTPC) opening, and impair cell proliferation and apoptosis ¹⁵. QD394 sensitized cells to As_2O_3 , implying the synergistic effects between QD394 and different redox modulators (Figure III-5B). Since QD394 caused DNA damage, we assessed the synergy between QD394 and compounds regulating DNA repair. Olaparib, a poly(ADP-ribose) polymerase (PARP) inhibitor, is an FDA-approved drug to treat breast, ovarian, and pancreatic cancer ¹⁶. Combination of QD394 and olaparib resulted in synergistic effects in the colony formation assay (Figure III-5C). Cumulatively, QD394 is synergistic with cancer stemness inhibitors, other redox modulators, and PARP inhibitors.

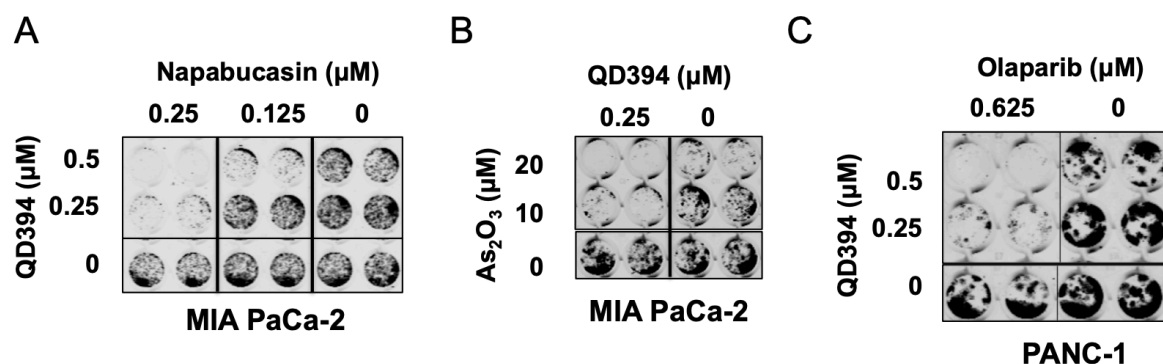


Figure III-5. QD394 is synergistic with select FDA-approved drugs in pancreatic cancer cells. Napabucasin (A), As_2O_3 (B), and Olaparib (C) were added 1 h before QD394. Cells were treated with compounds for 24 h.

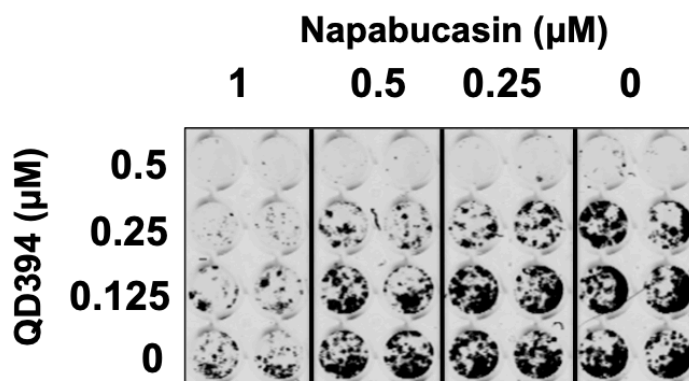


Figure III-S6. Combination of QD394 and napabucasin in PANC-1 cells.

QD394-Me shows improved plasma stability and reduced toxicity compared to QD394 in mice

We determined the stability of QD394 in mouse liver microsomes and plasma. The half-life of QD394 is over 60 minutes in mouse liver microsomes, yet only six minutes in mouse plasma, indicating it has good microsomal stability but poor metabolic stability in plasma (Table III-5). We then determined its potential metabolites in mouse plasma to better guide the design of more metabolically stable derivatives (Figure III-6A). M1 and M2 metabolites have hydroxyl groups on the rings, and M3 and M4 metabolites are produced through a Michael addition. We then synthesized QD394-Me with a methyl group to block Michael addition (Figure III-6B).

This improved the plasma stability of QD394 from six minutes to over two hours. Next, we estimated the PK characteristics of QD394 and QD394-Me in CD-1 mice following intraperitoneal injection (IP, 10 mg/kg), oral administration (PO, 20 mg/kg), or intravenous (IV, 10 mg/kg) injection. Plasma concentration of both QD394 and QD394-Me rapidly decreased within the first two hours (Figure III-S7). Notably, two out of three mice administered with QD394 *via* IV injection died likely due to systemic toxicity, while all three mice that received IV injections of QD394-Me survived throughout the study (Table III-5). Therefore, QD394-Me appears to be less toxic and more tolerable in mice compared to QD394.

To understand why the concentration of QD394-Me rapidly decreased in the plasma, we assessed tissue distribution of QD394-Me administered *via* IV and PO in mice. After one-hour treatment, colon had the highest concentration of QD394-Me, although this was relatively low compared to the dosage (Colon: around 0.3 mg/kg, PO: 20 mg/kg, IV: 10 mg/kg) (Table III-S2). Besides distribution to organs, we identified potential metabolites of QD394-Me. The major metabolite of QD394-Me contains two hydroxyl groups on the right benzene or piperazine ring (Figure III-S8). As early as 15 min, we observed the major metabolite in the plasma; however, both the parent and metabolite compounds were distributed and excreted quickly over time (Figure III-S8).

In terms of tissue distribution results and similar cytotoxicity of QD394 in HCT116 colon cancer cell lines ($IC_{50} = 0.7 \mu\text{M}$), we conducted a preliminary animal study in immunocompetent Balb/c mice using mouse colon cancer cell line CT-26. Three out of five mice displayed tumor shrinkage in the QD394-Me IV (10 mg/kg) and QD394 IP (20 mg/kg) treatment groups; however, we did not observe significant differences in the tumor sizes between control and treatment groups due to high variance (Figure III-S9). A more robust evaluation of their

efficacy in pancreatic cancer mouse models and potential combination studies with FDA-approved drugs could be further explored.

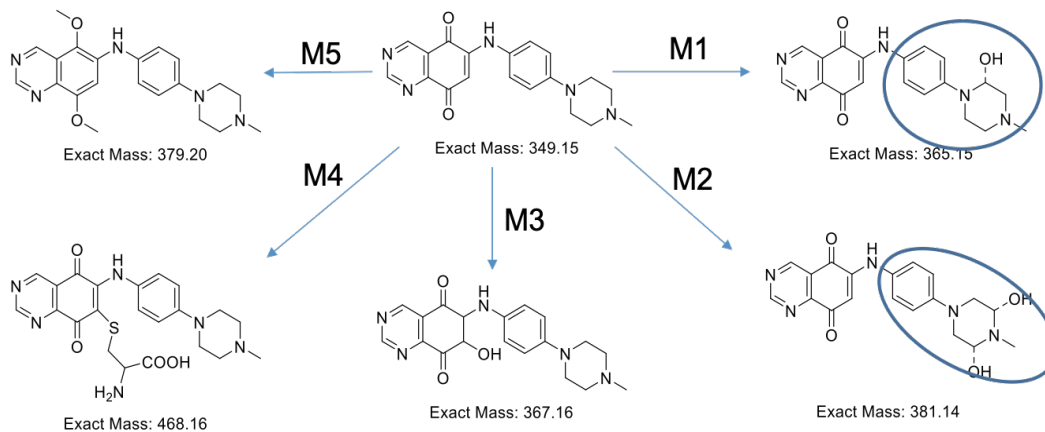
Table III-5. PK optimization of QD394. Microsomal stability, plasma stability, and PK studies were performed to evaluate the PK profiles of QD394 and its analog QD394-Me. Key parameters for each experiment are listed.

Compound	Microsomal stability T _{1/2} (min) mouse	Plasma stability T _{1/2} (min)		Concentration at 7 h in mouse plasma (ng/mL)		
		mouse	human	IP (n=2)	PO (n=2)	IV (n=3)
QD394	> 60	6	NA	5.0, 4.5	23.3, 25.8	2 out of 3 mice died
QD394-Me	44.6	> 120	> 120	6.7, 1.1	4.2, 3.4	3.4 ± 1.2

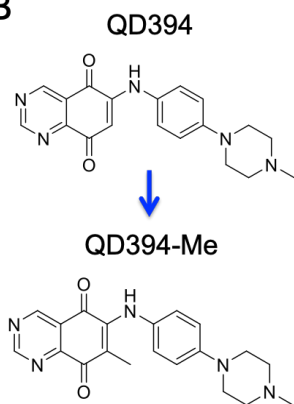
Table III-S1. Tissue distribution of QD394-Me in mouse. IV 10 mg/kg, PO 20 mg/kg, 1 h.

1h	Concentrations (ng/mL or ng/g)	
	PO 20mg/kg	IV 10mg/kg
Plasma	52	25.8
Blood	209	86.4
Skin	33.1	20.45
Bone	13.7	36.5
Lung	22.6	35.9
Pancreas	28.4	55
Spleen	40	249.5
Kidney	126.5	142.5
Colon	339	277.5
Liver	51	31.15

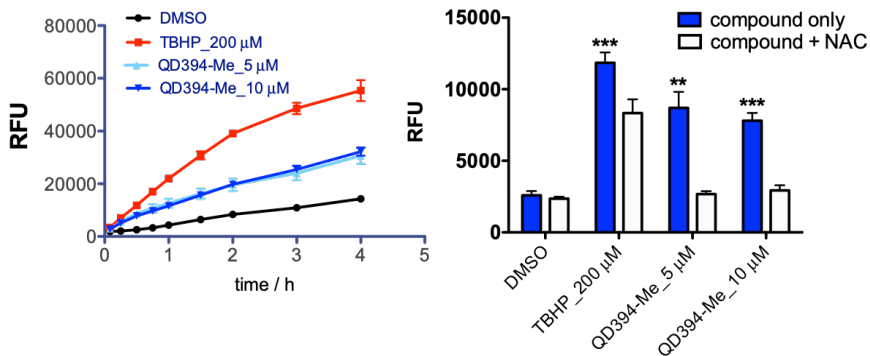
A



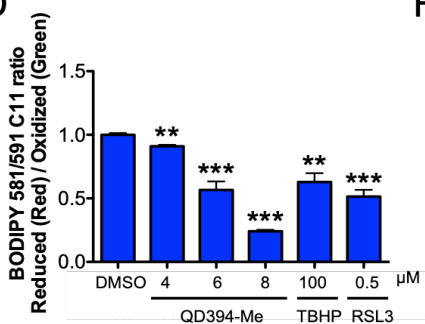
B



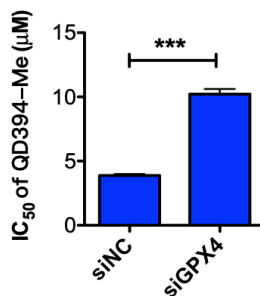
C



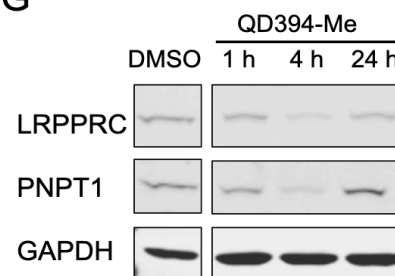
D



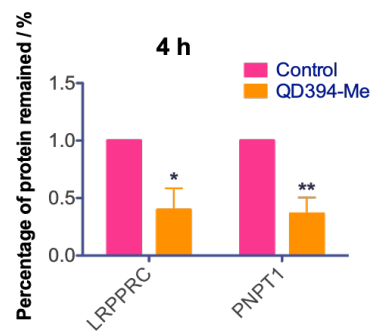
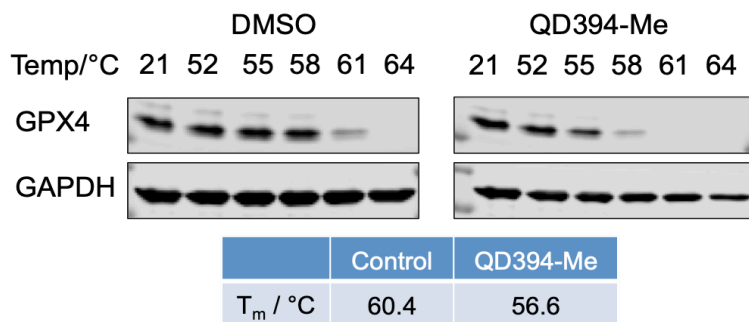
F



G



E



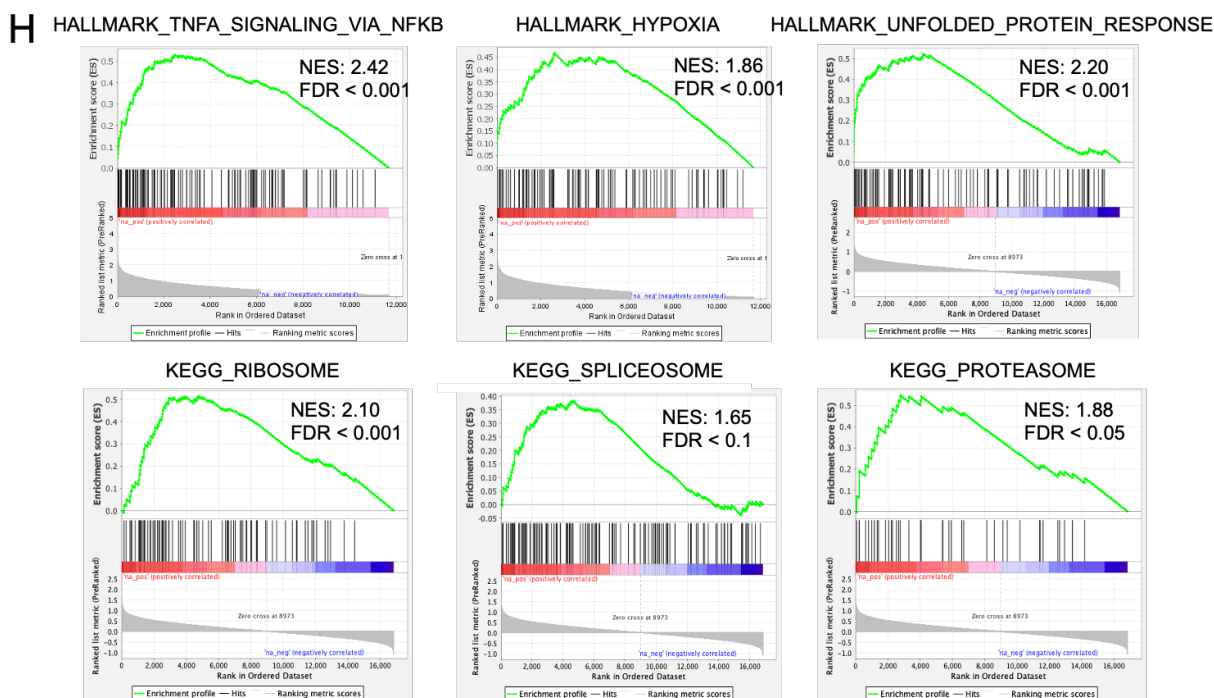


Figure III-6. Pharmacokinetics optimization of QD394 leads to QD394-Me with better stability in mouse plasma, and QD394-Me has a similar cellular profile as QD394. (A) Potential metabolites of QD394 in mouse plasma. The hydroxyl groups could be on either ring in the circle. (B) Structures of QD394 and QD394-Me. (C) QD394-Me increased cellular ROS level, and NAC reduced the induction of ROS at 30 min. ** denotes $p < 0.005$, *** denotes $p < 0.0005$. (D) QD394-Me significantly increased lipid peroxidation in MIA PaCa-2 cells. (E) QD394-Me destabilized GPX4 protein in MIA PaCa-2 cells. QD394-Me was tested at 100 μM . (F) The cytotoxicity of QD394-Me was significantly reduced in the GPX4-knockdown MIA PaCa-2 cells. siNC: samples treated with scramble siRNA; siGPX4: samples treated with GPX4 siRNA. (G) QD394-Me reduced the protein expression of LRPPRC and PNPT1 significantly at 4 h in MIA PaCa-2 cells. QD394-Me was tested at $3 \times \text{IC}_{50}$ for 1 h and 4 h, and $2 \times \text{IC}_{50}$ for 24 h. * denotes $p < 0.05$, ** denotes $p < 0.005$. (H) Select enriched gene sets of QD394-Me in MIA PaCa-2 Bru-seq samples.

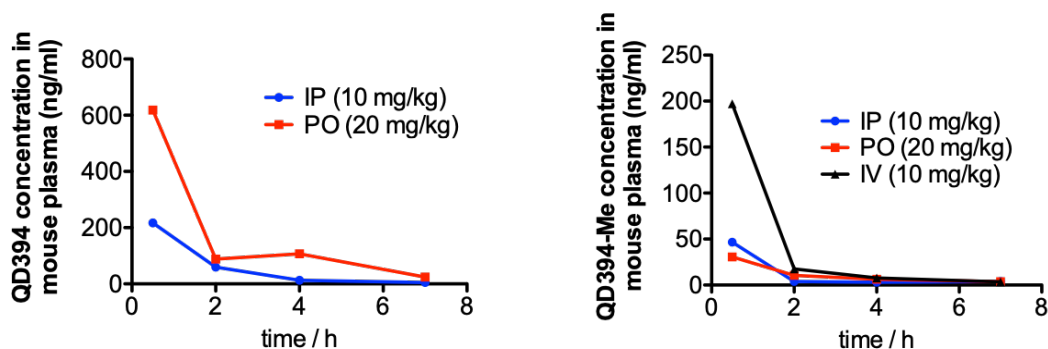


Figure III-S7. Plasma concentration of QD394 and QD394-Me administered *via* IP, PO, or IV in CD-1 mice.

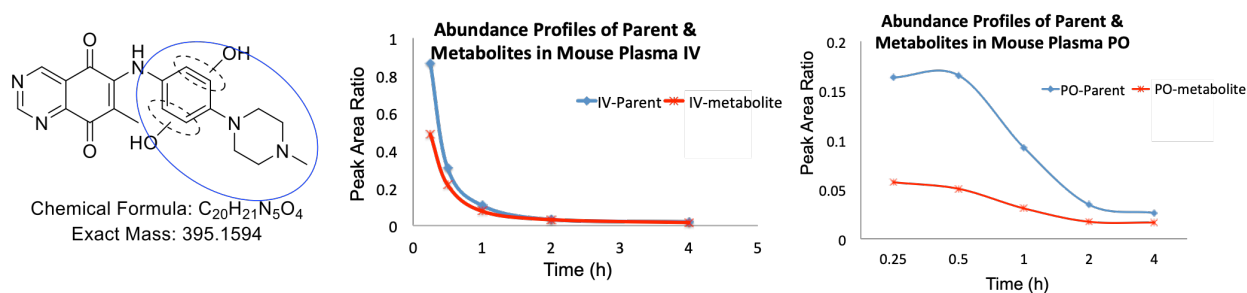


Figure III-S8. Major metabolite of QD394-Me in mouse plasma and its abundance profiles administered *via* IV or PO in mice. Two hydroxyl groups could be on either ring within the circle.

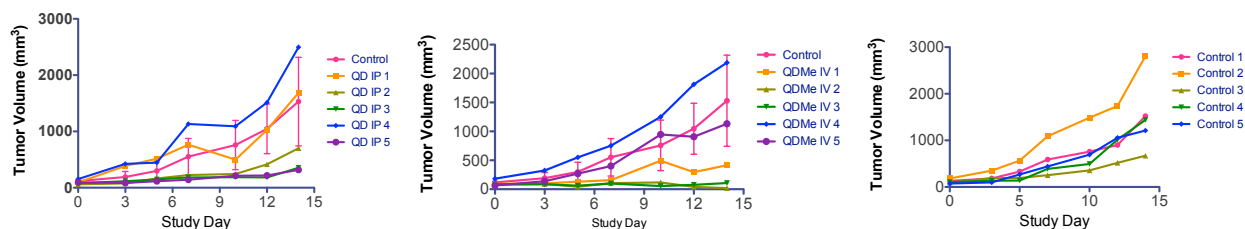


Figure III-S9. *In vivo* study with female Balb/c mice implanted subcutaneously with CT-26 cells. QD394 (QD) was dosed at 10 mg/kg IP, and QD394-Me (QDMe) was dosed 3 times weekly at 20 mg/kg IV. Five mice were in each group.

QD394-Me and QD394 share similar cell death mechanisms

QD394-Me and QD394 show similar cytotoxicity in PANC-1 and BxPC-3 cells, while QD394-Me is less potent than QD394 in MIA PaCa-2 cells (Table III-1). QD394-Me also significantly increased cellular ROS in MIA PaCa-2 cells, and NAC blocked the induction of ROS (Figure III-6C). Similar to QD394, QD394-Me increased lipid ROS significantly in a dose-dependent manner (Figure III-6D). QD394-Me destabilized GPX4 protein in pancreatic cancer cells in the CETSA experiments (Figure III-6E, S4), and its cytotoxicity was significantly reduced in the GPX4-knockdown experiments (Figure III-6F, Table III-S2). Moreover, QD394-Me significantly decreased protein expression of LRPPRC and PNPT1 at 4 h, consistent with QD394 in MIA PaCa-2 cells (Figure III-6G). Therefore, QD394-Me shows a similar mechanism

of action to QD394 in pancreatic cancer cells but has improved plasma stability and less *in vivo* toxicity.

Bru-seq analysis of QD394-Me

We tested QD394-Me in MIA PaCa-2 using Bru-seq experiments. QD394-Me induced hallmark gene sets related to TNF signaling and hypoxia, which is similar to QD394. Additionally, QD394-Me increased upfolded protein response, suggesting potential ER stress (Figure III-6H). QD394-Me also induced ROS pathway and JAK/STAT3 signaling hallmark gene sets, supporting its ROS-inducing capability and STAT3-targeting effects. KEGG pathways related to proteasome, ribosome and spliceosome were enriched by QD394-Me, indicating its downstream effects on protein and transcript regulation (Figure III-6H). There are no common downregulated enriched gene sets between QD394 and QD394-Me Bru-seq samples, and this could be because that QD394-Me only significantly stimulated very few decreased gene sets at $3\times IC_{50}$ concentration in MIA PaCa-2.

Table III-S2. Cytotoxicity of QD394, QD394-Me, and napabucasin in GPX4-knockdown PANC-1 and BxPC-3 cells. siNC: samples treated with scramble siRNA; siGPX4: samples treated with GPX4 siRNA.

IC ₅₀ (μM)	PANC-1		BxPC-3	
	siNC	siGPX4	siNC	siGPX4
QD394	0.362	1.064	0.715	1.292
QD394-Me	2.734	6.74	3.55	4.649
Napa	1.159	3.143	1.041	1.72

Discussion

ROS induction alters the activity of multiple transcription factors, including STAT3, NF-κB, and hypoxia-inducible factor-1α (HIF-1A) ¹⁷. STAT3 signaling is downstream of MAPK,

JAK, and Src pathways. Redox modulation can inactivate these kinases leading to either activation or inhibition of STAT3 signaling, depending on cellular context and duration of ROS generation¹⁸. TNFA signaling and hypoxia hallmark gene sets were upregulated by QD394 and napabucasin. TNFA/TNF are important cytokines for maintaining cellular homeostasis and mediating the activation of NF- κ B, which in turn regulates downstream prosurvival genes, MAPK signaling, and cell death in cancers and inflammatory diseases^{19,20}. The transcription factor HIF-1A is activated by hypoxic conditions and responds to accumulated ROS *via* NF- κ B activation^{21,22}. ROS induction by QD394 and napabucasin can trigger these signaling pathways. Napabucasin is a cancer stemness inhibitor that reduces the proliferation, invasion, and stemness of cancer cells^{23,24}. Napabucasin is bioactivated by NQO1 and generates ROS to induce DNA damage and cell death²⁵. In this study, we report that necrostatin-1 rescued napabucasin-mediated cell death, suggesting that napabucasin induces necroptotic cell death in pancreatic cancer cells. However, QD394 did not cause necroptosis, but iron-, ROS-dependent, and GPX4-mediated ferroptosis (Figure III-7)^{26,27}.

Liproxstatin-1 inhibits ferroptosis induced by erastin, BSO and RSL3 *in vitro*, and it prevents ferroptosis and ROS accumulation in GPX4 knockout cells both *in vitro* and *in vivo*^{28,29}. Ferrostatin-1 is a first-generation ferroptosis inhibitor that rescues cell death caused by erastin and RSL3^{1,30}. Additionally, both compounds are effective radical-trapping antioxidants in the lipid bilayers³⁰. However, ferrostatin-1 did not prevent H₂O₂-induced necrosis, although ferroptosis is defined as a necrotic-like cell death¹. The fact that QD394 induces ROS may explain why ferrostatin-1 did not rescue QD394-induced cell death. Although ferrostatin-1 blocked lipid peroxidation and ferroptosis, QD394 could cause ROS-involved DNA damage and necrotic cell death (Figure III-7). Therefore, we suggest that a combination of cell death

pathways are induced by QD394 and QD394-Me, but ferroptosis is an essential part since GPX4 protein expression regulates the cytotoxicity of QD394 and QD394-Me. Interestingly, we determined potential interactions between QD394, QD394-Me, and GPX4 in the cells, but the detailed binding site requires further investigation.

LRPPRC and PNPT1 are closely related to mitochondrial translation and RNA catabolic processes in different diseases³¹⁻³⁴. LRPPRC deficiency alters mitochondrial electron transport chain, mitochondrial permeability, and transmembrane ROS diffusion³⁵. PNPT1 regulates the correct maturation of mitochondrial ND6 transcripts and efficient mitochondrial RNA degradation^{33,34}. Both proteins are involved in mitochondrial function and negatively associated with the survival of pancreatic adenocarcinoma patients. Our redox modulators, QD394 and QD394-Me, decreased the expression of these two proteins, which thus could be used as potential pharmacodynamic biomarkers in pancreatic cancer (Figure III-7). Meanwhile, further understanding of the connection between overexpression of these two genes and pancreatic cancer is needed and may lead to novel therapeutics.

Conclusions

In this study, we developed a novel redox modulator QD394 and explored its mechanisms of action in pancreatic cancer cells. QD394 shares a highly similar transcriptomic profile to napabucasin, inhibits STAT3 phosphorylation, increases ROS levels, and induces DNA damage. However, while napabucasin causes necroptosis, QD394 induces an iron-, ROS-dependent, and GPX4-mediated cell death. One essential cell death mechanism of QD394 is ferroptosis, since QD394 increases lipid peroxidation, destabilizes GPX4 protein, and its cytotoxicity is dependent on GPX4. Bru-seq and proteomics analysis reveal that QD394 decreases both nascent transcripts and protein expression of LRPPRC and PNPT1. Furthermore,

QD394 acts in synergy with several FDA-approved drugs, suggesting its potential utility to overcome drug resistance. A PK-guided optimization campaign resulted in QD394-Me with improved mouse plasma stability and less systemic toxicity in mice.

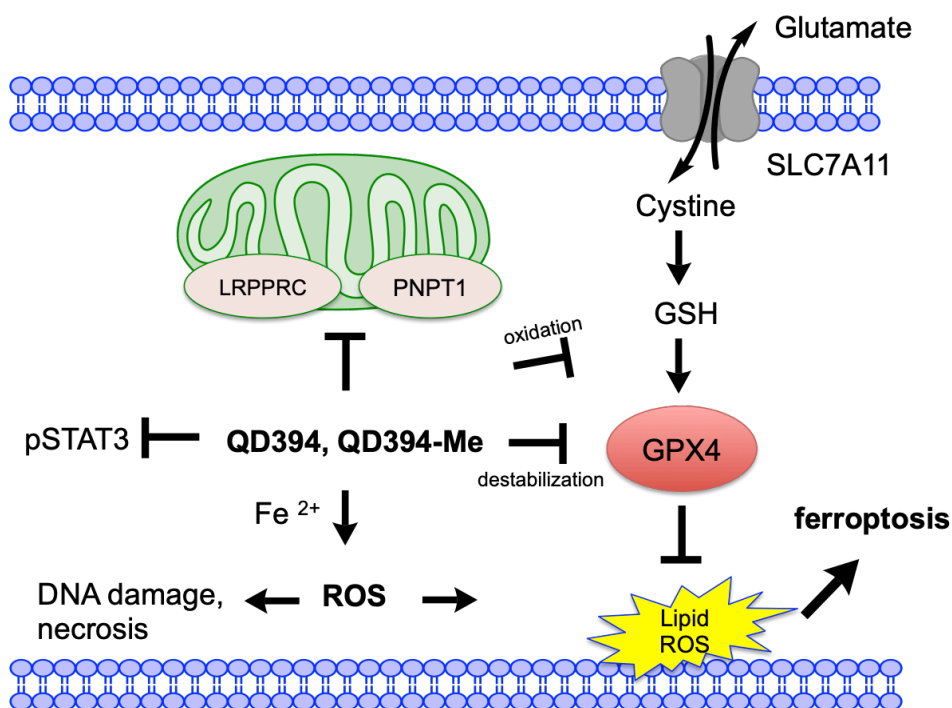


Figure III-7. Summarized working mechanisms of QD394 and QD394-Me in pancreatic cancer cells. QD394 and QD394-Me increase cellular ROS level, induce DNA damage, decrease mitochondrial proteins, and promote accumulation of lipid ROS. They oxidize GSH to GSSG and destabilize GPX4 in the cells. Their cytotoxicity is dependent on iron, ROS, and GPX4 expression. Ferroptosis and necrosis are potentially involved in their cell death mechanisms.

Methods

Chemical compounds. Stock solutions of QD compounds and napabucasin were made in dimethylsulfoxide (DMSO) at 10 mM and were stored at -20 °C. QD compounds were synthesized in Dr. Mario Sechi's Lab at the University of Sassari. Napabucasin was purchased from Medchem Express. N-acetyl cysteine (Sigma) and deferoxamine mesylate salt (Sigma) were dissolved in ultrapure water (Gibco). Z-VAD (MedChemExpress), necrostatin-1

(Selleckchem), RSL3 (Cayman Chemical), deferasirox (Cayman Chemical), liproxstatin-1 (Cayman Chemical), ferrostatin-1 (Cayman Chemical), chloroquine phosphate (LKT LABS), olaparib (MedChemExpress), 3-Methyladenine (Cayman Chemical), and N-phenylmaleimide (Oakwood Chemical) were dissolved in DMSO.

Cell lines and cell culture. Pancreatic cancer cell lines (MIA PaCa-2, PANC-1, and BxPC-3) were purchased from ATCC. All cell lines were maintained in RPMI 1640 (Gibco) containing 10% FBS (Gibco) at 37 °C in a humidified atmosphere of 5% CO₂. All cell lines were in culture under 35 passages and determined to be free of mycoplasma contamination using Plasmoguard Test (InvivoGen, San Diego, CA).

MTT assay. Cytotoxicity was determined by a 3-(4,5-dimethylthiazol-2-yl)-2,5-diphenyltetrazolium bromide (MTT) assay. Cells were seeded in 96-well tissue culture plates and allowed overnight attachment. Subsequently, cells were treated with compounds or DMSO for 72 h. MTT solution (0.3 mg/mL) was added to each well for 3 h in the incubator. After removal of the media, DMSO was added, and the plates were shaken for 15 min before measuring the absorbance at a wavelength of 570 nm using a microplate reader (Molecular Devices). IC₅₀ values were calculated using GraphPad Prism.

Colony Formation Assay. Cells were seeded in 96-well tissue culture plates at 300 cells (MIA PaCa-2) or 600 cells (PANC-1 and BxPC-3) per well. After overnight attachment, cells were treated with compounds continuously. Cell death inhibitors or signaling pathway inhibitors were added 1 h prior to compound treatment. Plates were incubated for 7-9 days until cells in the control wells became 80-90% confluent. Media was removed, and cells were stained with a 0.05% crystal violet solution for 30 min. Cells were then washed with ddH₂O to remove excess stain,

and the plates were imaged using Odyssey Imaging Systems (LI-COR Biosciences) after overnight drying.

ROS measurement. Cells were seeded in 96-well flat clear-bottom black tissue-culture plates (Corning #3603) at a density of 1.8×10^4 cells per well. After overnight attachment, cells were stained with CM-H2DCFDA dye (10 μ M, Thermo Fisher, C6827) in HBSS for 40 min at 37 °C. Cells were washed with pre-warmed DPBS (Gibco) twice, and 80 μ L HBSS was added. Compounds were added in HBSS at designated concentrations. Fluorescent signal was measured using a CLARIO Star plate reader (Ex: 483-15 nm; Em: 530-20 nm; BMG LABTECH).

GSH/GSSG-Glo assay. GSH/GSSG-Glo assay kit (Promega) was used to determine the GSH/GSSG ratio in cells with drugs or DMSO. 15,000 - 20,000 cells per well were seeded into solid opaque 96-well tissue culture plates (Falcon). After overnight attachment and compound treatment, medium was removed, and cells were lysed with 50 μ L of Total or Oxidized Glutathione Reagent per well. The plate was shaken for 5 minutes, and 50 μ L fresh Luciferin Generation Reagent was added to each well. After 30-min incubation at room temperature, 100 μ L Luciferin Detection Reagent was added. Luminescence was detected using a CLARIOstar plate reader (BMG LABTECH) after 15-min equilibration. GSH/GSSG ratio was calculated with net RLU, using the formula: (net vehicle total glutathione RLU – net vehicle GSSG RLU)/(net vehicle GSSG RLU/2).

Bru-seq experiments and analysis. Nascent RNA Bru-seq experiments were performed as previously reported ⁶. Briefly, 2×10^6 cells were seeded in 10 cm dishes in duplicates. After overnight attachment, cells were treated with compounds ($3 \times IC_{50}$) for 4 h. Cells were added with bromouridine at a final concentration of 2 mM and incubated at 37 °C for the last 30 min of the drug treatments. Cells were then collected and lysed in TRIzol, and total RNA was isolated.

The bromouridine-containing RNAs were captured using anti-BrdU antibodies conjugated to magnetic beads and converted to cDNA libraries (Illumina TrueSeq), which were sent for deep sequencing at the University of Michigan Sequencing Core. Sequencing reads were mapped to the hg38 reference genome, and DESeq2 was used to determine differentially expressed genes. The shrunkenLFC (shrunken log₂FoldChange) was calculated from DESeq2. We used shrunkenLFC for the heatmap and GSEA analysis. Downstream signaling pathways were identified using GSEA. Heatmaps and statistics were generated using the R programming language.

Immunoblot. Cells were seeded in 6-well tissue culture plates at 3.5×10^5 cells per well. After compound treatments, cells were washed with DPBS (Gibco) and lysed with RIPA buffer containing 1× protease inhibitor (Sigma) and 1× phosphatase inhibitor (Sigma). Cell lysates were sonicated before centrifugation at 14,000 rpm for 10 min at 4 °C, and supernatant was collected for BCA protein assay (Thermo Scientific). 25 µg proteins from each sample was resolved on 10% SDS polyacrylamide gels and electrotransferred to PVDF membranes (Trans-Blot® Turbo™ RTA Mini PVDF Transfer Kit, BIO-RAD). After blocking with 5% milk in 1× TBS for 1 h at room temperature, membranes were probed with primary antibodies (1:500-1:1000) in 5% milk in 1× TBST or 5% BSA in 1× TBST overnight at 4 °C. The membranes were then washed with TBST three times, and probed with anti-rabbit or anti-mouse secondary antibody (Dylight 800 4 × PEG conjugated; Thermo Scientific; 1:6000) for 1 h at room temperature. Membranes were imaged with Odyssey Imaging Systems (LI-COR Biosciences). Protein expression was quantified with ImageJ and normalized to loading controls.

Lipid ROS measurement. MIA PaCa-2 cells were treated with compounds for the designated time before 10 µM C11-BODIPY (Thermo Fisher) was added, and cells were incubated for 30

min at 37 °C. Cells were washed with DPBS (Gibco) twice, and 100 µL HBSS was added before measurement using a CLARIOstar plate reader (BMG LABTECH). Plates were read with two filter sets; one at excitation/emission of 581/591 nm (Texas Red) for the reduced dye, and the other at excitation/emission of 488/510 nm (FITC) for the oxidized dye. The ratio of the emission fluorescence intensities at the Texas Red filter and FITC filter was calculated in Microsoft Excel, and *p* value was determined using unpaired Student's *t*-test.

Cellular Thermal Shift Assay (CETSA). Cells were seeded at 3×10^6 cells per 10 cm cell culture dish. After overnight attachment, 100 µM QD394, QD394-Me, or DMSO was added to the cells for 1 h. Cells were then trypsinized, washed with DPBS, and suspended in 650 µL DPBS. The suspensions were split into 100 µL aliquots, heated at indicated temperatures for 3 minutes in the Veriti Thermal Cycler (Applied Biosystems), and incubated for 3 minutes at room temperature. Each aliquot was flash-frozen three times and spun at 12,000 rpm for 20 minutes at 4 °C. Supernatants were collected, and 25 µL of each sample was loaded onto a 10% SDS polyacrylamide gel for immunoblot analysis using the protocol detailed above.

siRNA knockdown of GPX4. GPX4 siRNA (s6110) and negative control siRNA (4390843) were purchased from Thermo Fisher. According to the manufacturer's instructions, 3.5×10^5 cells were seeded in 6-well tissue culture plates for overnight attachment. The siRNA transfection reagent complex was formed by combining 30 pmol siRNA in 150 µL Opti-MEM medium (Thermo Fisher) with 9 µL Lipofectamine RNAiMAX Reagent (Thermo Fisher) in 150 µL Opti-MEM medium. After 15-min incubation, this complex was added to each well with fresh medium for 48 h. One half of these cells were harvested for immunoblot, and the other half were seeded for the 24 h MTT assay to determine the cytotoxicity of QD394, QD394-Me, and napabucasin.

Proteomics study. MIA PaCa-2 cells were treated with 1.2 μ M QD394 or DMSO control for 24 h before collecting the cell lysates in RIPA buffer. 75 μ g proteins of each sample was sent to the Proteomics Core at the University of Michigan in duplicate. TMT10plex Mass Tag Labeling Kit (ThermoFisher) was used to quantify the proteins in each sample, and Abundance Ratio and log₂ Abundance Ratio were calculated as treatment over control. STRING analysis was performed using proteins with adjusted *p* values below 0.05.

Survival analysis of LRPPRC and PNPT1. Patient sample RNASeq RSEM normalized gene expression values and related survival metadata were sourced from the TCGA GDAC Firehose³⁶. When multiple samples were available for a given patient, barcodes were sorted alphabetically and the first was selected for analysis. TCGA disease patient samples were evaluated for reduced survivability by comparing survival outcomes for patients with high and low expression of LRPPRC and PNPT1. Thresholding for high and low expression patient populations was evaluated using five different quantile cutoffs: 95%, 90%, 75%, 50%, and 25%. A log-rank test statistic was calculated for each cutoff to compare the survival distributions of high and low expression patient populations with the null hypothesis that there was no difference in survival curves. Survival analysis was performed using the R statistical programming language.

Microsomal stability test. The 10 mM stock solutions of QD394, QD394-Me, and verapamil (positive control) were prepared in DMSO. Solutions were diluted to 1 mM with acetonitrile and further diluted to 10 μ M with 0.1 M phosphate buffer (3.3 mM MgCl₂). NADPH (1 mg) was dissolved in 60 μ L 0.1 M phosphate buffer (3.3 mM MgCl₂). 330 μ L 0.1 M phosphate buffer (3.3 mM MgCl₂) and 40 μ L 10 μ M test compounds were added to 10 μ L microsomes (20 mg/mL). Data points were collected at 0, 5, 10, 15, 30, 45, and 60 min. Solutions were

centrifuged at 3500 g for 10 min to pellet precipitated proteins. The supernatant was used for LC/MS/MS analysis. Natural log peak area ratio (compound peak area / internal standard peak area) was plotted against time, and the gradient of the line was determined to calculate the half-life ($t_{1/2}$) of the test compound in microsomes.

Plasma stability test. Pooled mouse plasma was stored at -80 °C prior to use. Compounds were dissolved in DMSO to obtain a concentration of 500 μ M. 1 μ L compound was added to 500 μ L plasma. Samples were collected at time points of 0, 0.17, 0.5, 1, 2, and 4 h. The solution was centrifuged at 3500 g for 10 min to pellet precipitated proteins. The supernatant was used for LC-MS/MS analysis. Natural log peak area ratio (compound peak area / internal standard peak area) was plotted against time, and the gradient of the line was determined to calculate the half-life ($t_{1/2}$) of the test compound in plasma.

PK study. QD394 and QD394-Me were administered by IP injection (10 mg/kg), oral PO (20 mg/kg), or IV injection (10 mg/kg) to CD-1 mice. At the given time points (0.5, 2, 4, and 7 h), blood samples were collected using heparinized calibrated pipettes. Samples were centrifuged at 15,000 rpm for 10 min. Subsequently, blood plasma was collected from the upper layer. The plasma was frozen at -80 °C for LC-MS/MS analysis.

Metabolite identification. QD394 and QD394-Me were incubated with mouse plasma under the same conditions as the plasma stability test. Samples were collected at 0.5 h to determine potential metabolites of QD394 or QD394-Me using LC-MS/MS analysis. Indicated metabolites were also measured *in vivo* after 1-hour QD394-Me treatment.

Tissue distribution analysis. Mice were dosed with QD394 at 20 mg/kg PO and QD394-Me at 10 mg/kg IV. After 1 h, indicated organs were collected for later analysis. Dissociation solvent was added at five-fold the tissue weight into each homogenization tube with beads for tissue

homogenization, and 30 μL homogenate was isolated for sample preparation. For calibration curve samples, 30 μL blank homogenate was mixed with 30 μL standard solution and 140 μL internal standard solution; for dosed samples, 30 μL homogenate was mixed with 30 μL blank acetonitrile and 140 μL internal standard solution. Samples were vortexed and centrifuged at 3500 g for 10 min, and the supernatant was isolated for LC-MS analysis.

Mice study. Female Balb/c mice were purchased from Envigo. At the time of implantation, all mice were aged 5-6 weeks. Mice were implanted subcutaneously in the right flank with 1×10^6 CT-26 cells in 100 μL DPBS. Seven days after implantation, mice were randomized into groups ($n = 5$) with mean tumor volumes ranging from 97 to 117 mm^3 . The negative control group was dosed daily in the intraperitoneal cavity (IP) with the same vehicle used for QD394. QD394 was dosed at 10 mg/kg IP, and QD394-Me was dosed 3 times weekly intravenously (IV) at 20 mg/kg. After 17 days of dosing, four hours post-dose, negative control and treated groups were euthanized by CO_2 asphyxiation followed by cervical dislocation. The end of the study was chosen as the first day that any mouse reached humane euthanasia criteria determined by the animal use protocol.

Statistical analysis. For the Bru-seq analysis, Pearson correlation and p value were calculated using function `cor.test()` in R (version 3.3.2). Significance levels for assays and immunoblots were calculated using unpaired Student's t -test in Microsoft Excel. Results were shown as mean \pm standard deviation from at least three independent experiments.

Author contributions

Shuai Hu is the primary author. Mario Sechi's lab synthesized the QD analogs. Mats Ljungman's lab performed the Bru-seq experiments. Duxin Sun's lab assisted the PK studies.

Sean McCann conducted the animal studies. Armand Bankhead III made Figure II-4C. Nouri Neamati is the corresponding author.

References

1. Dixon, S. J. *et al.* Ferroptosis: an iron-dependent form of nonapoptotic cell death. *Cell* 149, 1060–1072 (2012).
2. Stockwell, B. R. *et al.* Ferroptosis: A Regulated Cell Death Nexus Linking Metabolism, Redox Biology, and Disease. *Cell* 171, 273–285 (2017).
3. Galluzzi, L. *et al.* Molecular mechanisms of cell death: recommendations of the Nomenclature Committee on Cell Death 2018. *Cell Death Differ.* 25, 486–541 (2018).
4. Mou, Y. *et al.* Ferroptosis, a new form of cell death: opportunities and challenges in cancer. *J. Hematol. Oncol.* 12, 34 (2019).
5. Ye, L. F. *et al.* Radiation-Induced Lipid Peroxidation Triggers Ferroptosis and Synergizes with Ferroptosis Inducers. *ACS Chem. Biol.* 15, 469–484 (2020).
6. Paulsen, M. T. *et al.* Use of Bru-Seq and BruChase-Seq for genome-wide assessment of the synthesis and stability of RNA. *Methods* 67, 45–54 (2014).
7. Blaser, H., Dostert, C., Mak, T. W. & Brenner, D. TNF and ROS Crosstalk in Inflammation. *Trends Cell Biol.* 26, 249–261 (2016).
8. Nishigori, C., Hattori, Y. & Toyokuni, S. Role of Reactive Oxygen Species in Skin Carcinogenesis. *Antioxidants & Redox Signaling* vol. 6 561–570 (2004).
9. Rodust, P. M., Stockfleth, E., Ulrich, C., Leverkus, M. & Eberle, J. UV-induced squamous cell carcinoma--a role for antiapoptotic signalling pathways. *Br. J. Dermatol.* 161 Suppl 3, 107–115 (2009).
10. Görlach, A. *et al.* Reactive oxygen species, nutrition, hypoxia and diseases: Problems solved? *Redox Biol* 6, 372–385 (2015).
11. Tafani, M. *et al.* The Interplay of Reactive Oxygen Species, Hypoxia, Inflammation, and Sirtuins in Cancer Initiation and Progression. *Oxid. Med. Cell. Longev.* 2016, 3907147 (2016).
12. Stockwell, B. R. Ferroptosis: Death by lipid peroxidation. *Free Radical Biology and Medicine* vol. 120 S7 (2018).
13. Szklarczyk, D. *et al.* STRING v11: protein-protein association networks with increased coverage, supporting functional discovery in genome-wide experimental datasets. *Nucleic Acids Res.* 47, D607–D613 (2019).
14. Gupta, S. C. *et al.* Upsides and downsides of reactive oxygen species for cancer: the roles of reactive oxygen species in tumorigenesis, prevention, and therapy. *Antioxid. Redox Signal.* 16, 1295–1322 (2012).

15. Carney, D. A. Arsenic trioxide mechanisms of action – looking beyond acute promyelocytic leukemia. *Leukemia & Lymphoma* vol. 49 1846–1851 (2008).
16. Olaparib. *National Cancer Institute* <https://www.cancer.gov/about-cancer/treatment/drugs/olaparib> (2014).
17. Prasad, S., Gupta, S. C. & Tyagi, A. K. Reactive oxygen species (ROS) and cancer: Role of antioxidative nutraceuticals. *Cancer Lett.* 387, 95–105 (2017).
18. Fang, B. Genetic Interactions of STAT3 and Anticancer Drug Development. *Cancers* 6, 494–525 (2014).
19. Annibaldi, A. & Meier, P. Checkpoints in TNF-Induced Cell Death: Implications in Inflammation and Cancer. *Trends Mol. Med.* 24, 49–65 (2018).
20. Shen, J. *et al.* Anti-cancer therapy with TNF α and IFN γ : A comprehensive review. *Cell Prolif.* 51, e12441 (2018).
21. Semenza, G. L. Defining the role of hypoxia-inducible factor 1 in cancer biology and therapeutics. *Oncogene* 29, 625–634 (2010).
22. Bonello, S. *et al.* Reactive Oxygen Species Activate the HIF-1 α Promoter Via a Functional NF κ B Site. *Arteriosclerosis, Thrombosis, and Vascular Biology* vol. 27 755–761 (2007).
23. Han, D. *et al.* Napabucasin, a novel STAT3 inhibitor suppresses proliferation, invasion and stemness of glioblastoma cells. *J. Exp. Clin. Cancer Res.* 38, 289 (2019).
24. Sugarman, R. *et al.* Pharmacokinetics and pharmacodynamics of new drugs for pancreatic cancer. *Expert Opin. Drug Metab. Toxicol.* 15, 541–552 (2019).
25. Froeling, F. E. M. *et al.* Bioactivation of Napabucasin Triggers Reactive Oxygen Species-Mediated Cancer Cell Death. *Clin. Cancer Res.* 25, 7162–7174 (2019).
26. Pathania, D. *et al.* Design and discovery of novel quinazolinedione-based redox modulators as therapies for pancreatic cancer. *Biochim. Biophys. Acta* 1840, 332–343 (2014).
27. Pathania, D., Kuang, Y., Sechi, M. & Neamati, N. Mechanisms underlying the cytotoxicity of a novel quinazolinedione-based redox modulator, QD232, in pancreatic cancer cells. *Br. J. Pharmacol.* 172, 50–63 (2015).
28. Friedmann Angeli, J. P. *et al.* Inactivation of the ferroptosis regulator Gpx4 triggers acute renal failure in mice. *Nat. Cell Biol.* 16, 1180–1191 (2014).
29. Xie, Y. *et al.* Ferroptosis: process and function. *Cell Death & Differentiation* vol. 23 369–379 (2016).
30. Shah, R., Margison, K. & Pratt, D. A. The Potency of Diarylamine Radical-Trapping Antioxidants as Inhibitors of Ferroptosis Underscores the Role of Autoxidation in the Mechanism of Cell Death. *ACS Chem. Biol.* 12, 2538–2545 (2017).
31. Zhou, W. *et al.* Proteasome-Independent Protein Knockdown by Small-Molecule Inhibitor for the Undruggable Lung Adenocarcinoma. *J. Am. Chem. Soc.* 141, 18492–18499 (2019).
32. Cui, J., Wang, L., Ren, X., Zhang, Y. & Zhang, H. LRPPRC: A Multifunctional Protein Involved in Energy Metabolism and Human Disease. *Front. Physiol.* 10, 595 (2019).

33. Matilainen, S. *et al.* Defective mitochondrial RNA processing due to PNPT1 variants causes Leigh syndrome. *Hum. Mol. Genet.* 26, 3352–3361 (2017).
34. Liu, X. *et al.* PNPT1 Release from Mitochondria during Apoptosis Triggers Decay of Poly(A) RNAs. *Cell* 174, 187–201.e12 (2018).
35. Cuillerier, A. *et al.* Loss of hepatic LRPPRC alters mitochondrial bioenergetics, regulation of permeability transition and trans-membrane ROS diffusion. *Human Molecular Genetics* vol. 26 3186–3201 (2017).
36. Broad GDAC Firehose. <https://gdac.broadinstitute.org/>.

CHAPTER IV

Identification and Characterization of Novel Mitochondrial Transcription Inhibitors

Mitochondria are essential cellular organelles that serve as "powerhouses" to not only generate ATP through oxidative phosphorylation (OXPHOS), but also produce reactive oxygen species (ROS), control calcium signaling, and regulate cell cycle and differentiation¹⁻³. The mitochondria of cancer cells undergo extensive bioenergetic and biosynthetic reprogramming to facilitate proliferation, invasion, and metastasis¹⁻³. Increasing studies show that targeting mitochondria is an attractive anticancer therapy⁴⁻⁷. Anticancer drug ditercalinium intercalates with the major groove of DNA and depletes mtDNA^{8,9}. An effective approach to generate small molecules targeting mitochondria is to conjugate a lipophilic cation, such as a triphenylphosphonium (TPP⁺) moiety, to the drug of interest^{10,11}. Previously, we developed a TPP-derivative of the nitrogen mustard chlorambucil (Figure IV-1), a DNA alkylating drug approved by the FDA for the treatment of chronic lymphocytic leukemia and lymphomas¹². This TPP-conjugated chlorambucil, named Mito-Chlor, selectively localizes to mitochondria, where it acts on mtDNA and causes cell cycle arrest and cell death¹².

In this study, we show that Mito-Chlor, but not its precursor compound chlorambucil inhibits the transcription of the mitochondrial genome. Comparing Bru-seq data from other novel small molecules led to the identification of a new compound SQD1 featuring a styrylquinoline-5, 8-dione core as another mitochondrial transcription inhibitor. Quinones are

widely distributed in natural products and several FDA approved drugs, such as doxorubicin, mitoxantrone, and apaziquone, have been extensively used for the treatment of multiple cancers (Figure IV-1).

This study expanded current understanding of Mito-Chlor and identified it as a potent mitochondrial transcription inhibitor. A novel compound SQD1 sharing a similar transcriptomic profile with Mito-Chlor was also discovered and characterized in parallel with Mito-Chlor to further elucidate their mechanisms of action.

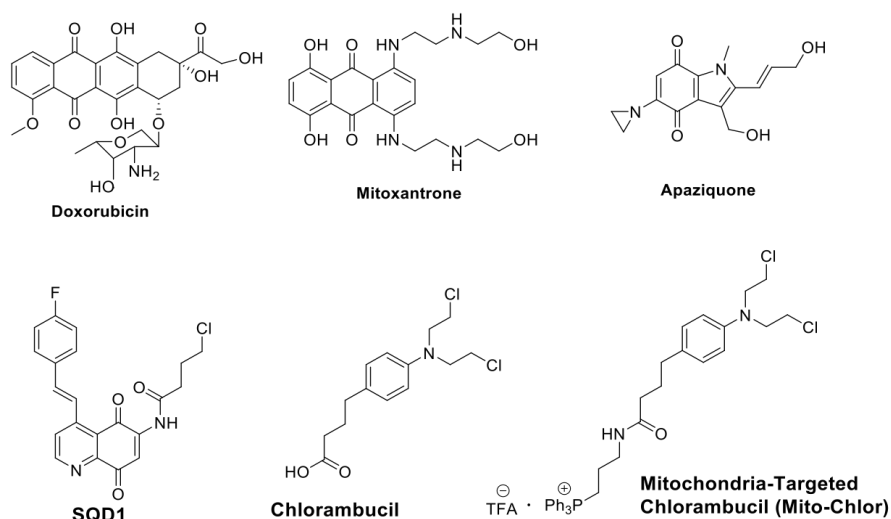


Figure IV-1. The structures of SQD1, Mito-Chlor, chlorambucil and select anticancer agents with a quinone scaffold.

Results and discussion

Mito-Chlor and SQD1 inhibit the transcription of the mitochondrial genome

The circular mitochondrial genome contains a guanine-rich heavy (H-strand) and a guanine-poor light strand (L-strand)¹⁴. H-strand and L-strand are transcribed independently, controlled by the light-strand promoter (LSP), the heavy-strand promoter 1 (HSP1) and the heavy-strand promoter 2 (HSP2), which are located nearby in the displacement loop (D-loop),

the main non-coding region of the mtDNA¹⁴. The H-strand encodes 12 mitochondrial proteins, such as ATP6 and CYB, while the L-strand only encodes ND6 (Figure IV-2A)¹⁵. These proteins constitute essential subunits of the four mitochondrial respiratory chain complexes (I–IV).

Mito-Chlor was shown to accumulate in mitochondria and act on mtDNA, setting it apart from its parent compound chlorambucil¹². In order to assess how Mito-Chlor affects mitochondrial genes, we used Bru-seq technique, a useful tool for interpreting the mechanism of action of novel agents^{13,16}. In the Bru-seq trace diagrams of mitochondrial transcripts, remarkably, after a 4-hour treatment in MIA PaCa-2 cells, Mito-Chlor inhibited transcription from the H-strand promoters, while having no detectable effect on transcription from the L-strand promoter. In contrast, chlorambucil showed no inhibitory effect on either of the two strands (Figure IV-2B). In order to identify other small molecules with similar mechanism to Mito-Chlor, we performed a robust cluster analysis using a collection of over 100 in-house compounds analyzed by Bru-seq (not shown). This analysis led to the identification of a novel compound SQD1, featuring a unique styrylquinoline-5, 8-dione core (Figure IV-1). SQD1 shares a similar genome-wide transcription profile with Mito-Chlor, and interestingly, it is also found to block the transcription from the mitochondrial genome (Figure IV-2B). Additionally, H₂O₂ inhibited mitochondrial transcription from the H-strand promoters in a dose-dependent manner (Figure IV-2B), indicating that ROS could cause mitochondrial transcription inhibition.

We next conducted real-time PCR (RT-PCR) to detect the mRNA levels of mitochondrial genes located on both strands of the circular mtDNA (Figure IV-2C). MT-ND6 (mitochondrially encoded NADH: ubiquinone oxidoreductase core subunit 6) is the only protein-coding gene on the L-strand, and MT-ATP6 (mitochondrially encoded ATP synthase membrane subunit 6) and MT-CYB (mitochondrially encoded cytochrome B) are two protein-coding genes on the H-

strand. Similar to the Bru-seq results, SQD1 significantly decreased the transcription of ATP6, CYB and ND6 genes, confirming that SQD1 inhibited mitochondrial transcription from all promoters (Figure IV-2B). Mito-Chlor reduced the steady-state level of ND6 transcripts expressed from the LSP promoter, which was not observed in the nascent RNA Bru-seq. Furthermore, Mito-Chlor decreased CYB transcription, not ATP6 transcription, although both genes are encoded by the H-strand (Figure IV-2C). In contrast to Mito-Chlor, chlorambucil did not inhibit the steady-state RNA levels of any of these three genes (Figure IV-2C). It is interesting to note the different results obtained with Bru-seq and RT-PCR of Mito-Chlor. A potential explanation for this is that RT-PCR quantifies the steady-state levels of total RNAs while Bru-seq only measures the newly synthesized RNA.

The mitochondrial membrane potential ($\Delta\Psi_m$, MMP), generated by proton pumps, is critical for the physiological function of mitochondria. We next investigated whether these agents would affect MMP using tetramethylrhodamine methyl ester (TMRM), a cell-permeable dye that accumulates in active mitochondria with intact membrane potentials. After a 4-hour treatment, Mito-Chlor displayed significant decrease in the TMRM fluorescence level while SQD1 did not (Figure IV-2D). This result suggests that Mito-Chlor also interfered with mitochondrial physiological function when inhibiting the mitochondrial transcription at 4 h, while SQD1 did not.

In order to assess the effects of SQD1 and Mito-Chlor on mitochondrial function, we measured the ATP production in compound-treated MIA PaCa-2 cells in glucose and galactose medium (Figure IV-2E). In the glucose medium, mammalian cells generate ATP from both aerobic glycolysis in cytoplasm and mitochondrial OXPHOS. Galactose medium where galactose is the sole sugar source for mammalian cells will force them to rely on mitochondrial

OXPPOS, instead of glycolysis, to produce ATP¹⁷. FCCP (carbonyl cyanide-4-(trifluoromethoxy)phenylhydrazone) the uncoupler of mitochondrial OXPPOS was used as a positive control¹⁸. After 24-hour treatment, FCCP, the uncoupler of mitochondrial OXPPOS showed a significant decrease in ATP production in galactose medium as compared to glucose medium, so did Mito-Chlor, while only marginal difference was observed with SQD1 treated groups (Figure IV-2E). This result suggests that the Mito-Chlor impaired ATP production by the mitochondrial OXPPOS while SQD1 did not.

Furthermore, we performed immunoblot on three mitochondrial proteins to assess their protein expression (Figure IV-2F). Mito-Chlor displayed a dose-dependent decrease in protein levels of CYB, ATP6 and ND6 while SQD1 showed no reduction of these proteins. Therefore, although both SQD1 and Mito-Chlor inhibit the transcripts of mtDNA, Mito-Chlor finally decreases mitochondrial protein expression, impairs mitochondrial physiological function and inhibits mitochondrial OXPPOS; the effects of SQD1 is limited on mitochondrial transcription level. Therefore, Mito-Chlor has a more solid profile on regulating mitochondrial function, in terms of transcripts, proteins, and function.

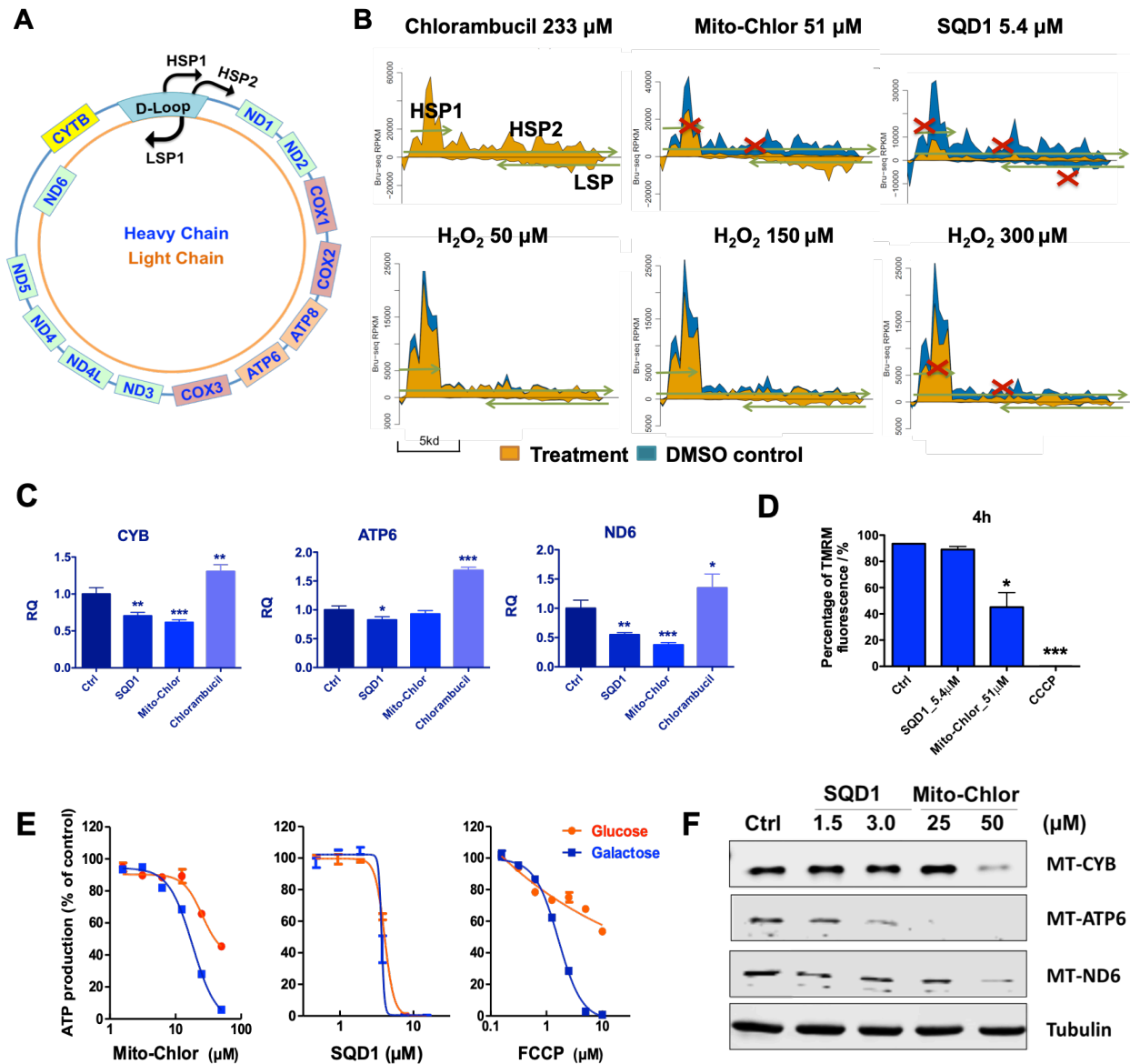


Figure IV-2. The effects of SQD1 and Mito-Chlor on mitochondrial transcription, mitochondrial proteins and ATP production. (A) Transcription from the mitochondrial genome occurs on the L-strand (orange) and the H-Strand (blue) controlled by three promoters, HPS1, HSP2, and LSP1. (B) Bru-seq trace diagrams of the mitochondrial transcripts after treatment with chlorambucil, Mito-Chlor and SQD1 in MIA PaCa-2 cells. Chlorambucil showed no effects on mitochondrial transcription, while Mito-Chlor blocked the transcription from the H-strand promoters. SQD1 treatment inhibited transcription from all three promoters. (C) SQD1 and Mito-Chlor reduce mitochondrial RNA levels of CYB, ATP6 and ND6 genes as represented by relative quantification (RQ) values determined from RT-PCR. Treatment conditions are the same as the Bru-seq experiments. * denotes $p < 0.05$, ** $p < 0.005$, and *** $p < 0.0005$. (D) TMRM measurement of mitochondrial membrane potential (MMP) in MIA PaCa-2 cells treated by SQD1 and Mito-Chlor at 4 h. CCCP (carbonyl cyanide 3-chlorophenylhydrazine) was used as a positive control. Treatment conditions are the same as the Bru-seq experiments. (E) ATP production measurement of SQD1, Mito-Chlor and FCCP-treated MIA PaCa-2 cells in glucose and galactose medium. (F) Immunoblot of MT-CYB, MT-ATP6 and MT-ND6 at 24 h treatment.

Mito-Chlor and SQD1 induce similar transcription profiles

Besides targeting mitochondrial transcription effect, we further analyzed genome-wide transcriptomic profile of SQD1 and Mito-Chlor to understand its working mechanism in the cells. After comparing with DMSO control, SQD1- and Mito-Chlor-treated samples have in total 12,336 common expressed genes with a strong Pearson correlation (r) of 0.52 ($p < 2.2e-16$) (Figure IV-3A). The common upregulated genes ($\log_2FC > 1$) have an r value of 0.45 ($p < 2.2e-16$), and their common downregulated genes ($\log_2FC < -1$) have an r value of 0.34 ($p < 2.2e-16$) (Figure IV-3B, 3C). 19 of top 25 upregulated and 19 of top 25 downregulated protein-coding genes from SQD1 treatment were also altered in the Mito-Chlor-treated sample in the same direction.

Examining the upregulated genes induced by SQD1 revealed some clues to its mechanism of action (Table VI-1). *HMOX1*, with the highest fold change ($FC=315.4$), encodes heme oxygenase 1 (HO-1), a protein that participates in the cellular defense against oxidative injury¹⁹. Upregulated genes *HK2*, *PFKFB4*, *DDIT4*, *ENO2* and *HILPDA* are related to HIF-1 (hypoxia-inducible factor 1) signaling and the hypoxic response²⁰⁻²². SQD1 increased the transcription of a series of hypoxia-related genes. Genes related to biosynthesis and canonical glycolysis pathways were also induced, such as the expression of *HK2*, *PFKFB4*, *ENO2*, *UPRT*, and *PGK1*. The protein FOS ($FC = 19.1$) dimerizes with JUN ($FC = 24.6$) to form the transcription factor complex AP-1^{23,24}. Elevation of AP-1 regulates genes involved in cell growth, cell differentiation, and cell death^{24,25}. Besides *FOS* and *JUN*, the transcription of *BHLHE40*, *C10orf10*, and *CSRNP1*, involved in transcription activation, were also highly increased. Furthermore, SQD1 elevated the transcription of autophagy-related genes, such as *BNIP3L*,

MAP1LC3B, and *GABARAP1I*. Taken together, SQD1 induced a series of genes related to oxidative stress, transcription activation, metabolic pathways and cell death.

Gene set enrichment analysis (GSEA) is a computational method that identifies classes of genes that are over-represented in a large set of genes^{26,27}. According to the GSEA results, 7 out of the top 20 upregulated gene sets and 10 out of the top 20 downregulated gene sets are in common between SQD1 and Mito-Chlor, indicating that they elicit similar responses in cells (Figure IV-3D, 3E). These gene sets are related to hypoxic response, redox signaling, MAPK signaling, cell proliferation, cell cycle and cell differentiation (Table IV-2). For the SQD1-treated sample, hypoxia-related gene sets account for 11 out of the top 25 upregulated gene sets. The downregulated gene sets imply that SQD1 affects cell proliferation, cell cycle, and cell differentiation. Overall, SQD1 treatment induces cell signaling involved in hypoxic response, transactivation, glycolysis, and autophagy.

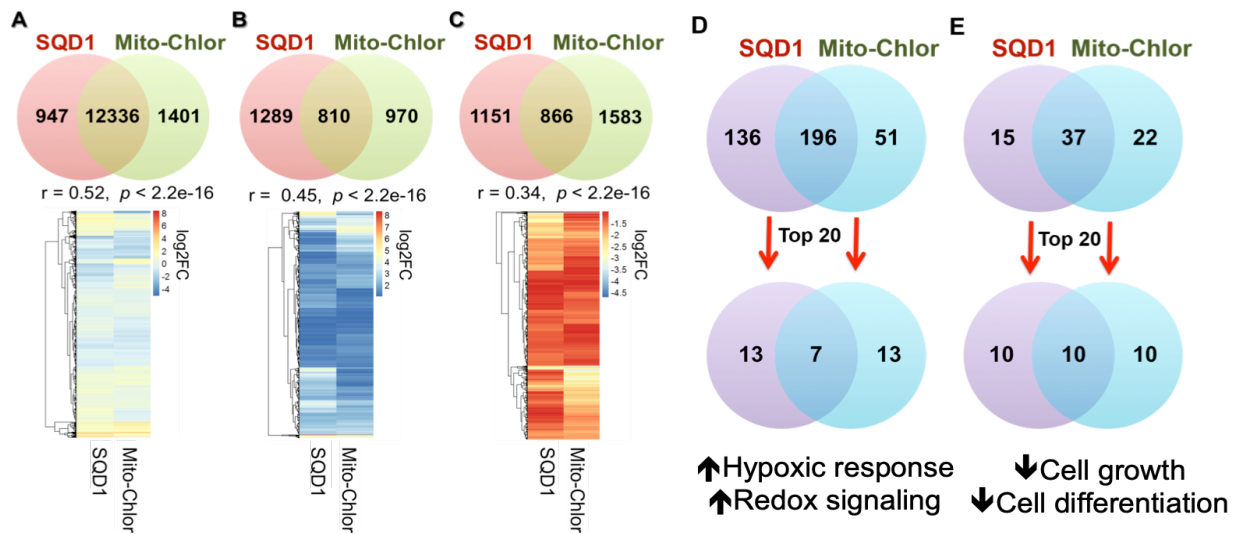


Figure IV-3. SQD1 and Mito-Chlor share similar transcriptomic profiles and enriched gene sets. The comparisons between SQD1 and Mito-Chlor are displayed in heatmaps. (A) Total common genes. (B) Common upregulated genes. (C) Common downregulated genes. r is Pearson correlation. SQD1 and Mito-Chlor also share common upregulated (D) and downregulated (E) enriched gene sets with FDR < 0.001. Top 20 enriched gene sets ranked by FDR values were also compared between the two samples.

Table IV-1. Top 25 protein-coding genes upregulated by SQD1 in MIA PaCa-2 cells. FC, fold change.

Gene name	FC	Gene name	FC	Gene name	FC	Gene name	FC	Gene name	FC
<i>HMOX1</i>	315.4	<i>ADM</i>	40.0	<i>BHLHE40</i>	30.2	<i>HSPA1A</i>	28.3	<i>GABARAPL1</i>	24.1
<i>ANKRD37</i>	56.1	<i>DDIT4</i>	37.1	<i>MAP1LC3B</i>	29.6	<i>CSRNPI</i>	24.9	<i>HSPH1</i>	22.3
<i>HK2</i>	53.2	<i>BNIP3L</i>	34.7	<i>ENO2</i>	29.1	<i>UPRT</i>	24.6	<i>PGK1</i>	22.1
<i>PFKFB4</i>	40.9	<i>CXCL8</i>	31.7	<i>C10orf10</i>	28.8	<i>JUN</i>	24.6	<i>TRIB3</i>	21.3
<i>SCAND2P</i>	40.3	<i>LUCAT1</i>	31.0	<i>HSPA1B</i>	28.4	<i>HILPDA</i>	24.5	<i>FAM162A</i>	21.0

Table IV-2. Common upregulated (A) and downregulated (B) enriched gene sets among the top 20 of SQD1 and Mito-Chlor.

(A)

Common upregulated enriched gene sets

PODAR_RESPONSE_TO_ADAPHOSTIN_UP
 CONCANNON_APOPTOSIS_BY_EPOXOMICIN_UP
 HELLER_SILENCED_BY_METHYLATION_DN
 GROSS_HYPOXIA_VIA_ELK3_DN
 NAGASHIMA_NRG1_SIGNALING_UP
 NAGASHIMA_EGF_SIGNALING_UP
 ZWANG_CLASS_3_TRANSIENTLY_INDUCED_BY_EGF

(B)

Common downregulated enriched gene sets

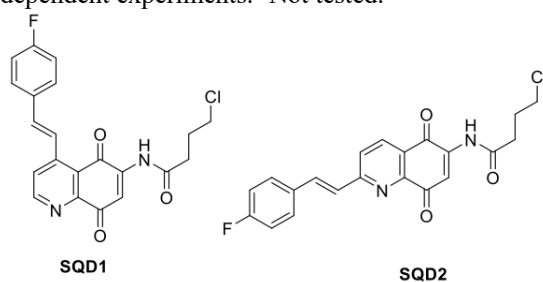
KONG_E2F3_TARGETS
 LEE_EARLY_T_LYMPHOCYTE_UP
 GRAHAM_NORMAL_QUIESCENT_VS_NORMAL_DIVIDING_DN
 GARGALOVIC_RESPONSE_TO_OXIDIZED_PHOSPHOLIPIDS_TURQUOISE_DN
 DUTERTRE ESTRADIOL_RESPONSE_24HR_UP
 ROSTY_CERVICAL_CANCER_PROLIFERATION_CLUSTER
 CHANG_CYCLING_GENES
 GOBERT_OLIGODENDROCYTE_DIFFERENTIATION_UP
 ZHANG_TLX_TARGETS_DN
 FUJII_YBX1_TARGETS_DN

Evaluation of the cytotoxicity and ROS induction capability of SQD1 and Mito-Chlor

We synthesized SQD1 and SQD2 to investigate the influence of styryl substitution. The 4-styryl analog SQD1 ($IC_{50} = 1.3 \pm 0.18 \mu M$) is more potent than 2-styryl analog SQD2 ($IC_{50} =$

3.9 ± 0.3 μM). Antiproliferative activity of SQD1 and Mito-Chlor was evaluated in MIA PaCa-2 cells with and without antioxidants due to their potential effects on redox signaling. The combination with NAC significantly decreased the cytotoxicity of SQD1, implying that intracellular thiol-containing molecules may contribute to the detoxification of SQD1. The combination of vitamin E (Vit-E) slightly reduced the cytotoxicity of SQD1, again, suggesting that elevated oxidative stress within cells may contribute to their cytotoxicity (Table IV-3, Figure IV-4A). The rescue effect of NAC was also observed for Mito-Chlor, indicating that the cytotoxicity of Mito-Chlor is linked to ROS (Table IV-3, Figure IV-4A). Additionally, SQD1 displayed similar cytotoxicity across different cancer cells (Table IV-4).

Table IV-3. Cytotoxicity of SQD1, SQD2 and Mito-Chlor in MIA PaCa-2 cells. ^aIC₅₀ data are shown as mean ± standard deviation from three independent experiments. ^bNot tested.



ID	IC ₅₀ (μM) ^a	+2 mM NAC	+0.5 mM vit-E
SQD1	1.3 ± 0.2	9.8 ± 3.8	2.1 ± 0.6
SQD2	3.9 ± 0.3	NT ^b	NT
Mito-Chlor	42.0 ± 2.0	> 50	>50

Table IV-4. Cytotoxicity of SQD1 in a panel of cancer cell lines. IC₅₀ (μM) values are shown as mean ± standard deviation from three independent experiments.

	MDA- MB-231	MDA- MB-468	T-47D	HUCCT1	TFK1	BxPC-3	PANC-1	KYSE- 410	KYSE- 70
SQD1	3.2 ± 0.9	1.1 ± 0.2	1.2 ± 0.2	1.5 ± 0.6	5.6 ± 2.6	2.4 ± 0.2	1.1 ± 0.1	3.5 ± 0.1	2.9 ± 0.3

Furthermore, we used CM-H₂DCFDA dye, a general oxidative stress indicator, to measure ROS induced by SQD1 and Mito-Chlor^{28,29}. Relative fluorescence unit (RFU) represents the relative level of cellular ROS. SQD1 induced a moderate increase in the fluorescence while Mito-Chlor caused a significant increase in a time-dependent manner (Figure IV-4B). Moreover, the elevated fluorescence signal could be attenuated by NAC and Vit-E (Figure IV-4C), indicating that the ROS levels are increased upon compound treatments in MIA PaCa-2 cells. Dihydroethidium (DHE) was used as an independent redox probe for the detection of superoxide and hydrogen peroxide^{30,31}. The histogram shows a right shift of the DHE fluorescence in SQD1- and Mito-Chlor-treated samples as compared with the control, suggesting increased oxidative stress (Figure IV-4D).

Given the mitochondrial transcription inhibition effect of SQD1 and Mito-Chlor, we next assessed mitochondrial superoxide level using the MitoSOX Red dye³². Mitochondrial complex III inhibitor, antimycin A, a well-established stimulus of mitochondrial superoxide and ROS production was used as a positive control. SQD1, Mito-Chlor and antimycin A treatment increased fluorescence signal due to the induction of mitochondrial superoxid (Figure IV-4E). In contrast, chlorambucil and TPP treatment did not alter the mitochondrial superoxide level.

In all, SQD1 and Mito-Chlor increased hydrogen peroxide, superoxide and other types of ROS in MIA PaCa-2 cells.

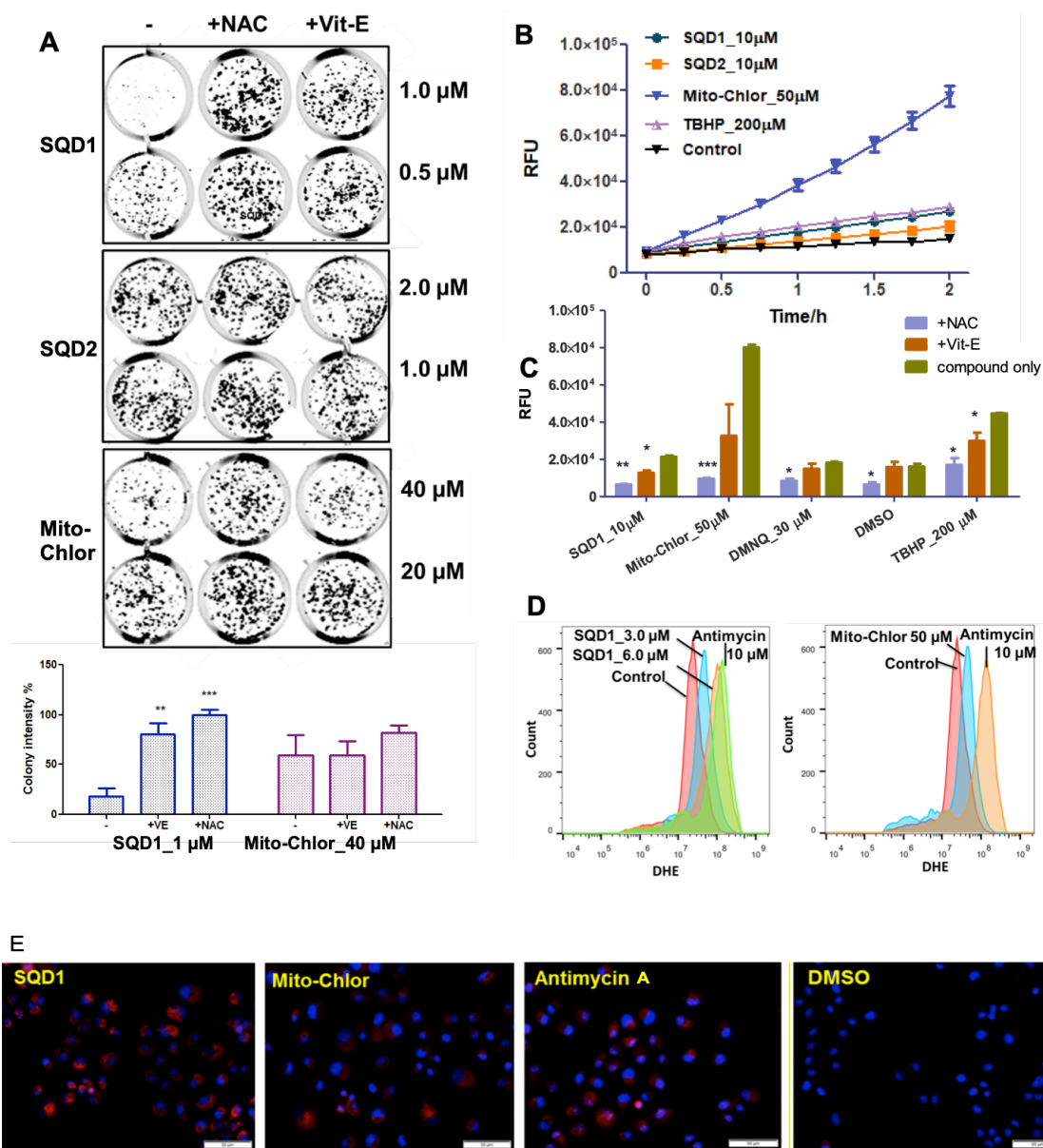


Figure IV-4. SQD1 and Mito-Chlor inhibit cell growth and increase ROS levels in MIA PaCa-2 cells. (A) NAC (2.0 mM) or Vit-E (0.5 mM) protected cytotoxicity of SQD1 and Mito-Chlor. (B) Relative fluorescence unit (RFU) was measured at indicated time using CM-H2DCFDA dye. Tert-butyl hydroperoxide (TBHP) was used as a positive control. (C) The RFU of compound-treated MIA PaCa-2 cells in the presence or absence of Vit-E (0.5 mM) or NAC (3 mM) after 1-hour treatment. * denotes $p < 0.05$, ** $p < 0.005$. (D) Detection of superoxide and hydrogen peroxide in MIA PaCa-2 cells treated with SQD1 (5.4 μM), Mito-Chlor (51 μM), antimycin A (15 μM) or DMSO using DHE dye. (E) Detection of mitochondrial superoxide using MitoSOX Red superoxide indicator (2 μM) with fluorescence microscope. Objective: 20x.

SQD1 and Mito-Chlor induced similar protein expression patterns

Immunoblot analysis of some proteins involved in the pathways from the GSEA analysis and encoded by the top upregulated protein-coding genes from SQD1 samples revealed that SQD1 treatment caused a robust increase in the expression of 6 proteins (Figure IV-5). These proteins are mostly involved in oxidative stress (HMOX1), transactivation (FOSB, C-JUN), metabolism regulation (HK2, PFKFB4), and induction of autophagy (MAPLC-3 α/β , GABARAPL). The substantial upregulation of the components of transcription activator AP-1, JUN and FOS are likely to be responsible for the strong trend of transcription activation induced by the two compounds. As previously discussed, the most upregulated gene, HMOX1, its protein expression level increased during oxidative injury^{19,33}. SESN2 (encoding the protein sestrin 2) is another antioxidant induced under oxidative and genotoxic stress to protect cells against ROS was also significantly upregulated³⁴. The mitochondrial genome is especially vulnerable to oxidative damage since it does not contain protective histones³⁵. Oxidatively damaged mitochondria can be eliminated through autophagy to prevent excessive ROS production^{36,37}. The significant increase in GABARAPL and MAPLC-3 α/β levels may indicate the induction of autophagy. SQD1 also upregulated protein expression of HK2 and PFKFB4, suggesting enhanced glycolysis (Figure IV-5).

H₂O₂ triggers similar changes in protein levels of FOSB, c-JUN, HMOX1, HK2, PFKFB4, MAPLC-3 α/β , and GABARAPL as compared to SQD1 (Figure IV-5). The antioxidant NAC attenuates the protein changes caused by SQD1 and H₂O₂, supporting the hypothesis that the induced cellular ROS had profound influences on the downstream signaling of SQD1 (Figure IV-5). Mito-Chlor also dose-dependently induced the expression levels of HMOX1, SESN2, FOSB, MAPLC3 α/β , and c-JUN proteins, similar to SQD1 (Figure IV-5A, 5B). However, the

protein levels of glycolytic enzyme HK2, PFKFB4, and autophagy-related protein GABARAPL were not altered by Mito-Chlor (Figure IV-5A, 5B). The addition of NAC protected the upregulation of transcription activator AP-1 and HMOX1 induced by Mito-Chlor but had negligible influence on the expression levels of SESN2 and MAPLC3 α/β (Figure IV-5).

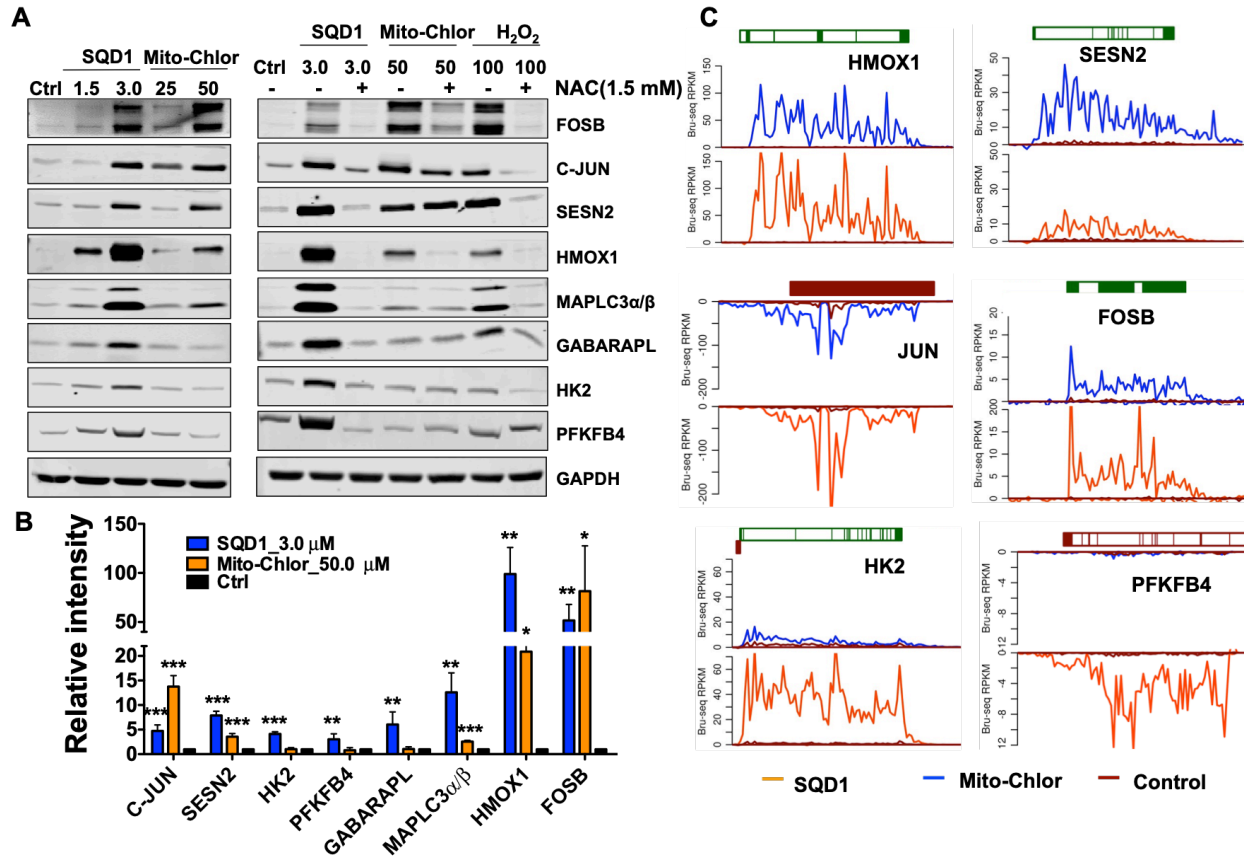


Figure IV-5. SQD1, Mito-Chlor, and H₂O₂ induce similar changes in protein expression in MIA PaCa-2 cells. (A) 24 h treatment of SQD1 upregulated the expression levels of FOSB, c-JUN, HMOX1, HK2, PFKFB4, MAPLC-3 α/β and GABARAPL in a dose-dependent manner. Mito-Chlor treatment induced similar protein expression changes with the exception of GABARAPL, HK2, and PFKFB4. SQD1-, Mito-Chlor- and H₂O₂-induced changes in select protein levels were rescued by the addition of 1.5 mM NAC. (B) Protein levels induced by SQD1 and Mito-Chlor were quantified by ImageJ and normalized to respective loading controls. The data are presented as mean \pm standard deviation of at least three independent experiments. * denotes $p < 0.05$, ** $p < 0.005$, and *** $p < 0.0005$. (C) Transcription trace diagrams of the representative genes after SQD1 or Mito-Chlor treatment. The positive y-axis represents plus-strand signal of transcription moving from left to right, and the negative y-axis represents minus-strand signal of transcription moving from right to left.

In summary, SQD1 and Mito-Chlor are identified as mitochondrial transcription inhibitors (Figure IV-6). Their redox-modulating capability could partially contribute to the

mitochondrial transcription inhibition because H_2O_2 itself is able to cause mitochondrial transcription inhibition (Figure IV-2). However, their transcription inhibition pattern and the pathways to ROS induction are different. The mitochondrial superoxide increased by Mito-Chlor could be a downstream effect of its targeting and alkylating effects on mtDNA. SQD1, as a quinone redox recycler, it may also react with cysteines of some proteins, deplete GSH or alkylate DNA, resulting in cellular oxidative stress (Figure IV-6). Increasing studies have shown that mtDNA damage causes impairment of the respiratory complexes and a concomitant increase in mitochondrial ROS, leading to a vicious feed-forward cycle of additional mtDNA damage and ROS production³⁵. Furthermore, mtDNA damage could alter mitochondrial gene expression and interfere with mtDNA replication³⁵. Although SQD1, Mito-Chlor, and H_2O_2 all exhibit mitochondrial transcription inhibition, their transcriptional repression patterns and mitochondrial protein regulations are different.

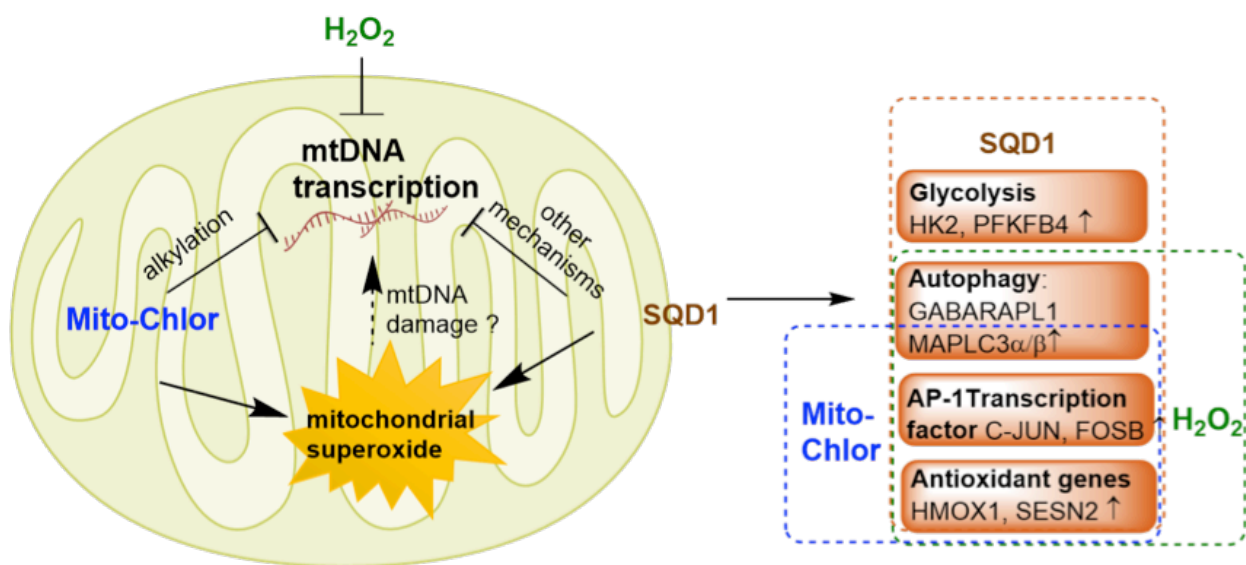


Figure IV-6. Proposed mechanisms of action of SQD1 and Mito-Chlor, and the adaptation pathways of pancreatic cancer cells in response to SQD1 and Mito-Chlor.

In this study, we demonstrate that Mito-Chlor represses transcription of the mitochondrial genome while its parent compound, chlorambucil, does not. A search of other small molecules that block transcription of mtDNA identified a novel quinone compound SQD1. Furthermore, the transcriptomic profile of Mito-Chlor was similar to that of SQD1 and both of these compounds induced mitochondrial superoxide and similar changes in protein expression in MIA PaCa-2 cells. SQD1, although deprived of a mitochondrial-directing group, shows promise in targeting mitochondria DNA via mitochondrial superoxide and other mechanisms. Taken together, as mitochondrial transcription inhibitors, SQD1 and Mito-Chlor are promising probes for the study of cell death related to mitochondrial function and oxidative stress.

Materials and methods

Cell culture and reagents. MIA PaCa-2, BxPC-3, PANC-1, KYSE-410, KYSE-70, and T-47D were cultured in RPMI 1640 medium supplemented with 10% FBS (v/v). MDA-MB-468 and MDA-MB-231 were cultured in L-15 medium supplemented with 10% FBS (v/v). HUCCT1 was cultured in RPMI 1640 medium supplemented with 1% penicillin/streptomycin (v/v) and 10% FBS (v/v). TFK1 cells was cultured in RPMI 1640 medium supplemented with penicillin/streptomycin (50 U/mL) and 10% FBS (v/v). Cells were maintained at 37 °C in a humidified atmosphere of 5% CO₂. They were maintained in culture under 40 passages and tested regularly for *mycoplasma* contamination using Plasco Test (InvivoGen).

Chemicals. All commercial chemicals and solvents used for synthesis were reagent grade and were used without further purification unless otherwise specified. Chlorambucil was purchased from Oakwood Products, Inc., and Mito-Chlor was synthesized as described ¹².

Western blotting and antibodies. Cells were lysed in RIPA buffer (25 mM Tris-HCl, pH =7.4, 150 mM NaCl, 1% Nonidet P-40, 0.5% Sodium deoxycholate, 0.1% SDS) supplemented with

Halt Protease and Phosphatase Inhibitor Cocktail (Thermo Scientific, 78443). Protein concentration was determined by BCA protein assay kit (Thermo Scientific, 23228, 23224). Unless otherwise described, 25-30 μg of protein was resolved by SDS–polyacrylamide gel electrophoresis (PAGE). Antibodies used for Western blots include C-Jun (Santa Cruz, SC-74543), SESN-2 (Santa Cruz, SC-393195), HK2 (ThermoFisher, 700422), PFKFB4 (ThermoFisher, PA5-15475), HMOX1 (Thermo Fisher, MA1-112), MAP LC3 α/β (Santa Cruz, SC-398822), FOSB (Cell Signaling, 2251T), GAPDH (Cell Signaling, 2118S), GABARPAL1 (Cell Signaling, 26632S), PARP (Cell Signaling, 9542S), Cleaved PARP (Cell Signaling, 5625), p-H2AX (Cell Signaling, 9718), MT-CYB (Abcam, ab81215), MT-ATP6 (Abcam, ab192423), MT-ND6 polyclonal antibody (Thermo Fisher, PA5-43532) and tubulin (Santa Cruz, SC-101527).

Colony formation assay. Cells were seeded in 24-well tissue culture plates at a density of 500 cells per well or 96-well plates at 250 cells per well. After overnight attachment, cells were treated with compounds for 24 h. NAC or vitamin-E was added 1 h prior to the compound treatments. Then, the media containing compounds was removed and fresh media was added. After 7–10 days, when colonies had fully formed in the DMSO-treated wells, cells were stained with a 0.05% crystal violet solution for 30 min, and then washed with ddH₂O to remove excess stain. Plates were imaged using Odyssey Imaging Systems (LI-COR Biosciences) after overnight drying. The colony density was quantified by Licor and ImageJ.

CM-H₂DCFDA ROS assay. MIA PaCa-2 cells were seeded in 96-well flat clear-bottom black tissue culture plates at a density of 1.5×10^4 per well. After overnight attachment, the media was removed and 100 μL CM-H₂DCFDA dye (10 μM , Thermo Fisher, C6827) in HBSS was added to each well at 37 °C for 35–40 min. After removal of the dye solution, cells were washed with

pre-warmed DPBS for 2 times and then 80 μ L HBSS was added. After pretreatment with or without NAC (3 mM), tested compounds were added in HBSS solution at designated concentrations. Fluorescent signal was then measured using CLARIO Star plate reader (Ex: 483 \pm 15M; Em: 530 \pm 20 nM).

Bru-seq experiment and analysis. MIA PaCa-2 cells were seeded in 10 cm dishes in duplicates. Twenty-four hours later, cells were treated with DMSO, SQD1 (5.4 μ M), Mito-Chlor (51 μ M), Chlor (233 μ M) or H₂O₂ (50 μ M, 150 μ M and 300 μ M) for 4 h. Bromouridine (Bru) was added to the media during the last 30 min of treatment to a final concentration of 2 mM as previously described¹³. Cells were then collected in TRIZOL and total RNA was isolated. The Bru-labeled nascent RNA was immunocaptured using anti-BrdU antibodies conjugated to magnetic beads. The cDNA libraries (Illumina TrueSeq) converted from the bromouridine-labeled RNA were sent for deep sequencing to the University of Michigan Sequencing Core. Sequencing reads (~40 million per sample) were mapped to the hg38 reference genome. Enriched gene sets were analyzed using GSEA. Hierarchical clustering was performed using log₂FC of gene expression. R programming language (Version 3.5.1) was utilized to produce select figures.

MitoSOX imaging. MIA PaCa-2 cells were seeded in 96-well clear-bottom black tissue culture plates at a density of 5000 cells per well. After overnight attachment, media was removed and 100 μ L HBSS solution was added into each well. The cells were treated with SQD1 (5.4 μ M), Mito-Chlor (51 μ M), chlorambucil (233 μ M), TPP (51 μ M), antimycin A (15 μ M) or DMSO, respectively. After 1-hour incubation at 37°C, the medium was removed. HBSS working solution with 5 μ M MitoSOX dye (Thermo Fisher, M36008) and 4 μ g mL⁻¹ Hoechst 33342 (Thermo Fisher, H3570) were added and incubated for 15 minutes. Cells were then washed

gently three times with warm HBSS buffer before imaging by the OLYMPUS DP80 system with RFP and DAPI filters using the 20 X objective.

DHE staining analyzed by flow cytometry. MIA PaCa-2 cells were seeded in 6-well plates at a density of 400,000 cells per well. After overnight attachment, medium was removed, and the cells were washed with HBSS solution once. A solution of 5 μ M DHE dye in HBSS pre-warmed buffer was added to each well. After incubation at 37 °C for 30 min, tested compounds were added. Plates were covered and incubated for an additional hour at 37 °C and protected from light. Staining buffer was carefully aspirated, and 0.5 mL trypsin was added to detach the cells. Complete medium (0.5 mL) was added to each well to neutralize the trypsin and then cells were transferred to centrifugal tubes to pellet the cells. Supernatant was discarded and cells were resuspended in HBSS buffer. The fluorescence of DHE was measured using a flow cytometer (ZE5 cell analyzer, Bio-Rad) with excitation at 488 nm and emission at 530 nm. At least 10,000 events were collected. Histograms were analyzed by Flowjo (Version 8).

RNA preparation and real-time PCR (RT-PCR). MIA PaCa-2 cells were seeded into 6-well tissue culture plates at a density of 3×10^5 per well and allowed to attach overnight before treating with drugs at specified time. RNAs were collected using Direct-zol RNA Miniprep kit (Zymo Research). RNA (1 μ g) from each sample was reverse-transcribed into cDNA using the High-Capacity cDNA Reverse Transcription Kit (Applied Biosystems). RT-PCR was performed using Viiia 7 Real-Time PCR System (Thermo Scientific) with TaqMan Gene Expression Master Mix (Thermo Scientific). RT-PCR primers (MT-ND6, MT-ATP6, MT-CYB, HMOX1, GAPDH) were purchased from Thermo Scientific. Relative expression levels were normalized to GAPDH and fold changes in mRNA expression level were evaluated using the $2^{-\Delta\Delta C_t}$ method.

Mitochondrial membrane potential detection. MIA PaCa-2 cells were seeded into 6-well tissue culture plates at a density of 3×10^5 per well and allowed to attach overnight before treating with compounds at specified time. Cells were then resuspended and incubated with 20 nM TMRM (Thermo Fisher, M20036) in HBSS solution at 37 °C for 30 min and protected from light. CCCP (50 μ M) was used as a positive control. After removing the dye, the fluorescence intensity was measured by Bio-Rad ZE5 Analyzer flow cytometer (Ex: 561 nm; Em: 590 nm). The percentage of TMRM fluorescence level of the treatment groups compared to the control group represents the relative mitochondrial membrane potential.

Quantification of total cellular ATP in glucose and galactose medium. RPMI 1640 medium (Thermo Fisher, 11875101) was used as glucose medium. Galactose medium was prepared by adding 10 mM galactose (Sigma-Aldrich, G0750) to RPMI 1640 medium with no glucose (Thermo Fisher, 11879020). Cells were seeded into 96-well plates (Corning, 3603) at a density of 10,000 cells/well. The total cellular ATP content was determined 24 hours after compound treatment using the CellTiter-Glo® Luminescence Cell Viability Assay according to the manufacturer's protocol (Promega Corporation, G7570). Luminescence signals were quantified using a scanning microplate reader (BMG Labtech).

Immunoblot. MIA PaCa-2 cells were seeded into 6-well tissue culture plates for 2.5×10^5 cells per well and allowed to attach overnight before treating with appropriate compounds at indicated concentrations. Then, cells were lysed with RIPA buffer in the presence of protease and phosphatase inhibitors. The cells were collected, centrifuged and the pellet was discarded. Protein concentration of whole cell lysate in the supernatant was determined by BCA protein assay kit. Proteins were resolved on 8-15% SDS-PAGE and electrotransferred to transfer membrane (Immobilon®-FL). After incubating in blocking buffer (5% nonfat dry milk in TBST)

at room temperature for 1 h, membranes were probed with primary antibody (1:500–1:1000) in blocking buffer overnight at 4 °C. Next day, membranes were washed 3 times for 5 min with TBST, followed by incubation in anti-rabbit or anti-mouse secondary antibody (Dylight 800 4× PEG conjugated; Thermo Scientific; 1:5000) in blocking buffer at room temperature for 1 h. The membranes were washed 3 times with TBST and imaged by Odyssey® CLx Imaging System. Protein levels were quantified by ImageJ 1.52a and the relative density of each band was normalized by respective loading controls.

Statistical analysis. Statistical analysis was conducted using GraphPad Prism (Version 6.0), R programming (Version 3.5.1). All data are shown as mean \pm standard deviation from at least 3 independent experiments. Significance levels for assays and immunoblots were determined using the unpaired Student's *t*-test between two groups using Microsoft Excel. Significance levels for transcriptomic profile comparisons were calculated using R.

Author contributions

Wenmin Chen and Shuai Hu are equally contributed primary authors. Shuai Hu and Mats Ljungman conducted the bioinformatics analysis. Shuai Hu conducted RT-PCR experiments, and Wenmin Chen performed the DHE staining. Michelle T. Paulsen performed the Bru-seq experiments. Wenmin Chen, Shuai Mao, Haoxi Li and Xinde Chen synthesized the SQD compounds. Yibin Xu performed the cellular ATP assay. Other experiments were performed by Shuai Hu and Wenmin Chen. Nouri Neamati is the corresponding author.

References

1. Wallace, D. C. Mitochondria and cancer. *Nat. Rev. Cancer* 12, 685–698 (2012).
2. Porporato, P. E., Filigheddu, N., Pedro, J. M. B.-S., Kroemer, G. & Galluzzi, L. Mitochondrial metabolism and cancer. *Cell Research* vol. 28 265–280 (2018).
3. Vyas, S., Zaganjor, E. & Haigis, M. C. Mitochondria and Cancer. *Cell* vol. 166 555–566 (2016).
4. Pathania, D., Millard, M. & Neamati, N. Opportunities in discovery and delivery of anticancer drugs targeting mitochondria and cancer cell metabolism. *Adv. Drug Deliv. Rev.* 61, 1250–1275 (2009).
5. Weinberg, S. E. & Chandel, N. S. Targeting mitochondria metabolism for cancer therapy. *Nat. Chem. Biol.* 11, 9–15 (2015).
6. Battogtokh, G. *et al.* Mitochondria-targeting drug conjugates for cytotoxic, anti-oxidizing and sensing purposes: current strategies and future perspectives. *Acta Pharm Sin B* 8, 862–880 (2018).
7. Murphy, M. P. & Hartley, R. C. Mitochondria as a therapeutic target for common pathologies. *Nature Reviews Drug Discovery* vol. 17 865–886 (2018).
8. Hamilton, P. L. & Arya, D. P. Natural product DNA major groove binders. *Nat. Prod. Rep.* 29, 134–143 (2012).
9. Rodríguez-Enríquez, S., Marín-Hernández, A., Gallardo-Pérez, J. C., Carreño-Fuentes, L. & Moreno-Sánchez, R. Targeting of cancer energy metabolism. *Molecular Nutrition & Food Research* vol. 53 29–48 (2009).
10. Madak, J. & Neamati, N. Membrane permeable lipophilic cations as mitochondrial directing groups. *Current Topics in Medicinal Chemistry* vol. 15 745–766 (2015).
11. Zielonka, J. *et al.* Mitochondria-targeted triphenylphosphonium-based compounds: syntheses, mechanisms of action, and therapeutic and diagnostic applications. *Chem. Rev.* 117, 10043–10120 (2017).
12. Millard, M., Gallagher, J. D., Olenyuk, B. Z. & Neamati, N. A selective mitochondrial-targeted chlorambucil with remarkable cytotoxicity in breast and pancreatic cancers. *J. Med. Chem.* 56, 9170–9179 (2013).
13. Paulsen, M. T. *et al.* Use of Bru-Seq and BruChase-Seq for genome-wide assessment of the synthesis and stability of RNA. *Methods* 67, 45–54 (2014).
14. Gustafsson, C. M., Falkenberg, M. & Larsson, N.-G. Maintenance and expression of mammalian mitochondrial DNA. *Annual Review of Biochemistry* vol. 85 133–160 (2016).
15. Yusoff, A. A. M., Ahmad, F., Idris, Z., Jaafar, H. & Abdullah, J. M. Understanding mitochondrial DNA in brain tumorigenesis. *Molecular Considerations and Evolving Surgical Management Issues in the Treatment of Patients with a Brain Tumor* (2015) doi:10.5772/58965.
16. Hu, S., Jin, Y., Liu, Y., Ljungman, M. & Neamati, N. Synthesis and mechanistic studies of

- quinolin-chlorobenzothioate derivatives with proteasome inhibitory activity in pancreatic cancer cell lines. *European Journal of Medicinal Chemistry* vol. 158 884–895 (2018).
17. Gohil, V. M. *et al.* Nutrient-sensitized screening for drugs that shift energy metabolism from mitochondrial respiration to glycolysis. *Nat. Biotechnol.* 28, 249–255 (2010).
 18. Kane, M. S. *et al.* Current mechanistic insights into the CCCP-induced cell survival response. *Biochemical Pharmacology* vol. 148 100–110 (2018).
 19. Gozzelino, R., Jeney, V. & Soares, M. P. Mechanisms of cell protection by heme oxygenase-1. *Annual Review of Pharmacology and Toxicology* vol. 50 323–354 (2010).
 20. Lendahl, U., Lee, K. L., Yang, H. & Poellinger, L. Generating specificity and diversity in the transcriptional response to hypoxia. *Nat. Rev. Genet.* 10, 821–832 (2009).
 21. Hata, S. *et al.* Hypoxia-induced angiopoietin-like protein 4 as a clinical biomarker and treatment target for human prostate cancer. *Oncology Reports* vol. 38 120–128 (2017).
 22. Wilson, G. K., Tennant, D. A. & McKeating, J. A. Hypoxia inducible factors in liver disease and hepatocellular carcinoma: current understanding and future directions. *J. Hepatol.* 61, 1397–1406 (2014).
 23. Vierbuchen, T. *et al.* AP-1 Transcription factors and the BAF complex mediate signal-dependent enhancer selection. *Mol. Cell* 68, 1067–1082.e12 (2017).
 24. Bejjani, F., Evanno, E., Zibara, K., Piechaczyk, M. & Jariel-Encontre, I. The AP-1 transcriptional complex: local switch or remote command? *Biochim. Biophys. Acta Rev. Cancer* 1872, 11–23 (2019).
 25. Shaulian, E. & Karin, M. AP-1 as a regulator of cell life and death. *Nature Cell Biology* vol. 4 E131–E136 (2002).
 26. Subramanian, A. *et al.* Gene set enrichment analysis: a knowledge-based approach for interpreting genome-wide expression profiles. *Proc. Natl. Acad. Sci. U. S. A.* 102, 15545–15550 (2005).
 27. Mootha, V. K. *et al.* PGC-1 α -responsive genes involved in oxidative phosphorylation are coordinately downregulated in human diabetes. *Nat. Genet.* 34, 267–273 (2003).
 28. Zlotkowski, K. *et al.* Macrophilone A: structure elucidation, total synthesis, and functional evaluation of a biologically active iminoquinone from the marine hydroid macrorhynchia philippina. *Org. Lett.* vol. 19 1726–1729 (2017).
 29. Marydasan, B. *et al.* In vitro and in vivo demonstration of human-ovarian-cancer necrosis through a water-soluble and near-infrared-absorbing chlorin. *J. Med. Chem.* vol. 61 5009–5019 (2018).
 30. Wardman, P. Fluorescent and luminescent probes for measurement of oxidative and nitrosative species in cells and tissues: progress, pitfalls, and prospects. *Free Radic. Biol. Med.* 43, 995–1022 (2007).
 31. NaveenKumar, S. K. *et al.* The role of reactive oxygen species and ferroptosis in heme-mediated activation of human platelets. *ACS Chem. Biol.* 13, 1996–2002 (2018).

32. Cheng, G. *et al.* Detection of mitochondria-generated reactive oxygen species in cells using multiple probes and methods: potentials, pitfalls, and the future. *J. Biol. Chem.* 293, 10363–10380 (2018).
33. Loboda, A., Damulewicz, M., Pyza, E., Jozkowicz, A. & Dulak, J. Role of Nrf2/HO-1 system in development, oxidative stress response and diseases: an evolutionarily conserved mechanism. *Cell. Mol. Life Sci.* 73, 3221–3247 (2016).
34. Shin, B. Y., Jin, S. H., Cho, I. J. & Ki, S. H. Nrf2-ARE pathway regulates induction of Sestrin-2 expression. *Free Radic. Biol. Med.* 53, 834–841 (2012).
35. Yang, Y. *et al.* Mitochondria and mitochondrial ROS in cancer: novel targets for anticancer therapy. *J. Cell. Physiol.* 231, 2570–2581 (2016).
36. Georgakopoulos, N. D., Wells, G. & Campanella, M. The pharmacological regulation of cellular mitophagy. *Nat. Chem. Biol.* vol. 13 136–146 (2017).
37. Pickles, S., Vigié, P. & Youle, R. J. Mitophagy and quality control mechanisms in mitochondrial maintenance. *Curr. Biol.* vol. 28 R170–R185 (2018).

CHAPTER V

Mechanistic Studies of Quinolin-Chlorobenzothioate Derivatives with Proteasome

Inhibitory Activity

The human 26S proteasome is an essential protein degradation machinery designated to maintain cellular homeostasis *via* removal of unfolded and misfolded proteins, and it is involved in balancing cell survival and apoptotic cell death. Importantly, small molecule proteasome inhibitors activate unfolded protein response leading to cancer cell death and are attractive for cancer therapy ^{1,2}. Bortezomib, ixazomib and carfilzomib were approved for treating multiple myeloma or mantle-cell lymphoma as proteasome inhibitors. They have boronic acid or epoxyketone scaffold, known to interact with the N-terminal threonine residues in the catalytic subunits of the proteasome thus blocking its activity (Figure V-1) ¹. Derivatives of the approved proteasome inhibitors have shown efficacy in multiple cancers and are currently undergoing clinical trials in solid tumors, including pancreatic cancer ¹⁻⁴. Unfortunately, patients frequently develop resistance to these therapies due to either point mutations on the drug binding site or induction of alternative compensatory mechanisms such as the aggresome pathway ⁵. Therefore, development of proteasome inhibitors with different scaffolds and mechanisms of action would be critical to overcome tumor cell resistance to first-line proteasome inhibitors.

Pancreatic cancer is a difficult cancer to treat due to its rapid metastatic spread and late-stage diagnosis ⁶. Pancreatic ductal adenocarcinoma (PDAC) is the major type of pancreatic

cancer and is predicted to become the second most common cause of cancer-related death within the next decade in the United States ^{7,8}. Pancreatic tumor cells can rapidly develop resistance to current chemotherapies, such as gemcitabine, nab-paclitaxel and FOLFIRINOX ^{9,10}. Thus, it is essential to develop more effective therapeutics to better treat this dreadful disease. Inhibition of the ubiquitin-proteasome pathway contributes to apoptotic cell death in pancreatic cancer ^{11,12}. Bortezomib sensitizes pancreatic cancer cells to endoplasmic reticulum (ER) stress and apoptosis¹³. Additionally, proteasome activator subunit 3 (PSME3) promotes pancreatic cancer growth by activating the proteasome activity ¹⁴. Therefore, the proteasome is an attractive target for therapeutics in pancreatic cancer.

In a medium-throughput phenotypic screen of 20,000 diverse drug-like compounds, we identified a quinolin-chlorobenzothioate, QCBT7, with submicromolar cytotoxicity in the colon carcinoma cell line HCT 116. It was previously shown that the structurally similar compound 8-quinolinethiol hydrochloride (8TQ) inhibits the essential proteasome deubiquitinase Rpn11, instead of the catalytic subunit of the proteasome, suggesting that QCBT7 may also affect proteasome function (Figure V-1) ¹⁵. Quinoline derivatives possess antibacterial, antimalarial and anticancer activities. Thioester, amide and ester derivatives of quinoline have been used in antimicrobial and anticancer research ¹⁶⁻¹⁹. To further identify new quinoline derivatives with potential proteasome inhibition and anticancer activities, we synthesized 21 analogs of QCBT7 to establish structural requirements for potency. We then profiled nascent RNA and protein expression in QCBT7-treated pancreatic cancer cells to understand how these cells respond to the treatment. Our results demonstrate that the induced transcription and protein patterns following QCBT7 treatment resemble those obtained for MG132 and ixazomib, indicating that QCBT7 blocks proteasome activity and induces hypoxic response, ER stress and glycolysis.

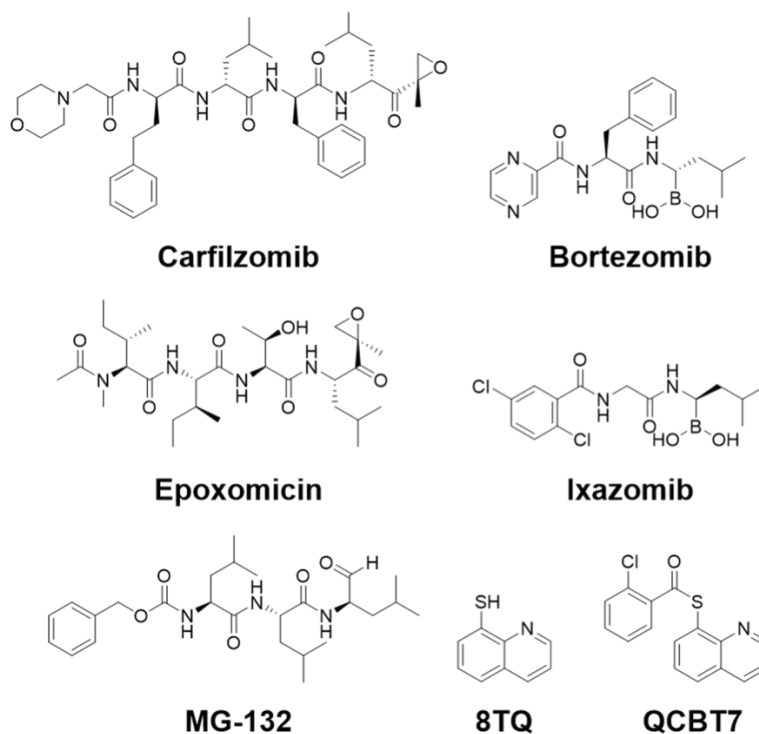


Figure V-1. Structures of select proteasome inhibitors and the lead compound QCBT7. Carfilzomib and epoxomicin are epoxyketone-based compounds, and bortezomib and ixazomib are boronate-containing compounds. MG132 is a peptide aldehyde. 8TQ is 8-quinolinethiol hydrochloride. QCBT7 has a similar scaffold to 8TQ.

Results and discussion

In a medium-throughput screen of 20,000 drug-like compounds derived from a diverse library, QCBT7 was one of the most cytotoxic hits and had an IC_{50} value of 0.6 μ M in HCT 116 cells²⁰. QCBT7 was further tested in the pancreatic cancer cell lines, showing IC_{50} values of 2.6 μ M and 1.1 μ M in MIA PaCa-2 and PANC-1 cells, respectively (Table V-1). Considering the stability of the thioesters in the cellular reducing environment, we synthesized ester and amide derivatives of QCBT7 to potentially increase the stability and maintain cytotoxicity.

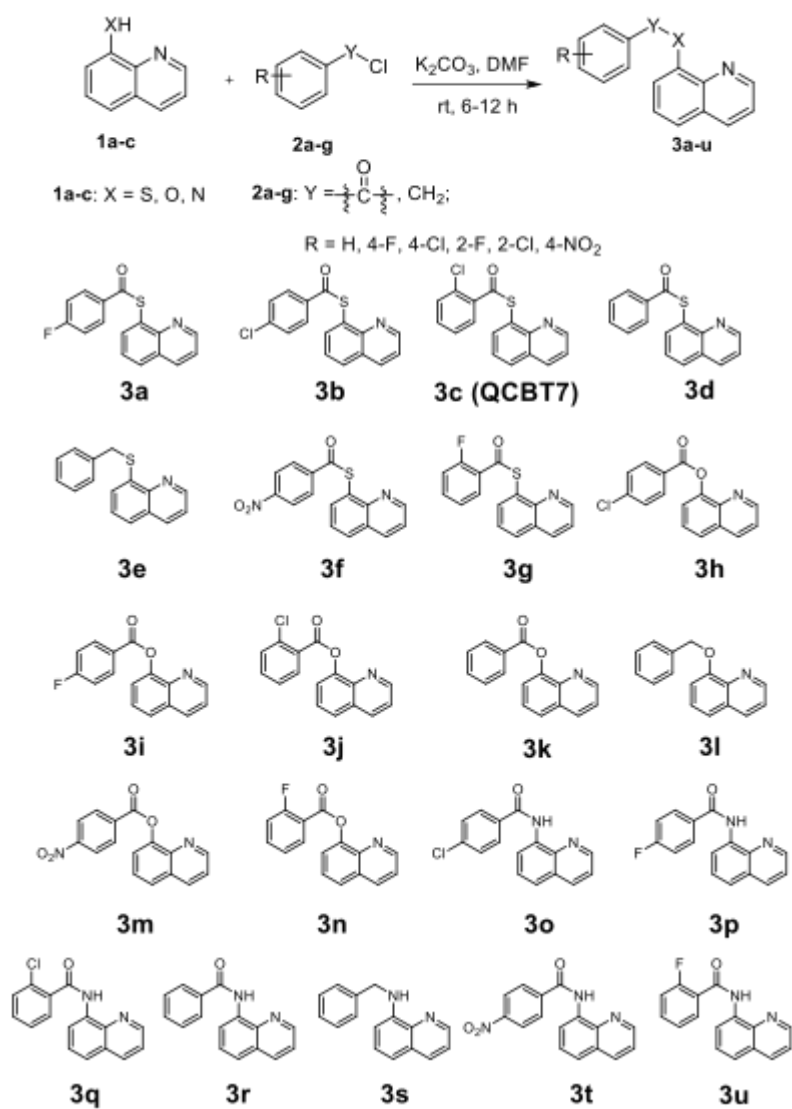
Table V-1. Cytotoxicity of 8-thioester/ester/amide-quinoline derivatives of QCBT7 in a panel of cancer cell lines. Data are shown as mean \pm standard deviation from at least three independent experiments.

Compound	IC ₅₀ (μ M)			
	MIA PaCa-2	PANC-1	HCT 116	KYSE-70
3a	3.3 \pm 0.2	1.5 \pm 0.4	1.1 \pm 0.4	1.1 \pm 0.3
3b	3.4 \pm 0.3	1.5 \pm 0.6	1.1 \pm 0.6	1.3 \pm 0.1
3c (QCBT7)	2.6 \pm 0.6	1.1 \pm 0.1	0.6 \pm 0.3	0.8 \pm 0.1
3d	2.4 \pm 0.8	0.9 \pm 0.3	0.5 \pm 0.3	0.7 \pm 0.1
3e	>20	>20	>20	>20
3f	4.9 \pm 3.3	1.7 \pm 0.1	1.5 \pm 0.6	0.9 \pm 0.2
3g	3.6 \pm 0.1	0.9 \pm 0.4	0.7 \pm 0.1	0.6 \pm 0.1
3h	10.3 \pm 5.6	9.4 \pm 4.4	4.7 \pm 1.5	11.8 \pm 0.5
3i	6.5 \pm 0.7	5.1 \pm 2.1	4.0 \pm 0.7	6.9 \pm 0.1
3j	6.5 \pm 0.1	7.1 \pm 1.1	3.0 \pm 0.8	15.2 \pm 5.7
3k	5.4 \pm 0.4	4.9 \pm 1.4	3.7 \pm 1.1	6.6 \pm 0.2
3l	>20	>20	>20	>20
3m	7.0 \pm 0.4	7.6 \pm 1.2	4.2 \pm 2.0	4.1 \pm 0.3
3n	5.8 \pm 0.8	5.5 \pm 0.2	2.9 \pm 0.1	6.5 \pm 0.3
3o	>20	>20	>20	>20
3p	>20	>20	>20	>20
3q	>20	>20	>20	>20
3r	>20	>20	>20	>20
3s	>20	>20	>20	>20
3t	>20	>20	>20	>20
3u	>20	>20	>20	>20

Synthesis of QCBT7 and its derivatives

Derivatives of QCBT7 were prepared according to the general procedure shown in Scheme IV-1 by Dr. Yi Jin. Benzoyl chloride or benzyl chloride was reacted with 8TQ, 8-hydroxyquinoline or 8-aminoquinoline, respectively, in the presence of potassium carbonate in dimethylformamide (DMF) to afford final products 3a-3u in 72-95% yields.

Scheme V-1. Preparation of QCBT7 derivatives.



8-thioester and 8-ester quinoline derivatives are more cytotoxic than 8-amide quinoline derivatives

Cytotoxicity of QCBT7 and its derivatives was assessed using the colorimetric MTT assay in a panel of cancer cell lines (Table V-1). The 8-thioester derivatives (3a-d, 3f, 3g) had similar IC_{50} values around 1 - 4 μ M, while the 8-ester derivatives (3h-k, 3m, 3n) were less potent (IC_{50} : 5-10 μ M). Different substituents on the benzene ring (R group in Scheme V-1) had little effect on the cytotoxicity of the compounds. The 8-amide derivatives (3o-r, 3t, 3u) were much less cytotoxic ($IC_{50} > 20 \mu$ M) although the amide-quinoline was more stable than the ester-quinoline and thioester-quinoline in the cellular reducing environment. The ether analogs 3e and 3l were inactive. These results suggest that the thioester-quinoline and ester-quinoline scaffolds are responsible for the cytotoxicity of this series of compounds. Due to the substantial reduction in cytotoxicity of the amide-quinoline derivatives and similar high potency among 8-thioester-quinoline analogs, we selected QCBT7 for further stability and mechanistic studies.

QCBT7 is more stable than 8TQ in solution

To assess the chemical stability of QCBT7, we performed liquid chromatography mass spectrometry (LCMS) of QCBT7 at three different time points after it was added to DMSO or to a 1:1 DMSO/water solution. N-acetylcysteine (NAC) was added in the solution to simulate a reducing environment and react with free thiols in the solution. 8TQ is the parent compound from which QCBT7 was synthesized, and is likely to be the functional scaffold for this series of compounds. QCBT7 was more stable than 8TQ under a range of conditions (Table V-2). In 100% DMSO, QCBT7 was still intact after seven days, while 8TQ formed dimers once it was dissolved in DMSO. Addition of NAC did not affect the results, and 8TQ also reacted with NAC

forming a conjugate at two and five hours. In a 1:1 solution of DMSO and water, 8TQ formed dimers within one minute, while QCBT7 was stable and present in a monomeric form after 48 hours. Additionally, NAC reacted with 8TQ as early as one minute, but did not react with QCBT7 in the 1:1 solution. In conclusion, QCBT7 is more stable than 8TQ in DMSO and 1:1 solution of DMSO and water, and NAC has little effect on QCBT7 even after 48-hour incubation. Therefore, we selected QCBT7, the more stable compound, for mechanistic studies

Table V-2. Stability of (a) QCBT7 and (b) 8TQ in DMSO and 1:1 DMSO/water solution with or without NAC. N/A: not measured at the time point.

(a) Percent of QCBT7 remaining				
Time / h	DMSO	DMSO+NAC	1:1 DMSO/water	1:1 DMSO/water+NAC
2	N/A	100	100	100
24	N/A	100	100	100
48	100 (> 7 days)	97.8	97.6	100
(b) Percent of 8TQ remaining				
Time / h	DMSO	DMSO+NAC	1:1 DMSO/water	1:1 DMSO/water+NAC
0.017	74.9	72.8	78.7	72.2
0.5	34.6	N/A	N/A	N/A
2	0	13.1	13.3	7.6
5	N/A	0	0	0

QCBT7 upregulates gene sets related to proteasome inhibition, unfolded protein response, glycolysis, and hypoxia

To better elucidate the potential mechanisms of action of QCBT7 in pancreatic cancer, we utilized Bru-seq technique to assess its effects on nascent transcription signatures in MIA PaCa-2 cells. After cells treated with 3.3 μ M QCBT7 for 4 h, we observed 326 upregulated genes with fold change (FC) over 2 and 127 downregulated genes with FC below 0.5 (Table V-3). In the set of upregulated genes, STRING analysis revealed three major biological processes:

carbon metabolism, HIF-1 signaling pathway and glycolysis ²¹. We performed gene set enrichment analysis (GSEA) using all the genes ranked by the log₂-fold change from the Bru-seq results ^{22,23}. The CONCANNON_APOPTOSIS_BY_EPOXOMICIN_UP gene set was ranked as the 13th enriched gene set of the C2 curated gene sets from the Molecular Signatures Database (MSigDB), suggesting that QCBT7 causes a similar transcriptional response to proteasome inhibitor epoxomicin (Figure V-2A). Epoxomicin is a potent, selective, irreversible and cell-permeable 20S proteasome inhibitor (Figure V-1) ²⁴. Additionally, we observed the enrichment of genes involved in the unfolded protein response (UPR), glycolysis and hypoxia in the Hallmark gene sets (Figure V-2B, 2C, 2D). Notably, a much higher number of hypoxia-related genes were upregulated (158) than downregulated (13) by QCBT7 (Figure V-2E). Other gene sets indicated that QCBT7 also stimulated the transcription of genes involved in apoptotic cell death. Taken together, the results from STRING and GSEA are consistent, and we hypothesize that QCBT7 causes proteasome inhibition, hypoxic response, glycolysis and unfolded protein response.

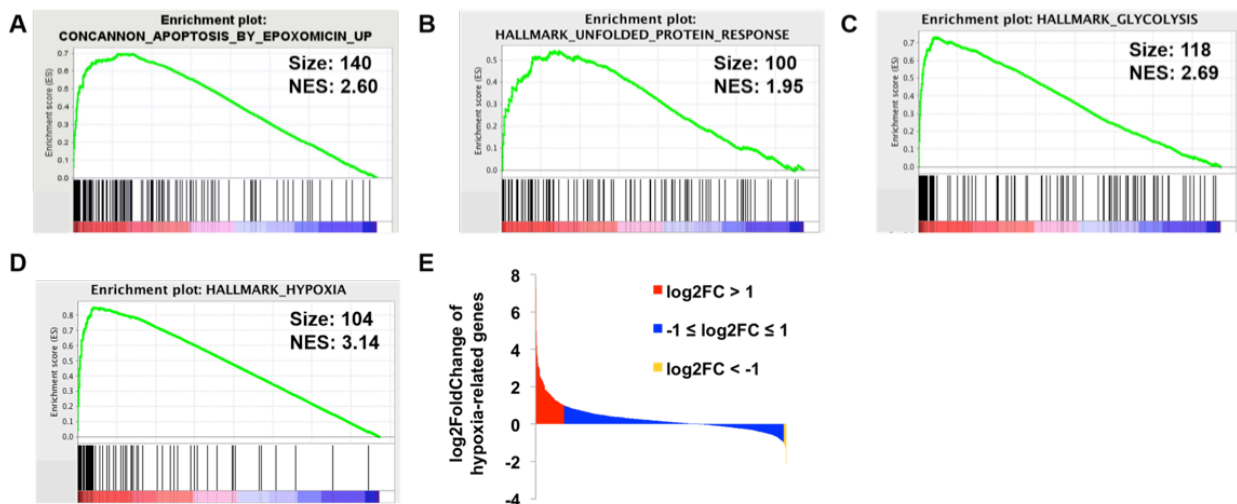


Figure V-2. QCBT7 upregulated the gene sets related to proteasome inhibition, unfolded protein response (UPR), glycolysis and hypoxic response. (A-D) GSEA enrichment plots for top enriched gene sets matched with upregulated genes from QCBT7 Bru-seq sample (FDR \leq 0.001). (A) Epoxomicin, a proteasome inhibitor. (B) UPR. (C) Glycolysis. (D) Hypoxia. Size is the number of genes, and NES is the normalized enrichment score for each gene set. (E) Log2FoldChange of 1387 hypoxia-related genes from QCBT7 Bru-seq results. 1 and -1 are used as the cutoff values for upregulated and downregulated genes.

Table V-3. Top 50 upregulated genes in QCBT7-treated MIA PaCa-2 cells. FC is fold change, defined as treatment over control. *HMOX1*, *PFKFB4*, *PDK1*, *PGK1*, *EGLN1*, *ENO2* and *HK2* are involved in the HIF-1 signaling pathway. *PGK1*, *ENO2*, *HK2* and *PGD* are related to carbon metabolism. *PGK1*, *ENO2* and *HK2* affect glycolysis.

Gene	FC	Gene	FC	Gene	FC	Gene	FC	Gene	FC
<i>HMOX1</i>	149	<i>BNIP3L</i>	15	<i>BTG1</i>	9	<i>ENO2</i>	8	<i>ZNF395</i>	6
<i>LOC344887</i>	45	<i>ADM</i>	14	<i>PGK1</i>	9	<i>GLA</i>	7	<i>GBE1</i>	6
<i>OSGIN1</i>	36	<i>GCLC</i>	13	<i>IL8</i>	9	<i>TXNRD1</i>	7	<i>PAM</i>	6
<i>PFKFB4</i>	32	<i>PDK3</i>	12	<i>ANGPTL4</i>	8	<i>EID3</i>	7	<i>HK2</i>	6
<i>MIR210HG</i>	30	<i>TNFSF9</i>	12	<i>NQO1</i>	8	<i>SRXN1</i>	7	<i>PGD</i>	6
<i>SLC7A11</i>	27	<i>FAM162A</i>	12	<i>EGLN1</i>	8	<i>P4HA1</i>	6	<i>INSIG2</i>	5
<i>DOK3</i>	24	<i>PDK1</i>	11	<i>DDIT4</i>	8	<i>JUNB</i>	6	<i>DUSP5</i>	5
<i>SCAND2</i>	23	<i>ARRDC3</i>	10	<i>DNAJB4</i>	8	<i>PIR</i>	6	<i>CCNG2</i>	5
<i>ANKRD37</i>	21	<i>RNF122</i>	9	<i>HILPDA</i>	8	<i>UPRT</i>	6	<i>RNF24</i>	5
<i>P4HA2</i>	19	<i>CHAC1</i>	9	<i>C3orf58</i>	8	<i>WSB1</i>	6	<i>ERO1L</i>	5

QCBT7 has similar expression signatures to proteasome inhibitors and hypoxia inducers

To further test our hypothesis that QCBT7 inhibits proteasome activity and induces hypoxia, glycolysis and ER stress, we performed connectivity map (CMAP) analysis of QCBT7 Bru-seq results (Table V-4) ²⁵. In the top 50 correlated perturbagens (small molecules and genetic reagents causing gene expression changes in cell lines), knockdown of PSMD1, PSMB5 and PSMA1 are listed, which encode different proteasome subunits. Additionally, proteasome inhibitors, such as MG132 and MLN-2238 (ixazomib), display similar expression signatures to QCBT7. Hypoxia-inducible factor (HIF) activators, such as VU-0418947-2 and VU-0418946-1, also show high similarity (high connectivity score), suggesting that QCBT7 induces hypoxic

response. Taken together, CMAP analysis supports the hypothesis that QCBT7 causes proteasome inhibition and elicits a hypoxic response.

Table V-4. Connectivity map analysis of QCBT7. Top compound perturbagens (CP), gene over-expression perturbagens (OE), gene knock-down perturbagens (KO) and perturbational class member (PCL) are listed. Pc_selection is the connectivity score (from -100 to 100). A positive higher score means more positive connection between the perturbagen and QCBT7.

Type	Name	Description	Pc_selection
CP	VU-0418947-2	hypoxia inducible factor activator	99.89
CP	VU-0418946-1	hypoxia inducible factor activator	99.86
CP	MG-132	proteasome inhibitor	99.58
CP	MLN-2238	proteasome inhibitor	99.3
OE	<i>NFE2L2</i>	basic leucine zipper proteins, nuclear factor (erythroid-derived 2)-like 2	99.91
KD	<i>PSMD1</i>	Proteasome subunits, proteasome (prosome, macropain) 26S subunit, non-ATPase, 1	99.82
KD	<i>PSMB5</i>	Proteasome subunits, proteasome (prosome, macropain) subunit, beta type, 5	99.61
KD	<i>PSMA1</i>	Proteasome subunits, proteasome (prosome, macropain) subunit, alpha type, 1	99.45
PCL	HIF activator	N/A	100
PCL	Proteasome inhibitor	N/A	99.72

QCBT7 and MG132 have similar transcriptional profiles

MG132, a peptide-aldehyde proteasome inhibitor, blocks the proteolytic activity of the 26S proteasome by covalently binding to the 20S catalytic subunit ²⁶. Due to its lack of specificity, it has only been used as a research tool to study the ubiquitin-proteasome pathway. In a separate study, we performed Bru-seq of MG132-treated HeLa cancer cells. Although a different cell line, we still identified similarity in the CONCANNON_APOPTOSIS_BY_EPOXOMICIN_UP gene set and WINTER_HYPOXIA_METAGENE gene set between QCBT7 and MG132.

QCBT7 and MG132 share 53 common upregulated enriched gene sets (FDR < 0.001) from C2 curated gene sets (Figure V-3A). Treatments with QCBT7 and MG132 induced 51 common genes contributing to the enrichment of the CONCANNON_APOPTOSIS_BY_EPOXOMICIN_UP gene set (Figure V-3B, 3C). Moreover, their transcript expressions were strongly correlated ($r = 0.69$, $p = 2.07e-08$) (Figure V-3D). STRING analysis indicates that the 51 common upregulated genes are involved in apoptotic signaling pathway, unfolded protein response and ER stress. Furthermore, we observed 22 common genes in the WINTER_HYPOXIA_METAGENE gene set from both QCBT7- and MG132-treated samples, and their nascent transcript expressions also had a strong correlation ($r = 0.68$, $p = 5.64e-04$) (Figure V-3E, 3F, 3G). These 22 genes are related to the HIF-1 signaling pathway, glycolysis and cellular stress.

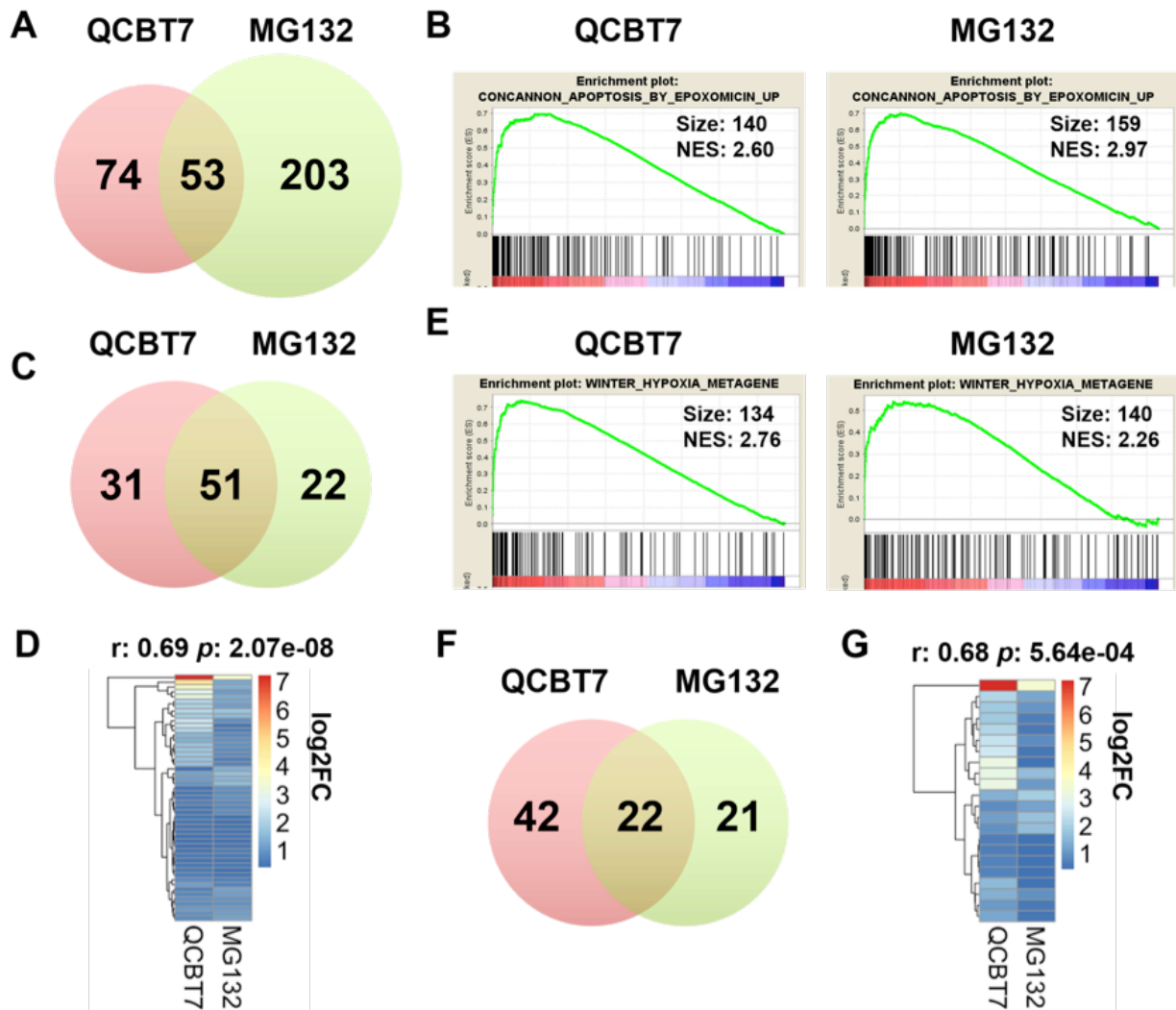


Figure V-3. QCBT7 and MG132 have common enriched gene sets in proteasome inhibition pathway and hypoxic response. (A) Venn diagram of all upregulated enriched gene sets between QCBT7 and MG132 (FDR < 0.001). (B) GSEA enrichment plots of CONCANNON_APOPTOSIS_BY_EPOXOMICIN_UP gene set in QCBT7 and MG132 Bru-seq samples. (C) 51 genes in common from the EPOXOMICIN gene set. (D) Heatmap of the 51 common genes using log₂FC ($r = 0.69$, $p = 2.07e-08$). (E) GSEA enrichment plots of WINTER_HYPOXIA_METAGENE gene set in two samples. (F) 22 genes in common from the HYPOXIA gene set. (G) Heatmap of the 22 common genes using log₂FC ($r = 0.68$, $p = 5.64e-04$).

Together, these results demonstrate that QCBT7 is similar to the proteasome inhibitor MG132 at the transcription level and regulates redox signaling and ER stress. GCLM, HMOX1, NQO1 and SQSTM1, from the 51 common genes in the EPOXOMICIN gene set, are involved in redox signaling pathways. GCLM encodes a glutamate-cysteine ligase modifier subunit, which is a rate-limiting enzyme for glutathione synthesis. HMOX1 (heme oxygenase 1)

responds to cellular oxidative stress and catalyzes cleavage of heme in order to maintain redox balance ²⁷. NQO1 (NAD(P)H quinone dehydrogenase 1) can also prevent oxidative stress *via* reducing quinones to hydroquinones. In addition, SQSTM1 (sequestosome 1) mediates the activation of NF- κ B signaling together with TNF receptor-associated factor 6, and is a positive regulator of Nrf2 signaling ²⁸. CEBPB, DDIT3 and PPP1R15A are three ER stress-related genes induced by both QCBT7 and MG132. Proteasome inhibitors may stimulate CEBPB, a transcription factor that interacts with DDIT3/CHOP, an ER stress biomarker, to induce cellular stress and cause cancer cell death ^{27,29}. PPP1R15A (GADD34) sensitizes cells to proteasome inhibitors by promoting ER stress, reactive oxygen species production and autophagy ³⁰.

Proteasome inhibitors can regulate redox homeostasis and induce ER stress ^{1,27}. MG132 has been shown to activate the Nrf2-ARE signaling pathway that protects cells from oxidative stress ³¹. The inhibition of proteasome activity caused by MG132 leads to the unfolded protein response and apoptosis ^{26,32}. The findings in our study are consistent with previous reports on the mechanisms of action of MG132. Moreover, they are similar to those of QCBT7 implied from the STRING and GSEA results.

QCBT7 induces the accumulation of ubiquitylated proteins

To investigate whether QCBT7 inhibits proteasome activity as suggested from Bru-seq analysis, immunoblot was performed using the antibody against the ubiquityl group of ubiquitylated proteins in QCBT7-treated pancreatic cancer cells. Ubiquitylated proteins are normally subjected to proteasome-mediated degradation, but inhibition of the proteasome results in the accumulation of slower-migrating ubiquitylated proteins. QCBT7 treatment resulted in the dose-dependent accumulation of ubiquitylated proteins in both MIA PaCa-2 and PANC-1 cells

(Figure V-4). Similarly, both MG132 and ixazomib caused a significant accumulation of ubiquitylated proteins ($p < 0.005$). QCBT7 showed a stronger accumulating effect than MG132 in PANC-1, while ixazomib was the most potent inducer of ubiquitylated proteins in both cell lines. These results support the hypothesis that QCBT7 has proteasome inhibitory activity. Ixazomib, which reversibly and selectively binds to the proteasome beta 5 subunit (PSMB5) of the 20S catalytic subunit, has been approved as an orally bioavailable proteasome inhibitor for the treatment of multiple myeloma and is currently being tested in combination with other standard-of-care treatments in clinical trials for solid tumors^{33,34}.

We also tested 2-chlorobenzoic acid (2-CBA), a potential by-product of QCBT7 in the cellular reducing environment (Figure V-4). 2-CBA did not cause accumulation of ubiquitylated proteins, suggesting that QCBT7 or 8TQ is the active proteasome inhibitory molecules.

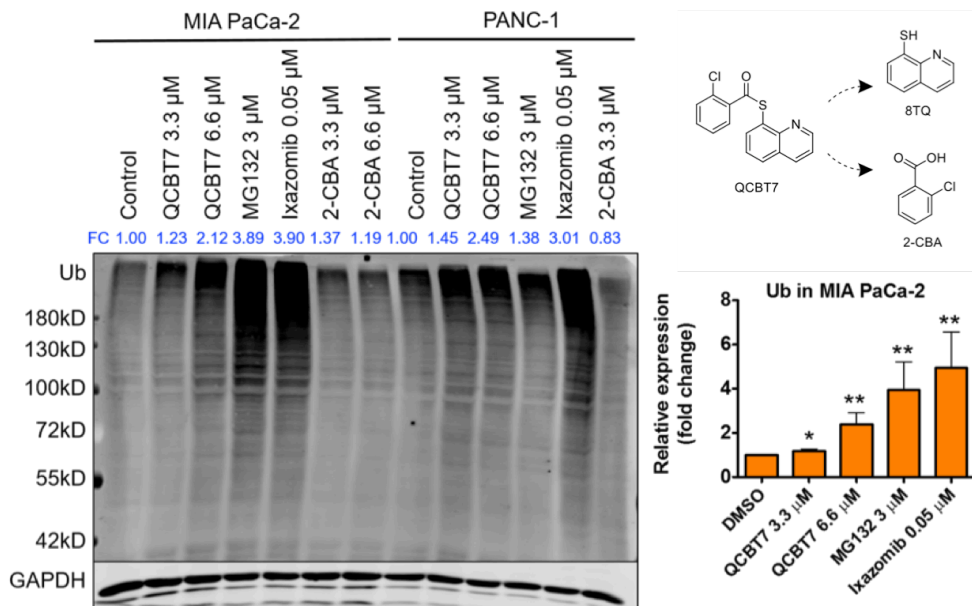


Figure V-4. QCBT7 causes the accumulation of ubiquitylated proteins in MIA PaCa-2 and PANC-1 cell lines, similar to MG132 and ixazomib. Cells were treated with QCBT7, MG132, ixazomib and 2-chlorobenzoic acid (2-CBA) for 24 h. MG132 and ixazomib were used as positive controls. FC: fold change, relative expression of the protein normalized to GAPDH expression. Data shown are representative of three independent experiments. Error bars represent standard deviation. * denotes $p < 0.05$, ** denotes $p < 0.005$ and *** denotes $p < 0.0005$ compared with DMSO control

QCBT7 increases the protein expression of genes related to glycolysis, ER stress and hypoxia in pancreatic cancer cells

To validate proteins and signaling pathways identified with the Bru-seq analysis, we performed immunoblot of selected genes related to glycolysis, ER stress and hypoxia in MIA PaCa-2 and PANC-1 cells. HK2 (hexokinase 2) and PFKFB4 (6-phosphofructo-2-kinase/fructose-2, 6-biphosphatase 4) are two glycolytic genes among the top 50 upregulated genes (Figure V-5A, Table V-3). QCBT7 elevated HK2 and PFKFB4 protein expression dose-dependently in both MIA PaCa-2 and PANC-1 cells (Figure V-5B), and it significantly increased their protein expression at 3.3 μ M (Figure V-5C, $p < 0.05$). HK2 and PFKFB4 are related to hexose metabolic processes and their protein expression increases under hypoxic conditions³⁵.

QCBT7 also induced CHOP expression, which is a protein biomarker for ER stress (Figure V-5B). Moreover, MG132 and ixazomib significantly increased PFKFB4 and CHOP expression, but not HK2, suggesting that they also have some differences in the downstream signaling due to potential distinct binding sites of the proteasome.

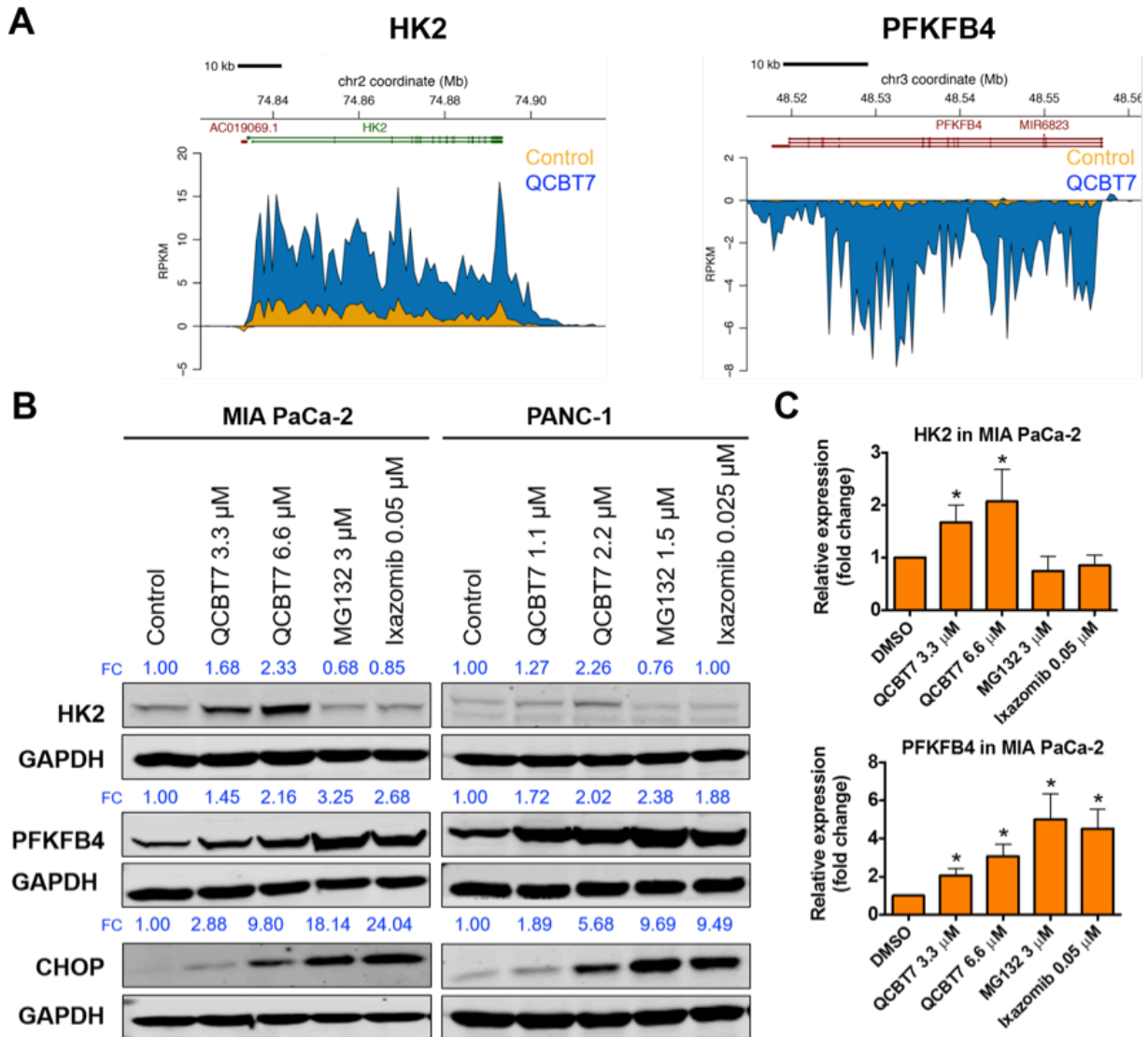


Figure V-5. QCBT7 increases nascent RNA and protein expression of genes related to glycolysis and ER stress in pancreatic cancer cells. (A) Trace diagrams of nascent RNA expression of HK2 and PFKFB4. Blue represents QCBT7 treatment and yellow represents the DMSO control. (B) Immunoblot of HK2, PFKFB4 and CHOP in MIA PaCa-2 and PANC-1 cells after 24 h treatment. FC: fold change, relative expression of the protein normalized to GAPDH expression. Data shown are representative of 3 independent experiments. (C) Quantification of relative expression of each protein in 3 independent experiments. Data are reported as mean \pm standard deviation. * denotes $p < 0.05$ compared with DMSO control.

Furthermore, QCBT7 increased the expression of hypoxia-related proteins, including HIF1A, SESN2, TRXR1, NQO1, HMOX1 and SLC7A11 (Figure V-6). At the nascent transcript level, NQO1, HMOX1 and SLC7A11 were dramatically upregulated by QCBT7 (Figure V-6A).

HMOX1 and SLC7A11 protein expression also increased significantly by 6.6 μ M QCBT7, and NQO1 showed dramatic increase in protein expression in PANC-1 but not MIA PaCa-2 cells (Figure V-6B, 6C). HIF1A, SESN2 and TRXR1 were upregulated by QCBT7 in both cell lines, and HIF1A and SESN2 showed a dose-dependent increase (Figure V-6B). MG132 and ixazomib had similar effects on HIF1A, SESN2, HMOX1 and SLC7A11 protein levels (Figure V-6B, 6C). SESN2 (sestrin 2) is inducible by hypoxia and oxidative stress conditions to balance metabolic homeostasis ³⁶. HMOX1 is a downstream target of HIF1A, and is sensitive to cellular redox signaling ³⁷. In addition, hypoxia affects glutathione metabolism ³⁵. TRXR1 (thioredoxin reductase 1) was elevated by QCBT7 to possibly balance the increase of HIF1A and maintain redox homeostasis. SLC7A11 (solute carrier family 7 member 11), which regulates glutamate transport, also showed an increased expression with the treatment ³⁸.

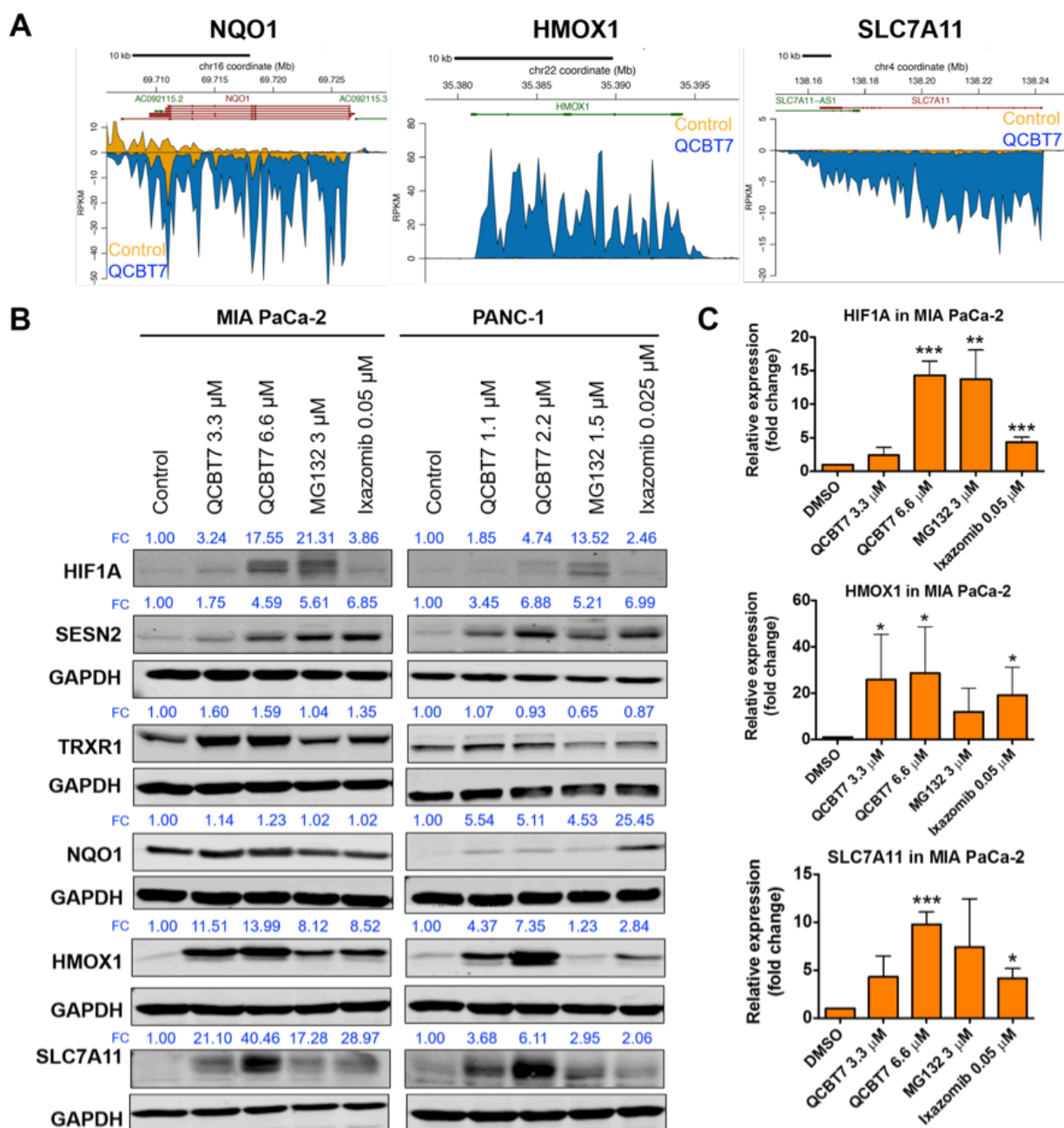


Figure V-6. QCBT7 increases nascent RNA and protein expression of genes related to hypoxia in pancreatic cancer cells. (A) Trace diagrams of nascent RNA expression of NQO1, HMOX1 and SLC7A11. Blue represents QCBT7 treatment and yellow represents the DMSO control. (B) Immunoblot of HIF1A, SESN2, TRXR1, NQO1, HMOX1 and SLC7A11 in MIA PaCa-2 and PANC-1 cells after 24 h treatment. FC: fold change, relative expression of the protein normalized to GAPDH expression. Data shown are representative of 3 independent experiments. (C) Quantification of relative expression of each protein in 3 independent experiments. Data are reported as mean \pm standard deviation. * denotes $p < 0.05$, ** denotes $p < 0.005$ and *** denotes $p < 0.0005$ compared with DMSO control.

Our immunoblot results of MG132 and ixazomib corroborate the previously reported mechanisms of proteasome inhibitors in inducing hypoxia and ER stress. MG132 increases the protein level of SESN2 due to the accumulation of ubiquitylated SESN2, and it is dependent on Nrf2³⁶. MG132, ixazomib and bortezomib increase HMOX1 and CHOP expression level due to Nrf2 signaling and ER stress^{27,31-34,39}. Compared with MG132 and ixazomib, QCBT7 also induces the expression of most proteins, such as PFKFB4, CHOP, HIF1A and HMOX1, supporting their similar mechanisms (Figure V-5, 6). The signaling pathways affected by QCBT7 have a strong correlation with its proteasome inhibition activity.

Overall, HK2, PFKFB4, CHOP, HIF1A, SESN2, TRXR1, NQO1, HMOX1 and SLC7A11 proteins are robustly upregulated in pancreatic cancer cells by QCBT7. Most proteins show a dose-dependent increase in response to QCBT7, MG132 and ixazomib. These results indicate that QCBT7 induces hypoxia, ER stress and glycolysis, and finally leads to cancer cell death, similar to MG132 and ixazomib

PFKFB4 is a potential biomarker to study proteasome inhibition

We identified that protein expression of PFKFB4 was significantly elevated by MG132, ixazomib and QCBT7. Additionally, QCBT7 increased PFKFB4 protein level back in the PFKFB4 knockdown MIA PaCa-2 cells (Figure V-S1). Our results show for the first time that PFKFB4 transcript and protein levels can be used to evaluate the response to proteasome inhibitors in pancreatic cancer. PFKFB4 is essential for cellular response to hypoxia, glucose metabolism and cell survival, and its depletion in p53-deficient prostate cancer cells inhibits tumor growth and cell survival^{35,40-42}. PFKFB4 is also recognized as an autophagy regulator,

relating to cancer cell death⁴³. Most importantly, it may be used as a new response regulatory protein to study the downstream signaling of MG132, ixazomib and other proteasome inhibitors.

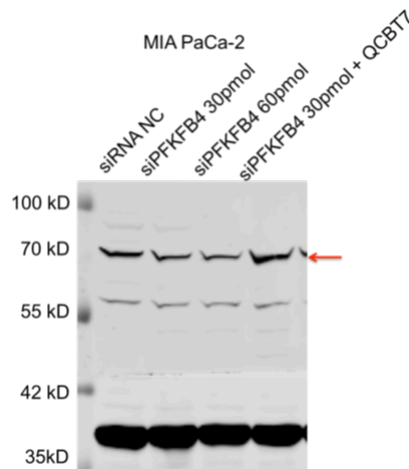


Figure V-S1. PFKFB4 protein level decreased by PFKFB4 siRNA at 30 pmol and 60 pmol, and QCBT7 increased the protein level back. The molecular weight of the target band is around 70 kD. NC: scramble siRNA.

Conclusions

In this study, the STRING, GSEA and CMAP analyses of the novel compound QCBT7 reveal that it induces transcriptional responses related to proteasome inhibition, hypoxia, ER stress and glycolysis. Moreover, QCBT7 blocked the degradation of ubiquitylated proteins, similar to MG132 and ixazomib. We demonstrated that PFKFB4, HK2, CHOP, HIF1A, SESN2, TRXR1, NQO1, HMOX1 and SLC7A11 protein levels increased upon QCBT7 treatment. MG132 and ixazomib also elevated PFKFB4, CHOP, HIF1A, SESN2, HMOX1 and SLC7A11 protein levels. Additionally, for the first time we identify PFKFB4 as a potential biomarker to monitor proteasome inhibition. In conclusion, QCBT7 shares similarity with proteasome inhibitors at both the transcript and protein levels, and blocks the protein degradation pathway. Importantly, our study reveals and confirms the association between hypoxia, glycolysis, ER stress and proteasome inhibition in pancreatic cancer cells.

Methods

Cell Culture. MIA PaCa-2, PANC-1, HCT 116 and KYSE-70 cells were cultured in RPMI 1640 medium (Gibco) supplemented with 10% FBS (Atlanta Biologicals). Cells were grown at 37 °C in a humidified atmosphere of 5% CO₂. All cell lines used were maintained in culture under 35 passages and tested regularly for mycoplasma contamination using Plasmotest Kit (InvivoGen, San Diego, CA).

MTT assay. Cytotoxicity of compounds was determined by a 3-(4,5-dimethylthiazol-2-yl)-2,5-diphenyltetrazolium bromide (MTT) assay as previously described⁴⁴. Briefly, cells were seeded in 96-well tissue culture plates and treated with compounds or vehicle for 72 h after overnight attachment. 20 µL MTT (3 mg/mL) was added, and the cells were incubated with MTT for 3 h. DMSO was added after removing the media and absorbance was measured at 570 nm.

Immunoblot. After overnight attachment in 6-well tissue culture plates, cells were treated with QCBT7 (3.3 µM or 6.6 µM), MG132 (3 µM), ixazomib (0.05 µM), or 2-CBA (3.3 µM or 6.6 µM). After 24 h treatment, cells were washed with 1×DPBS and lysed using RIPA lysis buffer in the presence of 1×protease inhibitor cocktail (Sigma-Aldrich) and 1×phosphatase inhibitor cocktail (VWR International). Cell lysates were vortexed and centrifuged at 12,000×g for 15 min at 4 °C. Protein concentration of the samples was measured using a BCA protein assay (Thermo Fisher Scientific) and equal amounts of total proteins were resolved on 10% or 8% polyacrylamide *via* SDS-PAGE. The separated proteins were transferred onto PVDF membranes (Thermo Fisher Scientific, 0.45 µm) and blocked in 5% milk for 1 h at room temperature. The membranes were probed with primary antibodies in 5% milk or 5% BSA at 4 °C overnight with recommended dilution (HK2: Cell Signaling Technology (CST) #2106, PFKFB4: Thermo Fisher

PA5-15475, CHOP: CST #2895, HIF1A: CST #3716, SESN2: CST #8487, TRXR1: CST #15140, NQO1: CST #3187, HMOX1: CST #5061, SLC7A11: CST #12691, Ub: CST #3936). Secondary antibodies were added at 1:6000 dilution (Thermo Fisher Scientific, DyLight 800, #SA5-35571 and # SA5-35521) and membranes were incubated for 1 h at room temperature. Finally, membranes were imaged using Odyssey Imaging Systems (LI-COR Biosciences).

PFKFB4 siRNA knock down study. siRNA targeting PFKFB4 was purchased from Thermo Fisher Scientific (#4427038). 8 million MIA PaCa-2 cells were seeded in 6-well tissue culture plates. After overnight attachment, 30 pmol and 60 pmol siPFKFB4 were added to MIA PaCa-2 cells following the manufacturer's protocol. QCBT7 (3.3 μ M) was added to the cells at the same time. Cells were collected after 24 h treatment for later immunoblot.

Bru-seq experiment and bioinformatics analysis. Bru-seq experiment for nascent RNA measurement was performed as previously reported ⁴⁴. Briefly, MIA PaCa-2 cells were treated with QCBT7 for 4 h. Bromouridine was added to the cells at a final concentration of 2 mM in the last 30 min of the treatment. Cells were then collected in Trizol and total RNA was isolated. The bromouridine-containing RNA population was further isolated and sequenced. Sequencing reads were mapped to the hg19 reference genome. Further analysis was conducted using DESeq, GSEA, STRING and CMAP. R (version 3.3.2) was used to calculate Pearson correlation and make related figures.

Statistics. Results were shown as mean \pm standard deviation as stated in the figure or table legends. Unpaired t-test was performed for data analysis.

Author contributions

Shuai Hu is the primary author. Yi Jin synthesized all the QCBT7 analogs. Yangnan Liu purified some analogs. Mats Ljungman lab conducted the Bru-seq experiments. Nouri Neamati is the corresponding author.

References

1. E.E. Manasanch, R.Z. Orlowski, Proteasome inhibitors in cancer therapy, *Nat Rev Clin Oncol*, 14 (2017) 417-433.
2. G.S. Kaplan, C.C. Torcun, T. Grune, N.K. Ozer, B. Karademir, Proteasome inhibitors in cancer therapy: Treatment regimen and peripheral neuropathy as a side effect, *Free Radic Biol Med*, 103 (2017) 1-13.
3. A.L. Goldberg, Development of proteasome inhibitors as research tools and cancer drugs, *J Cell Biol*, 199 (2012) 583-588.
4. D.E. Johnson, The ubiquitin-proteasome system: Opportunities for therapeutic intervention in solid tumors, *Endocr Relat Cancer*, 22 (2015) T1-17.
5. F. Cottini, A. Guidetti, C.P. Prada, T. Hideshima, M. Maglio, C. Varga, D. Chauhan, J. Laubach, K.C. Anderson, P.G. Richardson, Resistance to proteasome inhibitors in multiple myeloma, in: Q.P. Dou (Ed.) *Resistance to proteasome inhibitors in cancer: Molecular mechanisms and strategies to overcome resistance*, Springer International Publishing, Cham, 2014, pp. 47-80.
6. D. Li, K. Xie, R. Wolff, J.L. Abbruzzese, Pancreatic cancer, *Lancet*, 363 (2004) 1049-1057.
7. A. Semaan, A. Maitra, Pancreatic cancer in 2017: Rebooting pancreatic cancer knowledge and treatment options, *Nat Rev Gastroenterol Hepatol*, (2018).
8. J. Kleeff, M. Korc, M. Apte, C. La Vecchia, C.D. Johnson, A.V. Biankin, R.E. Neale, M. Tempero, D.A. Tuveson, R.H. Hruban, J.P. Neoptolemos, Pancreatic cancer, *Nat Rev Dis Primers*, 2 (2016) 16022.
9. F. Aroldi, P. Bertocchi, G. Savelli, E. Rosso, A. Zaniboni, Pancreatic cancer: New hopes after first line treatment, *World J Gastrointest Oncol*, 8 (2016) 682-687.
10. A. Lambert, C. Gavaille, T. Conroy, Current status on the place of folfirinix in metastatic pancreatic cancer and future directions, *Therap Adv Gastroenterol*, 10 (2017) 631-645.
11. A. Belalcazar, W.L. Shaib, M.R. Farren, C. Zhang, Z. Chen, L. Yang, G.B. Lesinski, B.F. El-Rayes, G.P. Nagaraju, Inhibiting heat shock protein 90 and the ubiquitin-proteasome pathway impairs metabolic homeostasis and leads to cell death in human pancreatic cancer cells, *Cancer*, 123 (2017) 4924-4933.

12. X. Li, F. Zhu, J. Jiang, C. Sun, Q. Zhong, M. Shen, X. Wang, R. Tian, C. Shi, M. Xu, F. Peng, X. Guo, J. Hu, D. Ye, M. Wang, R. Qin, Simultaneous inhibition of the ubiquitin-proteasome system and autophagy enhances apoptosis induced by ER stress aggravators in human pancreatic cancer cells, *Autophagy*, 12 (2016) 1521-1537.
13. S.T. Nawrocki, J.S. Carew, M.S. Pino, R.A. Highshaw, K. Dunner, Jr., P. Huang, J.L. Abbruzzese, D.J. McConkey, Bortezomib sensitizes pancreatic cancer cells to endoplasmic reticulum stress-mediated apoptosis, *Cancer Res*, 65 (2005) 11658-11666.
14. J. Guo, J. Hao, H. Jiang, J. Jin, H. Wu, Z. Jin, Z. Li, Proteasome activator subunit 3 promotes pancreatic cancer growth via c-myc-glycolysis signaling axis, *Cancer Lett*, 386 (2017) 161-167.
15. J. Li, T. Yakushi, F. Parlati, A.L. Mackinnon, C. Perez, Y. Ma, K.P. Carter, S. Colayco, G. Magnuson, B. Brown, K. Nguyen, S. Vasile, E. Suyama, L.H. Smith, E. Sergienko, A.B. Pinkerton, T.D.Y. Chung, A.E. Palmer, I. Pass, S. Hess, S.M. Cohen, R.J. Deshaies, Capzimin is a potent and specific inhibitor of proteasome isopeptidase rpn11, *Nat Chem Biol*, 13 (2017) 486-493.
16. A.P. Gorka, A. de Dios, P.D. Roepe, Quinoline drug-heme interactions and implications for antimalarial cytostatic versus cytotoxic activities, *J Med Chem*, 56 (2013) 5231-5246.
17. S. Jain, V. Chandra, P. Kumar Jain, K. Pathak, D. Pathak, A. Vaidya, Comprehensive review on current developments of quinoline-based anticancer agents, *Arab J Chem*, (2016). Epub Oct 26, 2016. DOI: 10.1016/j.arabjc.2016.10.009.
18. X.L. Liu, Y. Shi, J.S. Kang, P. Oelschlaeger, K.W. Yang, Amino acid thioester derivatives: A highly promising scaffold for the development of metallo-beta-lactamase II inhibitors, *ACS Med Chem Lett*, 6 (2015) 660-664.
19. H.-J. Zhou, D. Wustrow, Compositions and methods for JAMM protein inhibition, WO2014066506 (A2) (2014).
20. A. Kyani, S. Tamura, S. Yang, A. Shergalis, S. Samanta, Y. Kuang, M. Ljungman, N. Neamati, Discovery and mechanistic elucidation of a class of protein disulfide isomerase inhibitors for the treatment of glioblastoma, *ChemMedChem*, 13 (2018) 164-177.
21. L.J. Jensen, M. Kuhn, M. Stark, S. Chaffron, C. Creevey, J. Muller, T. Doerks, P. Julien, A. Roth, M. Simonovic, P. Bork, C. von Mering, STRING 8--a global view on proteins and their functional interactions in 630 organisms, *Nucleic Acids Res*, 37 (2009) D412-416.
22. A. Subramanian, P. Tamayo, V.K. Mootha, S. Mukherjee, B.L. Ebert, M.A. Gillette, A. Paulovich, S.L. Pomeroy, T.R. Golub, E.S. Lander, J.P. Mesirov, Gene set enrichment analysis: A knowledge-based approach for interpreting genome-wide expression profiles, *Proc Natl Acad Sci USA*, 102 (2005) 15545-15550.
23. V.K. Mootha, C.M. Lindgren, K.F. Eriksson, A. Subramanian, S. Sihag, J. Lehar, P. Puigserver, E. Carlsson, M. Ridderstrale, E. Laurila, N. Houstis, M.J. Daly, N. Patterson, J.P. Mesirov, T.R. Golub, P. Tamayo, B. Spiegelman, E.S. Lander, J.N. Hirschhorn, D. Altshuler, L.C. Groop, Pgc-1alpha-responsive genes involved in oxidative phosphorylation are coordinately downregulated in human diabetes, *Nat Genet*, 34 (2003) 267-273.

24. L.H. Meng, R. Mohan, B.H.B. Kwok, M. Elofsson, N. Sin, C.M. Crews, Epoxomicin, a potent and selective proteasome inhibitor, exhibits in vivo antiinflammatory activity, *Proc Natl Acad Sci USA*, 96 (1999) 10403-10408.
25. A. Subramanian, R. Narayan, S.M. Corsello, D.D. Peck, T.E. Natoli, X. Lu, J. Gould, J.F. Davis, A.A. Tubelli, J.K. Asiedu, D.L. Lahr, J.E. Hirschman, Z. Liu, M. Donahue, B. Julian, M. Khan, D. Wadden, I.C. Smith, D. Lam, A. Liberzon, C. Toder, M. Bagul, M. Orzechowski, O.M. Enache, F. Piccioni, S.A. Johnson, N.J. Lyons, A.H. Berger, A.F. Shamji, A.N. Brooks, A. Vrcic, C. Flynn, J. Rosains, D.Y. Takeda, R. Hu, D. Davison, J. Lamb, K. Ardlie, L. Hogstrom, P. Greenside, N.S. Gray, P.A. Clemons, S. Silver, X. Wu, W.N. Zhao, W. Read-Button, X. Wu, S.J. Haggarty, L.V. Ronco, J.S. Boehm, S.L. Schreiber, J.G. Doench, J.A. Bittker, D.E. Root, B. Wong, T.R. Golub, A next generation connectivity map: L1000 platform and the first 1,000,000 profiles, *Cell*, 171 (2017) 1437-1452 e1417.
26. N. Guo, Z. Peng, Mg132, a proteasome inhibitor, induces apoptosis in tumor cells, *Asia Pac J Clin Oncol*, 9 (2013) 6-11.
27. S. Nerini-Molteni, M. Ferrarini, S. Cozza, F. Caligaris-Cappio, R. Sitia, Redox homeostasis modulates the sensitivity of myeloma cells to bortezomib, *Br J Haematol*, 141 (2008) 494-503.
28. I. Riz, T.S. Hawley, J.W. Marsal, R.G. Hawley, Noncanonical sqstm1/p62-nrf2 pathway activation mediates proteasome inhibitor resistance in multiple myeloma cells via redox, metabolic and translational reprogramming, *Oncotarget*, 7 (2016) 66360-66385.
29. D.J. Barakat, J. Mendonca, T. Barberi, J. Zhang, S.K. Kachhap, I. Paz-Priel, A.D. Friedman, C/ebp β regulates sensitivity to bortezomib in prostate cancer cells by inducing redd1 and autophagosome-lysosome fusion, *Cancer Lett*, 375 (2016) 152-161.
30. L. Liu, S. Ito, N. Nishio, Y. Sun, N. Chen, Y. Tanaka, K. Isobe, Gadd34 facilitates cell death resulting from proteasome inhibition, *Anticancer Res*, 35 (2015) 5317-5324.
31. W. Cui, Y. Bai, P. Luo, L. Miao, L. Cai, Preventive and therapeutic effects of mg132 by activating nrf2-are signaling pathway on oxidative stress-induced cardiovascular and renal injury, *Oxid Med Cell Longev*, 2013 (2013) 306073.
32. H.S. Park, Y. Jun do, C.R. Han, H.J. Woo, Y.H. Kim, Proteasome inhibitor mg132-induced apoptosis via er stress-mediated apoptotic pathway and its potentiation by protein tyrosine kinase p56lck in human jurkat t cells, *Biochem Pharmacol*, 82 (2011) 1110-1125.
33. Q. Fan, B. Liu, Identification of the anticancer effects of a novel proteasome inhibitor, ixazomib, on colorectal cancer using a combined method of microarray and bioinformatics analysis, *Onco Targets Ther*, 10 (2017) 3591-3606.
34. G. Augello, M. Modica, A. Azzolina, R. Puleio, G. Cassata, M.R. Emma, C. Di Sano, A. Cusimano, G. Montalto, M. Cervello, Preclinical evaluation of antitumor activity of the proteasome inhibitor mln2238 (ixazomib) in hepatocellular carcinoma cells, *Cell Death Dis*, 9 (2018) 28.

35. A. Leiherer, K. Geiger, A. Muendlein, H. Drexel, Hypoxia induces a hif-1 alpha dependent signaling cascade to make a complex metabolic switch in sgbs-adipocytes, *Molecular and Cellular Endocrinology*, 383 (2014) 21-31.
36. M.G. Kim, J.H. Yang, K.M. Kim, C.H. Jang, J.Y. Jung, I.J. Cho, S.M. Shin, S.H. Ki, Regulation of toll-like receptor-mediated sestrin2 induction by ap-1, nrf2, and the ubiquitin-proteasome system in macrophages, *Toxicol Sci*, 144 (2015) 425-435.
37. X.J. Sheng, H.J. Tu, W.L. Chien, K.H. Kang, D.H. Lu, H.H. Liou, M.J. Lee, W.M. Fu, Antagonism of proteasome inhibitor-induced heme oxygenase-1 expression by pink1 mutation, *PLoS One*, 12 (2017) e0183076.
38. L. Martin, L.B. Gardner, Stress-induced inhibition of nonsense-mediated rna decay regulates intracellular cystine transport and intracellular glutathione through regulation of the cystine/glutamate exchanger slc7a11, *Oncogene*, 34 (2015) 4211-4218.
39. D.H. Shin, Y.S. Chun, D.S. Lee, L.E. Huang, J.W. Park, Bortezomib inhibits tumor adaptation to hypoxia by stimulating the fih-mediated repression of hypoxia-inducible factor-1, *Blood*, 111 (2008) 3131-3136.
40. P. Kumar, U. Gullberg, I. Olsson, R. Ajore, Myeloid translocation gene-16 co-repressor promotes degradation of hypoxia-inducible factor 1, *PLoS One*, 10 (2015) e0123725.
41. S. Ros, C.R. Santos, S. Moco, F. Baenke, G. Kelly, M. Howell, N. Zamboni, A. Schulze, Functional metabolic screen identifies 6-phosphofructo-2-kinase/fructose-2,6-biphosphatase 4 as an important regulator of prostate cancer cell survival, *Cancer Discov*, 2 (2012) 328-343.
42. S. Ros, J. Floter, I. Kaymak, C. Da Costa, A. Houddane, S. Dubuis, B. Griffiths, R. Mitter, S. Walz, S. Blake, A. Behrens, K.M. Brindle, N. Zamboni, M.H. Rider, A. Schulze, 6-phosphofructo-2-kinase/fructose-2,6-biphosphatase 4 is essential for p53-null cancer cells, *Oncogene*, 36 (2017) 3287-3299.
43. A.M. Strohecker, S. Joshi, R. Possemato, R.T. Abraham, D.M. Sabatini, E. White, Identification of 6-phosphofructo-2-kinase/fructose-2,6-bisphosphatase as a novel autophagy regulator by high content shrna screening, *Oncogene*, 34 (2015) 5662-5676.
44. Y. Kuang, M. Sechi, S. Nurra, M. Ljungman, N. Neamati, Design and synthesis of novel reactive oxygen species inducers for the treatment of pancreatic ductal adenocarcinoma, *J Med Chem*, 61 (2018) 1576-1594.

CHAPTER VI

Concluding Summary and Future Directions

In this dissertation, I report three novel scaffolds of small molecules that modulate cellular redox homeostasis and further characterize their MOAs in ferroptosis, mitochondrial functions, or proteasome inhibition, respectively. Specifically, in Chapter III, through lead optimization of a previously reported ROS inducer, we identified QD394 with higher hydrophilicity and a similar post-treatment transcriptomic profile to napabucasin. Both compounds inhibited the phosphorylation of STAT3, induced DNA damage, and altered redox signaling in pancreatic cancer cells. Combination with various cell death inhibitors revealed that QD394 stimulated an iron-, ROS-, and GPX4-mediated cell death. We also linked QD394 with the downregulation of LRPPRC and PNPT1, which are two mitochondrial proteins regulating RNA catabolic processes and negatively correlated to the overall survival of pancreatic cancer patients (Figure VI-1).

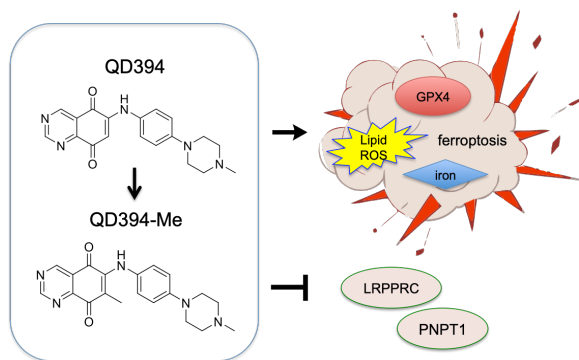


Figure VI-1. Mechanistic studies of QD394 and QD394-Me in pancreatic cancer cells.

In Chapter IV, we demonstrated that the previously described ROS inducer, Mito-Chlor, repressed transcription of the mitochondrial genome. Examining Bru-seq profiles identified a novel quinone compound SQD1 with similar transcriptomic profiles to Mito-Chlor. Both compounds induced oxidative stress, hypoxic response, and activation of AP-1 transcription factors. Cumulatively, this study identified novel mitochondrial transcription inhibitors that also regulate redox signaling (Figure VI-2).

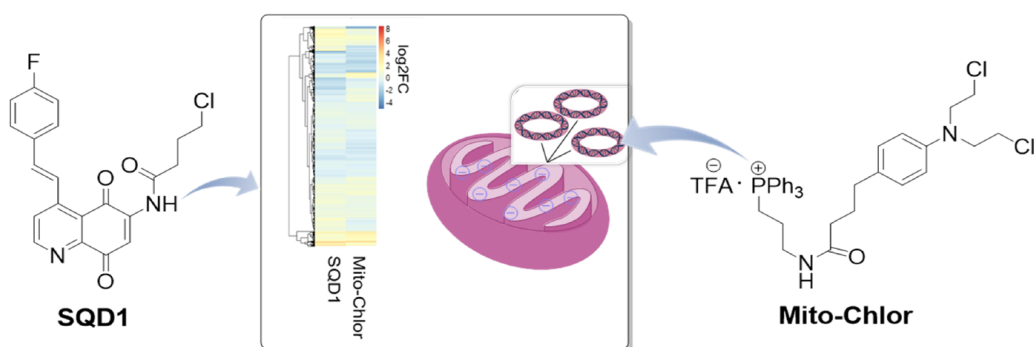


Figure VI-2. Characterization of mitochondrial transcription inhibitors.

In Chapter V, we identify a quinolin-chlorobenzothioate, QCBT7, as a new proteasome inhibitor showing cytotoxicity in a panel of cancer cell lines. QCBT7 caused an accumulation of ubiquitylated proteins in cancer cells and increased the expression of PFKFB4, CHOP, HMOX1, and SLC7A11 at both nascent RNA and protein levels. Overall, QCBT7 induces proteasome inhibition, hypoxic response, endoplasmic reticulum stress, and glycolysis. Furthermore, the involved signaling pathways emphasize the connection between redox signaling, hypoxia, and proteasome inhibition (Figure VI-3).

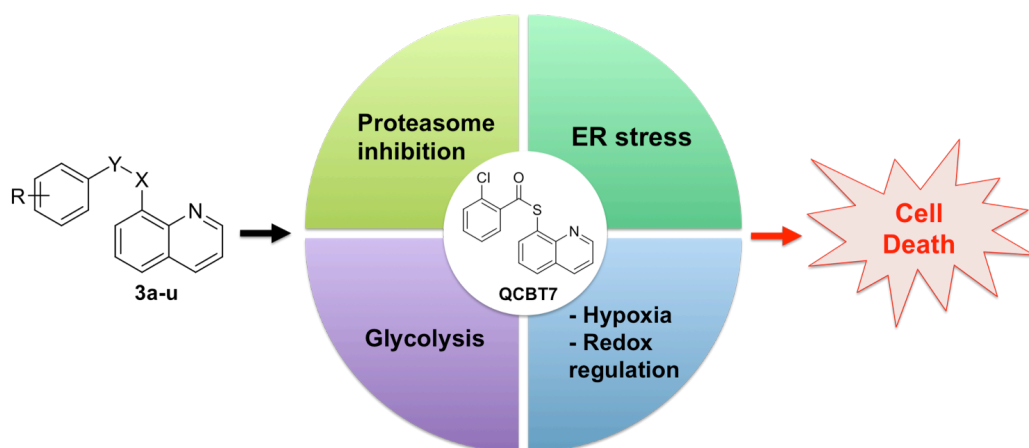


Figure VI-3. Characterization of QCBT7 analogs.

In addition to the investigations of small molecules regulating ROS signaling, we also reviewed ROS-related genes in cancer. Briefly, in Chapter II, we used Bru-seq, progression, and survival analysis to evaluate how ROS-related genes are involved in disease progression and survival in pancreatic cancer. This study provides novel potential target genes or biomarkers for pancreatic cancer and helps elucidate the mechanism of ROS-inducing agents for drug development. Moreover, a machine learning model was built to predict drug synergism as shown in appendix, which also confirms the synergy between QD394 and napabucasin.

Future directions

Relationship between mitochondrial RNA and redox modulators

We have observed that QD394 and QD394-Me decreased the protein expression of LRPPRC and PNPT1, and QD394 inhibited mitochondrial transcription in both heavy and light strands from Bru-seq analysis. These results suggest potential interactions between redox modulators and mitochondrial RNA for future investigation. Mitochondria are the major organelles as energy suppliers for cell growth and differentiation, and cancer cells reprogram the

metabolism of mitochondria to sustain aggressive proliferation and metastasis ¹. This work provides a foundation to target mitochondrial RNA catabolism and transcription to treat cancer cells, and future work could determine whether LRPPRC and/or PNPT1 are the regulators of this mitochondrial transcription inhibition. LRPPRC is an essential protein to maintain the mitochondrial ultrastructure and stability of mitochondrial mRNAs, the deficiency of which could cause impairment of the electron transport chain and mitochondrial permeability ^{2,3}. PNPT1 is involved in MT-ND6 transcript maturation and regulates mitochondrial RNA degradation and import ⁴⁻⁶. The further work may reveal the potential roles of LRPPRC and PNPT1 as drug targets to modulate mitochondria and cancer cell death.

Moreover, we observed that NQO1, an ROS-related enzyme we discussed in Chapter I, may be involved in the downregulation of LRPPRC and PNPT1 by QD394 and QD394-Me. This indicated that NQO1 could mediate the decrease of mitochondrial proteins and transcripts, which requires further evaluations. QD394 and QD394-Me also displayed synergy with dicoumarol (an NQO1 inhibitor), yet we did not fully understand the underlying mechanisms. NQO1 is a well-known enzyme that either detoxifies or bioactivates quinones, and small molecules targeting NQO1 have been developed to show preclinical and clinical efficacy in cancer ⁷. Future work may improve the understanding of NQO1-modulated pathways related to mitochondrial proteins and RNAs, and disclose new MOAs of NQO1-targeting agents.

In addition to determining RNA expression using Bru-seq, the effects on RNAs could also be evaluated *via* measuring RNA stability and degradation. There are established methods to determine RNA stability, including next-generation sequencing and biochemical and cell-

based assays ⁸. Moreover, RNA-targeted therapies are widely used to treat diseases, and a future study could evaluate the potential role of redox modulators in RNA-based anticancer therapies.

In vivo studies of redox modulators

We successfully improved the plasma stability and reduced the systemic toxicity of QD394 *via* structural optimization. However, the optimized analog QD394-Me still had a short half-life *in vivo*. It is possible that QD394-Me could bind to plasma protein or excrete rapidly in mice. Although QD394-Me had low plasma concentration, it still could be a promising anticancer candidate because three out of five mice showed a delay of tumor growth in the preliminary animal study. To further improve and confirm its *in vivo* efficacy, a new formulation or delivery system could be used to slow down compound metabolism in the plasma, such as using nanoparticles that could improve the PK profiles of compounds ^{9,10}. Additionally, both immunodeficient and immunocompetent mouse models of pancreatic cancer will be necessary to evaluate the efficacy of our redox modulators, since different cancers may have different response rates to the same treatment. ROS inducers could sensitize multidrug resistance cancer cells to certain chemotherapeutic drugs ¹¹, and we have observed synergistic effects between the redox modulators and FDA-approved drugs *in vitro*. Therefore, drug combination studies could also be tested to achieve better efficacy.

GPX4-targeted drug design

QD394-Me destabilized GPX4 in the CETSA experiments and its cytotoxicity was significantly dependent on GPX4, suggesting their potential interactions for further validation. GPX4 inhibition or depletion induces the accumulation of lipid peroxides and ferroptosis, and GPX4 inhibitors are more selective to cancer cells with a mesenchymal or drug-resistant

signature¹². The four major classes of ferroptosis inducers that we mentioned in Chapter II are all involved in regulating this central protein GPX4. Specifically, erastin indirectly suppresses GPX4 activity by decreasing GSH concentration; RSL3 directly reacts with the nucleophilic amino acid residues at the active site of GPX4 and reduces its activity; FIN56 promotes the degradation of GPX4; FINO2 indirectly inactivates GPX4 *via* unknown mechanisms¹³. It is possible that QD394-Me has similar mechanisms to one or several of these known ferroptosis inducers. It would be necessary to evaluate the effect of QD394-Me on GPX4 activity and binding in future studies to confirm the target. To measure GPX4 activity, an LC-MS-based or HP-TLC-based GPX4 activity assay could be used¹⁴. To prove the binding to GPX4, QD394-Me could be synthesized with an affinity tag to pull down the protein targets, and proteomics could be further performed to identify the binding partners¹⁴. This work may lead to a new class of GPX4-targeted small molecules to treat cancer, and the understanding of their binding mechanisms may assist design of novel GPX4 inhibitors as ferroptosis inducers.

Connections with RIP1-related pathways

RIP1-mediated pathways could be involved in MOAs of QD394 for further investigation. QD394 synergized with RIP1 kinase inhibitors (necrostatin-1 and nec-1s) and blocked the stabilization of RIP1 protein caused by necrostatin-1. However, the cytotoxicity of QD394 is not dependent on RIP1. We have not found the reasons for these effects, and it could be further explored to understand the relationships between ROS inducers and RIP1 signaling pathways. RIP1 works as a central switch between necroptosis and apoptosis, depending on the activity of caspase 8¹⁵. When caspase 8 is active, cells will be driven to caspase-dependent apoptosis; when caspase 8 is inactive, RIP1 will not be cleaved and mobilize RIP3 to phosphorylate MLKL,

inducing necroptosis. Future studies may be able to determine how RIP1-related pathways and caspase 8 activity are related to the cytotoxicity of QD394. This may also suggest other cell death pathways of QD394, besides the ferroptosis we characterized in the dissertation. This future study may provide insights into the interconnections among complex cell death pathways in cancer.

Altogether, this dissertation details the preclinical evaluation of novel small-molecule redox modulators in pancreatic cancer, and identifies novel ROS-related genes that are essential for cytotoxicity of redox modulators, PDAC progression, and patient survival. It improves the understanding of the relationship between redox signaling and cancer cell death, and provides the foundation of rational design of redox modulators. Future studies of redox modulators will seek to understand their deeper connections with mitochondrial transcription, GPX4 activity and binding, and RIP1-involved pathways. Systematic animal studies are needed to evaluate the *in vivo* efficacy of QD394-Me in pancreatic cancer. Additionally, novel ROS-related genes, such as *NQO1* and *ERO1*, could be further explored in terms of their functional roles in pancreatic cancer based on our bioinformatics analysis.

References

1. Wallace, D. C. Mitochondria and cancer. *Nat. Rev. Cancer* **12**, 685–698 (2012).
2. Cuillerier, A. *et al.* Loss of hepatic LRPPRC alters mitochondrial bioenergetics, regulation of permeability transition and trans-membrane ROS diffusion. *Human Molecular Genetics* vol. 26 3186–3201 (2017).
3. Zhou, W. *et al.* Proteasome-Independent Protein Knockdown by Small-Molecule Inhibitor for the Undruggable Lung Adenocarcinoma. *Journal of the American Chemical Society* vol. 141 18492–18499 (2019).
4. Liu, X. *et al.* PNPT1 Release from Mitochondria during Apoptosis Triggers Decay of Poly(A) RNAs. *Cell* vol. 174 187–201.e12 (2018).

5. Matilainen, S. *et al.* Defective mitochondrial RNA processing due to PNPT1 variants causes Leigh syndrome. *Human Molecular Genetics* vol. 26 3352–3361 (2017).
6. Wang, G. *et al.* PNPASE Regulates RNA Import into Mitochondria. *Cell* vol. 142 456–467 (2010).
7. Zhang, K. *et al.* NAD(P)H:Quinone Oxidoreductase 1 (NQO1) as a Therapeutic and Diagnostic Target in Cancer. *J. Med. Chem.* **61**, 6983–7003 (2018).
8. Cheneval, D., Kastelic, T., Fuerst, P. & Parker, C. N. A review of methods to monitor the modulation of mRNA stability: a novel approach to drug discovery and therapeutic intervention. *J. Biomol. Screen.* **15**, 609–622 (2010).
9. Shi, J., Votruba, A. R., Farokhzad, O. C. & Langer, R. Nanotechnology in drug delivery and tissue engineering: from discovery to applications. *Nano Lett.* **10**, 3223–3230 (2010).
10. Sanna, V. *et al.* Targeted Biocompatible Nanoparticles for the Delivery of (–)-Epigallocatechin 3-Gallate to Prostate Cancer Cells. *Journal of Medicinal Chemistry* vol. 54 1321–1332 (2011).
11. Cui, Q. *et al.* Modulating ROS to overcome multidrug resistance in cancer. *Drug Resist. Updat.* **41**, 1–25 (2018).
12. Liu, H., Schreiber, S. L. & Stockwell, B. R. Targeting Dependency on the GPX4 Lipid Peroxide Repair Pathway for Cancer Therapy. *Biochemistry* **57**, 2059–2060 (2018).
13. Lei, P., Bai, T. & Sun, Y. Mechanisms of Ferroptosis and Relations With Regulated Cell Death: A Review. *Front. Physiol.* **10**, 139 (2019).
14. Yang, W. S. *et al.* Regulation of ferroptotic cancer cell death by GPX4. *Cell* **156**, 317–331 (2014).
15. Legrand, A. J., Konstantinou, M., Goode, E. F. & Meier, P. The Diversification of Cell Death and Immunity: Memento Mori. *Mol. Cell* **76**, 232–242 (2019).

APPENDIX

Drug Synergism Prediction Using Machine Learning

Single-agent therapies have reached their bottleneck due to drug resistance and genetic heterogeneity in complex diseases. Combination therapies become better options than monotherapies for many diseases, including cancer and HIV, since they can increase the efficacy and reduce the toxicity and side effects in patients¹⁻³. However, random combinations of drugs may cause adverse effects or lessen the efficacy. With the emergence of a large number of drugs and drug candidates, it is costly, time-consuming and labor-intensive to test every pair through *in vitro* drug screening experiments. Alternatively, computational tools such as machine learning techniques can predict the synergistic effects of drug pairs more efficiently and prioritize the combinations for experimental and clinical tests³. Therefore, it is essential to develop a fast and convenient model to accurately predict drug combination effects to approach the experimental results.

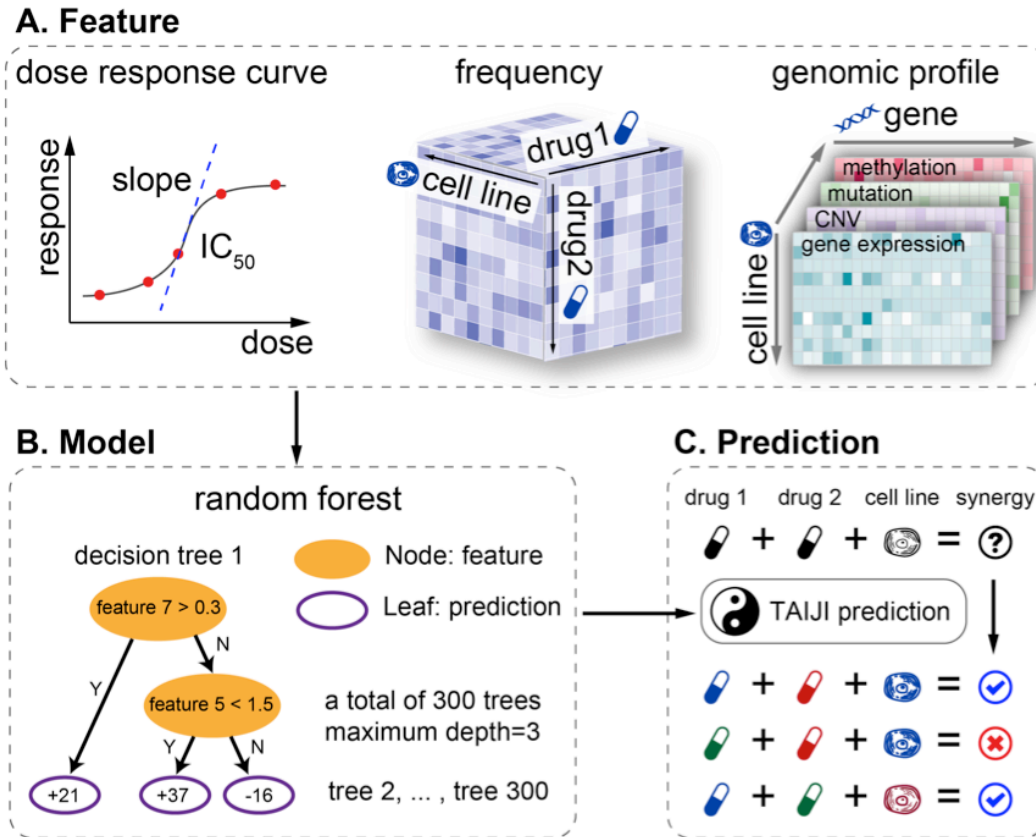
Many efforts have been made to predict drug synergy in cancer, utilizing Random Forests, Naive Bayes and deep learning algorithms. These pioneering studies have provided great advancement to estimate drug synergy⁴⁻⁶. To further facilitate the research of drug synergy, the Dialogue on Reverse Engineering Assessment and Method (DREAM)⁷ organized the AstraZeneca-Sanger Drug Combination Prediction Challenge⁸ to systematically evaluate the performance of different methods using a large dataset consisting of 11,500 experimentally

Notes: This work has been published as Li, H., **Hu, S.**, Neamati, N. & Guan, Y. *Bioinformatics* 35, 2338–2339 (2019).

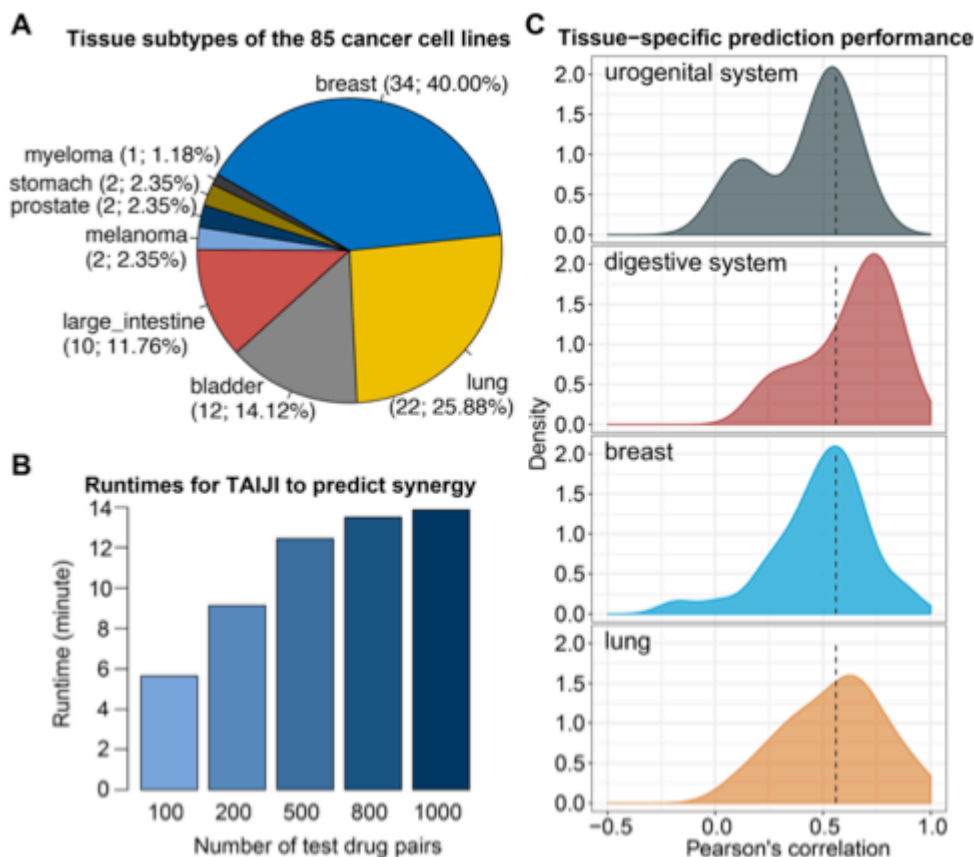
tested synergy scores of 118 drugs in 85 cancer cell lines. Our prediction algorithm ranked first in this challenge, leveraging the information from pharmacological data, molecular data and the gene-gene interaction network. Here, we present the software, TAIJI, to predict drug synergy based on our winning algorithm.

Methods and results

TAIJI is a novel program that utilizes both the pharmacological monotherapy results and cell line-specific molecular profiles (Appendix-1). Specifically, multiple features are extracted from the dose-response curves and the metrics of treatment effects. In addition, the post-treatment molecular features are simulated based on the pre-treatment genomic profiles and the gene-gene interaction network ⁹ *via* a network propagation approach. The nonlinear interactions between chemical features are learned by the random forest regressor ¹⁰⁻¹². Meanwhile, TAIJI is developed in the context of the largest dataset in the AstraZeneca-Sanger DREAM drug combination challenge, covering drug combination experiments in a broad spectrum of 85 cancer cell lines across different cancer tissues (Appendix-2A). To accelerate the computation, monotherapy- and molecular-based models in TAIJI are pre-trained, and the prediction of a drug pair can be finished within one second on average (Appendix -2B). Of note, TAIJI is a robust model by integrating the cross-drug and cross-cell line information. The average Pearson's correlation between predictions and observations is 0.53 (Appendix-2C), approaching the experimental replicates-level accuracy, the correlation of which is 0.56 ¹³. TAIJI is implemented using Perl and Python, two commonly used programming languages. It only requires scikit-learn, a popular machine learning package in Python.



Appendix-1. The workflow of TAIJI framework. (A) TAIJI captures multiple informative features from 1) the dose-response curve 2) the frequency of observed drugs and cell lines 3) cell line-specific genomic profiles. (B) A random forest regressor is used as the base learner, with a total of 300 trees and a maximum tree depth of 3. (C) TAIJI predicts the synergy of drug 1 - drug 2 - cell line combinations.



Appendix-2. Runtimes and prediction performance of TAIJI. (A) TAIJI is trained on a large drug synergy dataset covering 8 tissue subtypes containing 85 cancer cell lines (B) The runtimes for TAIJI using different numbers of cell line - drug 1 - drug 2 combinations. A total of 100, 200, 500, 800 and 1000 combinations were randomly selected for testing. Notably, the main time-consuming step is calculating the post-treatment molecular profile of a drug pair so that the runtime is not linear with the number of combinations. When a drug pair is tested across multiple cell lines, the runtime per combination becomes small. (C) The distribution of tissue-specific prediction correlations. The dashed line corresponds to the average upper limit of correlations calculated from technical replicates.

Conclusions

In this study, we present TAIJI, a novel fast software to predict drug synergy using the state-of-the-art machine learning algorithm. This software can be downloaded and easily used by computational biologists and pharmacologists to estimate the drug combinatorial effects and guide experimental and clinical trial design. This software predicts a synergistic effect between QD394 and napabucasin with a positive score, which is consistent with our experimental results in Chapter III.

Author contributions

Hongyang Li and Shuai Hu are equally contributed primary authors. Yuanfang Guan was the sole developer of the winning algorithm for the DREAM challenge. Yuanfang Guan is the corresponding author.

References

1. Al-Lazikani, B., Banerji, U. & Workman, P. Combinatorial drug therapy for cancer in the post-genomic era. *Nat. Biotechnol.* 30, 679–692 (2012).
2. Clercq, E. D. & De Clercq, E. The design of drugs for HIV and HCV. *Nat. Rev. Drug Discov.* 6, 1001–1018 (2007).
3. Weinstein, Z. B., Bender, A. & Cokol, M. Prediction of synergistic drug combinations. *Current Opinion in Systems Biology* 4, 24–28 (2017).
4. Li, P. *et al.* Large-scale exploration and analysis of drug combinations. *Bioinformatics* 31, 2007–2016 (2015).
5. Wildenhain, J. *et al.* Prediction of Synergism from Chemical-Genetic Interactions by Machine Learning. *Cell Syst* 1, 383–395 (2015).
6. Preuer, K. *et al.* DeepSynergy: predicting anti-cancer drug synergy with Deep Learning. *Bioinformatics* 34, 1538–1546 (2018).
7. Stolovitzky, G., Monroe, D. & Califano, A. Dialogue on reverse-engineering assessment and methods: the DREAM of high-throughput pathway inference. *Ann. N. Y. Acad. Sci.* 1115, 1–22 (2007).
8. Bionetworks, S. Synapse | Sage Bionetworks. <https://www.synapse.org/#!/Synapse:syn4231880>.
9. Guan, Y. *et al.* A Genomewide Functional Network for the Laboratory Mouse. *PLoS Comput. Biol.* 4, e1000165 (2008).
10. Breiman, L. 10.1023/A:1010933404324. *Machine Learning* vol. 45 5–32 (2001).
11. Li, H., Panwar, B., Omenn, G. S. & Guan, Y. Accurate prediction of personalized olfactory perception from large-scale chemoinformatic features. *Gigascience* 7, (2018).
12. Li, H., Li, T., Quang, D. & Guan, Y. Network Propagation Predicts Drug Synergy in Cancers. *Cancer Res.* 78, 5446–5457 (2018).

13. Menden, M. P. *et al.* A cancer pharmacogenomic screen powering crowd-sourced advancement of drug combination prediction. (2017) doi:10.1101/200451.